OPTIMIZING THIN-FILM PROPERTIES VIA ATOMIC-SCALE MODIFICATION

Alessandro Troglia

Ph.D. thesis, Universiteit van Amsterdam, 2024
Optimizing thin-film properties via atomic-scale modification
Alessandro Troglia
ISBN 978-94-6496-154-6

Printed by: Gildeprint – www.gildeprint.nl
Cover design: A. Troglia and F. Elam

An electronic copy of this thesis is available at:
https://dare.uva.nl & https://ir.arcnl.nl

The research described in this thesis was performed at the Advanced Research Center for Nanolithography (ARCNL), a public-private partnership between the University of Amsterdam (UvA), the Vrije Universiteit Amsterdam (VU), the Rijksuniversiteit Groningen (RUG), the Netherlands Organization for Scientifc Research (NWO), and the semiconductor-equipment manufacturer ASML.

OPTIMIZING THIN-FILM PROPERTIES VIA ATOMIC-SCALE MODIFICATION

Academisch Proefschrift

ter verkrijging van de graad van doctor
aan de Universiteit van Amsterdam
op gezag van de Rector Magnificus
prof. dr. ir. P. P. C. C. Verbeek
ten overstaan van een door het College voor Promoties ingestelde commissie,
in het openbaar te verdedigen in de Agnietenkapel
op vrijdag 13 september 2024, te 10:00 uur

door

Alessandro Troglia

geboren te Genova

Promotiecommissie

Promotor

prof. dr. M. S. Golden	Universiteit van Amsterdam

Copromotor

dr. R. Bliem	Universiteit van Amsterdam

Overige leden

prof. dr. P. C. M. Planken	Universiteit van Amsterdam
dr. A. Isaeva	Universiteit van Amsterdam
dr. E. van Heumen	Universiteit van Amsterdam
prof. dr. ir. G. Koster	University of Twente
dr. R. van Lent	ASML

Faculteit der Natuurwetenschappen, Wiskunde en Informatica

CONTENTS

Introduction **1**
Motivation . . . 1
Outline . . . 3
References . . . 5

1 A brief review on thin-film deposition, growth kinetics, and stress development in coatings **9**
1.1 Thin-film deposition techniques . . . 9
1.1.1 Sputter deposition . . . 9
1.1.2 Pulsed laser deposition . . . 12
1.1.3 PLD of metals and alloys . . . 15
1.2 Growth kinetics . . . 18
1.3 Stress . . . 23
References . . . 29

2 Free-standing nanolayers based on Ru silicide formation on Si(100) **39**
2.1 Introduction . . . 40
2.2 Methods . . . 41
2.2.1 Sample preparation . . . 41
2.2.2 X-ray photoelectron spectroscopy . . . 41
2.2.3 Scanning electron microscopy . . . 42
2.2.4 Transmission electron microscopy . . . 42
2.3 Results and Discussion . . . 42
2.4 Conclusions . . . 50
References . . . 51
Appendix . . . 57

3 Tuning material properties via disorder: From crystalline alloy to metallic glass **61**
3.1 Introduction . . . 62
3.2 Results and Discussion . . . 63
3.3 Conclusions . . . 71
3.4 Methods . . . 71
3.4.1 Sample preparation . . . 71
3.4.2 X-ray diffraction . . . 72
3.4.3 Atomic force microscopy . . . 72
3.4.4 X-ray photoelectron spectroscopy . . . 72
3.4.5 Optical spectroscopy . . . 72
3.4.6 Transport measurements . . . 73

References . . . 75
Appendix . . . 81

4 Bridging the gap between high-entropy alloys and metallic glasses: Control over disorder and mechanical properties of coatings 89
4.1 Introduction . . . 90
4.1.1 High-entropy alloys: A brief overview . . . 90
4.1.2 High-entropy alloy thin films . . . 92
4.2 Methods . . . 93
4.2.1 Sample preparation . . . 93
4.2.2 X-ray diffraction . . . 94
4.2.3 Transmission electron microscopy . . . 94
4.2.4 X-ray photoelectron spectroscopy . . . 94
4.2.5 Hardness measurements . . . 94
4.3 Results . . . 95
4.4 Discussion . . . 101
4.5 Conclusions . . . 104
References . . . 105
Appendix . . . 113

Summary 117

Samenvatting 119

List of Publications 123

Acknowledgements 125

INTRODUCTION

MOTIVATION

In 1959, during an annual meeting of the American Physical Society, American Nobel laureate Richard Feynman gave a lecture entitled *'There is plenty of room at the bottom'* [1]. During his talk, Feynman described a *'new field of physics'*, based on the manipulation and control of atoms at the nanoscale, and stated that *'atoms on a small scale behave like nothing on a large scale, [...] so as we go down to the atomic level, we are working with different laws, and we can expect to do different things'*. In this famous and celebrated lecture, Feynman was the first to describe a scientific discipline that later would be known as nanotechnology [2]. Towards the end of the 20^{th} century, intensive research in the field of nanotechnology led to breakthroughs in several industries, such as electronics and computing, medicine and healthcare, renewable energy, aerospace, and transportation [3]. To the present day, nanotechnology has been one of the main enabling forces behind the technological advancements of the 21^{st} century [4]; also, it plays a fundamental role in everyday high-tech devices, such as laptops, smartphones and batteries.

Within nanotechnology, thin films – layers of materials with a thickness ranging from tens of microns down to a few nanometers – occupy a central position [5]. In general, thin films are employed to enhance or modify the properties of bulk materials [6]. The deposition of a layer with specific physical and chemical properties leads to improved functionality, designed to precise requirements. The versatile platform offered by thin-film technology to enhance, functionalize and tailor the performance of bulk materials has led to major improvements in a wide variety of applications. For instance, thin films enhance the hardness [7], wear- and corrosion-resistance of the surface [8, 9] without altering the bulk characteristics. In addition, the precise surface-engineering offered by thin films leads to improved conductivity [10], optical transmission [11], magnetic properties [12], and mechanical behavior [13], thus expanding the applicability and performance of bulk materials in numerous fields.

One of the most fascinating aspects of thin-film technology is the optimization of macroscopic properties through modifications at the nanoscale. The development of coatings with characteristics tailored to the application, often referred to as functional thin films [14], requires precise control over the physics and chemistry at the atomic level. Parameters such as the detailed arrangement of the atoms and molecules, the presence of defects, dopants and contaminants, the thickness of the film, and the interaction with the environment define the film properties, and their contribution determines the performance in the desired application. In this framework, thin films of metals and alloys are a good example of

functional coatings, which form an active area of fundamental research and are widely employed in industrial applications. Metallic thin films are employed in the semiconductor industry as interconnects, contacts, adhesion layers, and diffusion barriers within various devices, such as integrated circuits and memories, transistors, and light-emitting diodes [15, 16]. In the renewable energy sector, metallic thin films enhance light absorption and carrier extraction in photovoltaic and thermoelectric devices, in their function as substrates, reflective back contacts, and electrodes [17, 18]. Moreover, considerable attention has been recently devoted to thin films of alloys with multiple principal elements, which have shown remarkable features such as high thermal and chemical stability at elevated temperatures, superior hardness, wear- and oxidation resistance [19–22]. These functional properties are directly linked to the nanoscale structure of the materials, and should therefore be accessible for modification.

An example where tailored properties at the nanoscale have major impact on the macroscopic performance can be found in the context of the fabrication of microprocessors and memory modules. In particular, functional thin films are currently employed in sensitive components of state-of-the-art photolithographic machines for the production of the more sophisticated electronic devices [23]. In the advancement to extreme ultraviolet light (EUV, λ = 13.5 nm) [23], transmission lenses are no longer an option, and coating technology became even more essential. One of the more prominent cases are EUV optics, which reflect EUV light via constructive interference produced by an array of alternating thin films with a thickness of just a few nanometers [24, 25]. Moreover, the high level of atomic-scale control over interface processes prevents detrimental intermixing that would cause loss in EUV transmission. Additionally, to withstand the challenging environment of EUV lithography, the EUV protective coatings are functionalized for high oxidation resistance and emissivity, thermal and chemical stability, and low EUV absorption [26, 27].

The space industry is another example where functional coatings are employed to enhance properties at the macroscopic level. Materials used in spacecraft applications experience a wide variety of detrimental and challenging conditions, such as exposure to electromagnetic radiation and ionizing particles, strong temperature variations, hot-cold thermal cycles, presence of contaminants, space debris, and reactive radicals, such as atomic oxygen [28]. In this framework, functional metallic coatings enable spacecraft devices to withstand the challenging space environment, not only as protective layers [28, 29], but also as essential detectors' components [30, 31]. For instance, in the case of the recently-launched James Webb Space Telescope (JWST) [30], both the primary and secondary mirrors of JWST are coated with a 100 nm thick gold film. The function of the gold layer is twofold: protecting the mirror from oxidation and other chemical degradation processes in space, and enhancing the reflectivity in the near and mid-infrared spectral ranges [28]. In order to perform its functions, the gold film needs to possess well-defined properties at the nanoscale, like thickness-uniformity, low surface roughness, low thermal and mechanical stress, and high durability at cryogenic temperatures [31].

Furthermore, improving macroscopic materials properties by tailored modifications at the atomic level is considered a promising approach in the context of the latest-generation nuclear fusion reactors, which hold promise to bring us closer to a new source of clean energy production. In particular, the walls of the reactor heat exhaust system need to withstand extreme temperatures, particles, ions, and plasma fluxes [32], with materials expecting to undergo irreversible changes in structure and morphology. The latter include damage mechanisms such as hydrogen-induced blistering [33], sputter erosion [34], and undesired formation of nanostructures [35]. These degradation processes lead to critical lifetime issues for fundamental components, which therefore require materials with specific properties [35]. Thin-film technology allows the necessary flexibility to functionalize and enhance the physical and chemical characteristics of selected reactor walls materials, such as tungsten (W) and tungsten-based alloys [36, 37]. In fact, various studies have demonstrated that precise control over the microstructure, morphology, and inclusions of inert and noble gases (N, Ne, and Ar) can dramatically improve the performance of tungsten-based alloys as diffusion and retention barriers, and increase their resistance against wear and erosion under fusion conditions [36, 38].

Controlling and modifying the atomic scale has been a successful pathway to influence the macroscopic behavior of materials. In particular, functional coatings need to possess specific physical and chemical properties at the nanoscale, tailored to the intended application and its environment. In this context, a basic comprehension of atomic-level properties is necessary to allow for deterministic materials engineering, so that the control over the nanoscale meets performance in everyday life.

OUTLINE

In this thesis, the focus is on functionalizing the macroscopic properties of metallic thin films via tailored modifications at the nanoscale. In particular, these modifications are shown to have a dramatic impact on the coatings' physical and chemical properties at the macroscale. For instance, they play a major role in a wide variety of applications such as free-standing membranes, corrosion-resistant, hard, and optically transparent coatings. In chapter 1, the main thin-film deposition techniques employed in this thesis are reviewed, with emphasis on their major advantages/drawbacks and the implications for the deposition of metals and alloys. Moreover, the most important kinetic mechanisms governing film formation are discussed. In fact, effectively modifying the growth kinetics yields customized film properties at the nanoscale, such as tunable level of atomic order/disorder, and dramatic changes in the coatings' macroscopic behavior. Furthermore, the effects of stress buildup and relaxation in thin films are addressed. On the one hand, such mechanisms can generally lead to catastrophic failures in the material; on the other, they can be exploited and engineered as an innovative pathway towards the production of functional components. In chapter 2, a delamination process of metallic thin films upon annealing is explained within a nanoscale framework. A

stress-based mechanism induced by intermixing and diffusion is proposed, and an innovative strategy to produce macroscopic free-standing nanolayers is suggested. In chapter 3, a novel design approach to functionalize metallic thin films is explored, namely tuning atomic structural disorder by off-equilibrium growth. The approach is applied to a simple binary alloy model system, and the influence on optical, electronic, and corrosion-resistance properties is investigated. The concept is further expanded in chapter 4 to include thin films of a multi-component alloy. The applicability of atomic disorder as parameter to tailor thin-film properties to specific applications is investigated for high-entropy alloys, a class of materials that goes beyond the traditional concepts of alloying.

REFERENCES

[1] R. P. Feynman. “There’s plenty of room at the bottom: An invitation to open up a new field of physics”. In: *Caltech Engineering and Science* 23.5 (1960), pp. 22–36. URL: https://resolver.caltech.edu/CaltechES:23.5.0.

[2] S. Bayda, M. Adeel, T. Tuccinardi, M. Cordani, and F. Rizzolio. “The History of Nanoscience and Nanotechnology: From Chemical–Physical Applications to Nanomedicine”. In: *Molecules* 25.1 (2020), p. 112. ISSN: 1420-3049. DOI: 10.3390/molecules25010112.

[3] S. Malik, K. Muhammad, and Y. Waheed. “Nanotechnology: A Revolution in Modern Industry”. In: *Molecules* 28.2 (2023), p. 661. ISSN: 1420-3049. DOI: 10.3390/molecules28020661.

[4] R. Wennersten, J. Fidler, and A. Spitsyna. “Nanotechnology: A New Technological Revolution in the 21st Century”. In: *Handbook of Performability Engineering*. Springer London, 2008, pp. 943–952. ISBN: 978-1-84800-131-2. DOI: 10.1007/978-1-84800-131-2_57.

[5] A. Makhlouf. “Conventional and advanced coatings for industrial applications: an overview”. In: *Nanocoatings and Ultra-Thin Films*. Woodhead Publishing, 2011, pp. 159–181. ISBN: 978-1-84569-812-6. DOI: 10.1533/9780857094902.2.159.

[6] A. E. Ares. *Thin Films*. IntechOpen, 2021. ISBN: 978-1-83881-993-4. DOI: 10.5772/intechopen.87838.

[7] N. Wang, Q. Cao, X. Wang, S. Ding, D. Zhang, and J.-Z. Jiang. “Ultrahigh specific hardness of Co-Ni-V-Al medium entropy alloy thin films”. In: *Materials Today Communications* 31 (2022), p. 103447. ISSN: 2352-4928. DOI: 10.1016/j.mtcomm.2022.103447.

[8] E. Cihan, H. Störmer, H. Leiste, M. Stüber, and M. Dienwiebel. “Low friction of metallic multilayers by formation of a shear-induced alloy”. In: *Scientific Reports* 9 (2019), p. 9480. ISSN: 2045-2322. DOI: 10.1038/s41598-019-45734-7.

[9] S. V. Ketov, X. Shi, G. Xie, R. Kumashiro, A. Y. Churyumov, A. I. Bazlov, N. Chen, Y. Ishikawa, N. Asao, H. Wu, and D. V. Louzguine-Luzgin. “Nanostructured Zr-Pd Metallic Glass Thin Film for Biochemical Applications”. In: *Scientific Reports* 5 (2015), p. 7799. ISSN: 2045-2322. DOI: 10.1038/srep07799.

[10] Y.-W. Zhang, B.-Y. Wu, K.-C. Chen, C.-H. Wu, and S.-Y. Lin. “Highly conductive nanometer-thick gold films grown on molybdenum disulfide surfaces for interconnect applications”. In: *Scientific Reports* 10 (2020), p. 14463. ISSN: 2045-2322. DOI: 10.1038/s41598-020-71520-x.

[11] A. Axelevitch, B. Gorenstein, and G. Golan. “Investigation of Optical Transmission in Thin Metal Films”. In: *Physics Procedia* 32 (2012), pp. 1–13. ISSN: 1875-3892. DOI: 10.1016/j.phpro.2012.03.510.

[12] T. Thomson. “Magnetic properties of metallic thin films”. In: *Metallic Films for Electronic, Optical and Magnetic Applications*. Woodhead Publishing, 2014, pp. 454–546. ISBN: 978-0-85709-057-7. DOI: 10.1533/9780857096296.2.454.

[13] W. Nix. “Metallic thin films: stresses and mechanical properties”. In: *Metallic Films for Electronic, Optical and Magnetic Applications*. Woodhead Publishing, 2014, pp. 353–421. ISBN: 978-0-85709-057-7. DOI: 10.1533/9780857096296.2.353.

[14] S. Zhang, J.-M. Ting, and W.-Y. Wu, eds. *Functional Thin Films Technology*. CRC Press, 2021. ISBN: 978-1-00308-808-0. DOI: 10.1201/9781003088080.

[15] S. D. Brotherton. *Introduction to Thin Film Transistors*. Springer Cham, 2013. ISBN: 978-3-319-00002-2. DOI: 10.1007/978-3-319-00002-2.

[16] F. O. Sequeda. “Thin Film Deposition Techniques in Microelectronics”. In: *JOM* 38 (1986), pp. 55–65. ISSN: 1543-1851. DOI: 10.1007/BF03257928.

[17] K. L. Chopra, P. D. Paulson, and V. Dutta. “Thin-film solar cells: an overview”. In: *Progress in Photovoltaics: Research and Applications* 12.2-3 (2004), pp. 69–92. DOI: 10.1002/pip.541.

[18] C. Gayner and K. K. Kar. “Recent advances in thermoelectric materials”. In: *Progress in Materials Science* 83 (2016), pp. 330–382. ISSN: 0079-6425. DOI: 10.1016/j.pmatsci.2016.07.002.

[19] N. I. Muhammad Nadzri, D. S. C. Halin, M. M. Al Bakri Abdullah, S. Joseph, M. A. A. Mohd Salleh, P. Vizureanu, D.-P. Burduhos-Nergis, and A. V. Sandu. “High-Entropy Alloy for Thin Film Application: A Review”. In: *Coatings* 12.12 (2022), p. 1842. ISSN: 2079-6412. DOI: 10.3390/coatings12121842.

[20] K. Cui and Y. Zhang. “High-Entropy Alloy Films”. In: *Coatings* 13.3 (2023), p. 635. ISSN: 2079-6412. DOI: 10.3390/coatings13030635.

[21] X. H. Yan, J. S. Li, W. R. Zhang, and Y. Zhang. “A brief review of high-entropy films”. In: *Materials Chemistry and Physics* 210 (2018). High-Entropy Materials, pp. 12–19. ISSN: 0254-0584. DOI: 10.1016/j.matchemphys.2017.07.078.

[22] R. K. Duchaniya, U. Pandel, and P. Rao. “Coatings based on high entropy alloys: An overview”. In: *Materials Today: Proceedings* 44 (2021), pp. 4467–4473. ISSN: 2214-7853. DOI: 10.1016/j.matpr.2020.10.720.

[23] B. Rice. “Extreme ultraviolet (EUV) lithography”. In: *Nanolithography*. Woodhead Publishing, 2014, pp. 42–79. ISBN: 978-0-85709-500-8. DOI: 10.1533/9780857098757.42.

[24] E. Louis, A. E. Yakshin, P. C. Goerts, S. Oestreich, R. Stuik, E. L. G. Maas, M. J. H. Kessels, F. Bijkerk, M. Haidl, S. Muellender, M. Mertin, D. Schmitz, F. Scholze, and G. Ulm. “Progress in Mo/Si multilayer coating technology for EUVL optics”. In: *Emerging Lithographic Technologies IV*. Vol. 3997. SPIE, 2000, pp. 406–411. DOI: 10.1117/12.390077.

[25] E. Louis, A. Yakshin, T. Tsarfati, and F. Bijkerk. “Nanometer interface and materials control for multilayer EUV-optical applications”. In: *Progress in Surface Science* 86.11 (2011), pp. 255–294. ISSN: 0079-6816. DOI: 10.1016/j.progsurf.2011.08.001.

[26] C. Sfiligoj. “Towards stable nanolayers for EUV optics”. PhD thesis. University of Amsterdam, 2021. URL: https://hdl.handle.net/11245.1/eb38c693-37b4-483f-9e07-fec239c7c132.

[27] G. Yetik. “Thermal stability of nanolayers for EUV optics”. PhD thesis. University of Amsterdam, 2023. URL: https://hdl.handle.net/11245.1/8031ab10-4564-4c88-9efc-e18edbb6c1bd.

[28] M. Hołyńska, A. Tighe, and C. Semprimoschnig. “Coatings and Thin Films for Spacecraft Thermo-Optical and Related Functional Applications”. In: *Advanced Materials Interfaces* 5.11 (2018), p. 1701644. DOI: 10.1002/admi.201701644.

[29] I. Levchenko, K. Bazaka, T. Belmonte, M. Keidar, and S. Xu. “Advanced Materials for Next-Generation Spacecraft”. In: *Advanced Materials* 30.50 (2018), p. 1802201. DOI: 10.1002/adma.201802201.

[30] NASA. *James Webb Space Telescope: Mirrors*. URL: https://webb.nasa.gov/content/observatory/ote/mirrors/index.html.

[31] R. A. Keski-Kuha, C. W. Bowers, M. A. Quijada, J. B. Heaney, B. Gallagher, A. McKay, and I. Stevenson. “James Webb Space Telescope optical telescope element mirror coatings”. In: *Space Telescopes and Instrumentation 2012: Optical, Infrared, and Millimeter Wave*. Vol. 8442. SPIE, 2012, 84422J. DOI: 10.1117/12.925470.

[32] T. W. Morgan, M. Balden, T. Schwarz-Selinger, Y. Li, T. H. Loewenhoff, M. Wirtz, S. Brezinsek, and G. D. Temmerman. “ITER monoblock performance under lifetime loading conditions in Magnum-PSI”. In: *Physica Scripta* 2020.T171 (2020), p. 014065. DOI: 10.1088/1402-4896/ab66df.

[33] Y. Jia, W. Liu, B. Xu, S. Qu, L. Shi, and T. Morgan. “Subsurface deuterium bubble formation in W due to low-energy high flux deuterium plasma exposure”. In: *Nuclear Fusion* 57.3 (2016), p. 034003. DOI: 10.1088/1741-4326/57/3/034003.

[34] P. Sigmund. “Mechanisms and theory of physical sputtering by particle impact”. In: *Nuclear Instruments and Methods in Physics Research Section B: Beam Interactions with Materials and Atoms* 27.1 (1987), pp. 1–20. ISSN: 0168-583X. DOI: 10.1016/0168-583X(87)90004-8.

[35] Y. Ueda, J. Coenen, G. De Temmerman, R. Doerner, J. Linke, V. Philipps, and E. Tsitrone. “Research status and issues of tungsten plasma facing materials for ITER and beyond”. In: *Fusion Engineering and Design* 89.7 (2014), pp. 901–906. ISSN: 0920-3796. DOI: 10.1016/j.fusengdes.2014.02.078.

[36] V. Tiron, I.-L. Velicu, C. Porosnicu, I. Burducea, P. Dinca, and P. Malinský. “Tungsten nitride coatings obtained by HiPIMS as plasma facing materials for fusion applications”. In: *Applied Surface Science* 416 (2017), pp. 878–884. ISSN: 0169-4332. DOI: 10.1016/j.apsusc.2017.04.183.

[37] S. Nogami, I. Ozawa, D. Asami, N. Matsuta, S. Nakabayashi, S. Baumgärtner, P. Lied, K. Yabuuchi, T. Miyazawa, Y. Kikuchi, M. Wirtz, M. Rieth, and A. Hasegawa. “Tungsten–tantalum alloys for fusion reactor applications”. In: *Journal of Nuclear Materials* 566 (2022), p. 153740. ISSN: 0022-3115. DOI: 10.1016/j.jnucmat.2022.153740.

[38] V. Tiron, G. Bulai, C. Costin, I.-L. Velicu, P. Dincă, D. Iancu, and I. Burducea. “Growth and characterization of W thin films with controlled Ne and Ar contents deposited by bipolar HiPIMS”. In: *Nuclear Materials and Energy* 29 (2021), p. 101091. ISSN: 2352-1791. DOI: 10.1016/j.nme.2021.101091.

1

A BRIEF REVIEW ON THIN-FILM DEPOSITION, GROWTH KINETICS, AND STRESS DEVELOPMENT IN COATINGS

1.1 THIN-FILM DEPOSITION TECHNIQUES

Several techniques have been developed to fabricate thin films, each offering unique advantages and capabilities. Physical vapor deposition (PVD) methods for thin-film fabrication are versatile, straightforward, and characterized by a controllable nature. In PVD, a solid material is vaporized via thermal or non-thermal processes; the evaporated species subsequently condense on a substrate, where the thin film grows. Specifically, PVD methods have proven very successful in depositing thin films of pure metals, alloys, semiconductors, and ceramics with application-oriented properties. In this thesis, metallic thin films have been deposited employing two of the most common PVD techniques, namely sputter deposition and pulsed laser deposition. Sputter deposition is a simple and reliable technique, excellent for producing high-quality layers of most common metals and alloys with well-defined characteristics. Pulsed laser deposition has been chosen due to its capability to enhance off-equilibrium and reactive growth, opening up new pathways in the fabrication of thin films with customized properties. In the next sections, the basic physical principles of these methods are presented, together with a brief discussion of the major advantages and drawbacks.

1.1.1 SPUTTER DEPOSITION

When considering PVD techniques for high-quality thin-film fabrication, sputter deposition stands out as a versatile, precise, and reliable method, employed both in fundamental research and industrial applications. For instance, in the semiconductor industry, it is currently used for metal interconnects, diffusion barriers, and passivation layers in integrated circuits and photovoltaics [1]. The optics and photonics sector relies on sputter deposition for the fabrication of optical coatings, including anti-reflective coatings and high-reflectivity mirrors [2].

Additionally, it finds application in the automotive industry for decorative coatings and anti-corrosion layers [3, 4]. Furthermore, sputter deposition plays a crucial role in the production of transparent conductive films for touchscreens, LCDs, and OLEDs [5]. Sputter deposition enables the fabrication of coatings with high level of purity, excellent uniformity and density over large areas, good adhesion, and conformity to the substrate [1].

The technique is based on the physical vaporization of atoms from the surface of a target material via momentum transfer of highly energetic particles, usually ions accelerated in an electric field [1, 6, 7]. A common sputter-deposition setup is schematically depicted in Figure 1.1. The target material and the substrate are facing each other in a vacuum chamber, with a typical base pressure in the range of 10^{-6}-10^{-8} mbar. The chamber is backfilled with a process gas, usually argon (Ar), with a pressure of up to a few mbar. Then, a negative electrical potential of several hundreds of volts is applied to the target (cathode), while the substrate is grounded (anode). In this configuration, free electrons are accelerated away from the target, colliding with the process gas atoms and causing their ionization to form positively charged ions (Ar^+). The latter are accelerated towards the cathode by the electric field, carrying enough kinetic energy to sputter atoms from the surface of the target, which are preferentially ejected in the direction of the substrate. Here, the evaporated material condenses to form a thin film. The characteristic light glow observed during the deposition process is the result of the Ar^+ ions recombining with free electrons, causing the emission of photons with a well-defined wavelength.

The sputter deposition process can be enhanced and optimized in several ways: an effective and well-established method is the implementation of magnetrons in the source [4, 8]. In this configuration, a magnetic field is applied parallel to the target surface, confining the electrons in the plasma near the surface (Figure 1.1). This has two main advantages: first, the plasma is concentrated and focused near the target, resulting in higher ion density, sputter-yield, and thus deposition rates [6, 8]. Secondly, negatively charged particles can be directed away from the substrate (e.g. highly ionized oxygen molecules), preventing contamination and improving the quality of the film [8]. Another variation of the method is reactive magnetron sputtering, where a small amount of a reactive gas (for example oxygen or nitrogen) is added to the process gas. The sputtered species will therefore form compounds upon ejection from the target and condense on the substrate to form thin films of composites such as oxides or nitrides [6].

The core of the sputter deposition technique is the interaction between the ions and the target surface. An impinging ion can sputter atoms and clusters, be reflected, penetrate, or be trapped in the material [9, 10]. In particular, the ions transfer energy to the target atoms via a series of elastic and inelastic collisions. Sputtering eventually occurs when the energy transfer from an ion is high enough to overcome the surface binding energy [9]. Parameters such as ion energy, atomic mass, binding energy, and preferential crystallographic orientation of the target strongly affect the sputtering yields [9, 11]. This is critical for the deposition of multi-element compounds like oxides and alloys, often resulting in

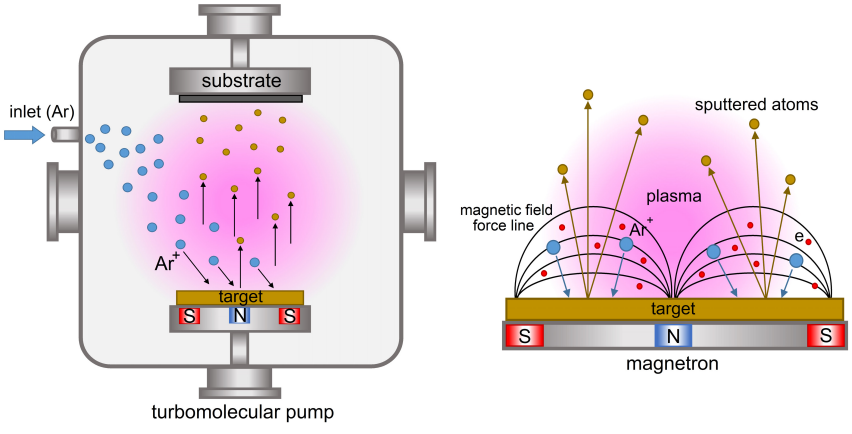

Figure 1.1 *(Left) Sketch of a typical sputter deposition setup: in a vacuum chamber backfilled with Ar, a strong negative electric potential is applied between target and substrate, causing the ionization of the process gas and the formation of a plasma. Positively charged Ar ions are accelerated towards the target, causing the sputtering of atoms, which are preferentially ejected towards the substrate. Here, the evaporated species condense and nucleate a thin film. (Right) Sketch of the magnetron sputter deposition configuration: a magnetic field is applied parallel to the target to enhance deposition rates and confine negatively charged species.*

large compositional variations between target and coating, a phenomenon referred to as 'preferential sputtering' [9]. In particular, the ion-target interaction governs the kinetic energy and angular distribution of the sputtered atoms [9, 11]. For common operating conditions, the energy of the ions generated in the plasma peaks at around 1 keV, leading to the sputtering of multiple target atoms with an average kinetic energy lying in the range of 1-10 eV [9, 11, 12]. Additionally, other parameters can influence the properties of the sputtered atoms. For instance, the ejected species crossing the distance between the target and substrate (typically a few cm) will further interact with the background process gas and plasma environment [1]. Scattering processes will occur at sufficiently high pressures (in the range of 10^{-2}-10^{-3} mbar), and result in a reduction of kinetic energy and spreading of the angular distribution of the emission [1, 12].

At the substrate, the kinetic energy of the incoming species combined with other deposition parameters such as the substrate temperature have a major impact on the film properties. For example, they strongly affect the adatom mobility, which in turn influences the morphology and microstructure of the coating [8]. In fact, at low mobility, the atoms impinging on the substrate will most likely remain close to the arriving location, having a low probability of overcoming the typical surface diffusion barrier. This leads to the formation of small crystallites with no preferential crystallographic orientation, resulting in low-density and rough films [8]. On the other hand, providing the system with more energy, for instance by increasing the kinetic energy of the incoming atoms and substrate

temperature, generally leads to increased mobility, which favors the growth of large, compact crystalline islands. The resulting films tend to be denser, smoother, and atomically-oriented, with a more complicated microstructure that depends on kinetically determined processes like cluster diffusion and grain boundary migration [8]. The ability to tune the coating microstructure during growth has a strong impact on various macroscopic material properties, such as hardness, ductility, tribological behavior, and corrosion resistance [13].

One of the main advantages of sputter deposition is the possibility to customize the setup geometry to specific requirements. Many crucial parameters for the film growth (namely energy fluxes and sputtering yields) are affected by geometrical factors such as anode size, configuration of the magnetic fields, and spacing between target (or substrate) and chamber walls [14]. Sputter deposition combines a long-lasting, geometrically-flexible source with high reproducibility and versatility, making it ideal for various in-line vacuum systems [1]. The latter is specifically one of the reasons why this technique is globally employed in industrial assembly and production lines. Moreover, other advantages are [1]: the flexibility in the choice of the target, as almost any solid material can be sputtered, including raw elements, alloys, and compounds; the possibility to perform large-area depositions (up to hundreds of cm^2) in specific configurations; and the option to incorporate techniques for *in-situ* surface preparation and monitoring. However, sputter deposition is also subject to some limitations: for instance, the growth of complex systems, namely multi-component alloys or oxides, is hindered not only by the size and number of the targets, which can be highly expensive, but also by the limited available parameters that can be tuned in the deposition process. In some cases, achieving the desired film properties such as correct stoichiometry or microstructure can be quite difficult. Moreover, the characteristic *atom-by-atom* growth and the relatively low energies involved in the deposition process make the stabilization of off-equilibrium phases challenging. In this framework, the constraints of the sputtering method could be overcome by other techniques. Pulsed laser deposition (PLD) is a good candidate to mitigate some of the limitations mentioned above, e.g. the ability to easily produce thin films in off-equilibrium phases, thanks to the wider range of growth possibilities.

1.1.2 PULSED LASER DEPOSITION

Among PVD techniques developed for thin-film growth, pulsed laser deposition has attracted considerable interest in the past few decades thanks to its versatility, reproducibility, and high level of control over the growth conditions [15]. The application of a laser-assisted deposition technique dates back to 1965 when its viability for optical thin-film deposition was first demonstrated [16]. Subsequently, the successful growth of high-quality epitaxial thin films of $Hg_{0.7}Cd_{0.3}Te$ in 1983 [17] and Y-Ba-Cu-based high-temperature oxide superconductor thin films in 1987 [18] marked the beginning of considerable advances in this field. Pulsed laser deposition has now evolved into a well-established method for growing high-quality thin films encompassing a wide variety of materials, including complex oxides,

metals and alloys, and semiconductors [19, 20].

Conceptually, pulsed laser deposition is a simple technique: Figure 1.2 depicts a schematic of the system and process. A high-intensity laser beam is focused on a stoichiometric target material located inside a vacuum chamber. If there is sufficient energy absorption at the chosen wavelength, the interaction between the laser and target leads to the ablation of the material and the formation of a plasma plume that expands away from the target, condensing on the substrate (Figure 1.2). Here, if optimal physical and chemical conditions are met, a stoichiometric thin film grows. Typical laser systems used in PLD are based on gas, such as KrF (λ=248 nm) and ArF (λ=193 nm) excimers, and solid-state materials, such as neodymium-doped yttrium aluminum garnet (Nd:YAG, λ=1064 nm). In these cases, the pulse duration varies between 10 ns and 25 ns, which has been proven to be an optimal range for target ablation, plasma formation, and subsequent thin-film growth [21]. While the concept may seem straightforward, the details of the physical processes that govern pulsed laser deposition are rather complicated. Three main steps can be identified: (i) laser beam interaction with the target material, (ii) plasma formation and expansion, and (iii) film nucleation and growth [21–23].

The laser light absorption by the target material is governed by various mechanisms, both thermal and non-thermal, occurring on different time scales. In this framework, the main non-thermal mechanism consists of electronic band transitions, i.e. the excitation of electrons by incoming photons. This process dominates the initial phase of the laser-target interaction. Excited electrons relax by rapidly transferring energy to the lattice via electron-phonon coupling, thus converting electronic excitations into thermal energy on a picosecond timescale. This leads to the fast heating of the material, which occurs within the optical absorption depth defined as $1/\alpha$, where α is the optical absorption coefficient. During this phase, for a typical ablation process in PLD, the temperature of the irradiated area on the target reaches several thousands of Kelvin, resulting in the surface local melting and evaporation. As a consequence, the material is ejected through a combination of electronic and thermal processes, and a dense vapor cloud is formed. Thermal energy causes material evaporation, while electronic excitations lead to the desorption of molecules and clusters. Therefore, in comparison to sputtering, laser ablation is the result of a solid-liquid-vapor transition.

The mechanisms of laser absorption and material evaporation typically occur in tens of picoseconds [21]. If the laser pulse duration is a few tens of nanoseconds, as is common for most PLD systems, the evaporated material further interacts with the laser beam. Incoming photons are absorbed in the initial vapor phase, promoting the generation of additional free electrons and ions by means of processes such as photoionization (electron ejection due to the absorption of a photon), and inverse Bremsstrahlung (electron excitation as a result of collisional energy transfer). This results in an increased level of ionization, and eventually leads to the formation of a plasma. The further absorption of the incoming photons increases the plasma temperature and density, resulting in the formation

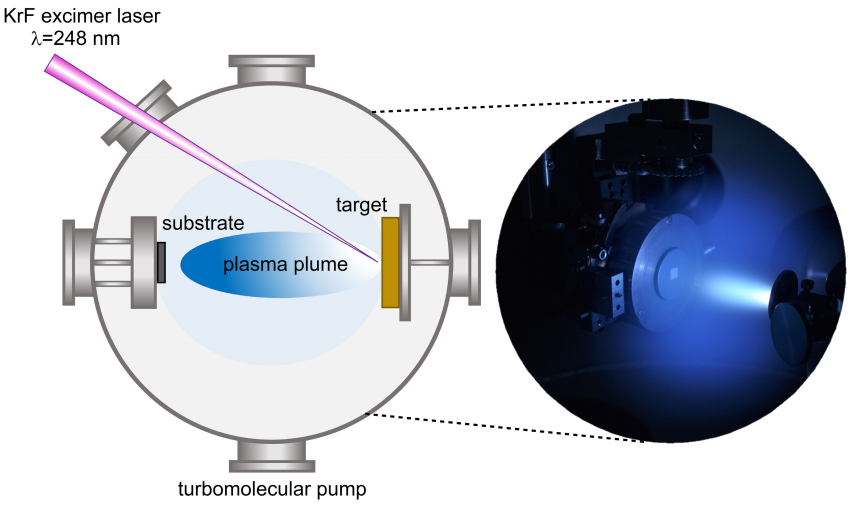

Figure 1.2 *(Left) Sketch of the pulsed laser deposition setup employed in this thesis: a high-intensity laser beam (here: KrF excimer with wavelength λ=248 nm) is focused on a target, resulting in the ablation of the material, the formation of a plasma plume and deposition onto a substrate. (Right) Photo of the plasma plume expanding from the target on the right towards the substrate on the left. The photo was taken during a thin-film deposition in the PLD setup at ARCNL (Credit: Roland Bliem).*

of the so-called *Knudsen layer* [21, 24]. In this near-surface region, the ejected species acquire a velocity distribution with a strong component perpendicular to the target surface, leading to the expansion of the plasma and the formation of the characteristic plume. The angular distribution of the plasma plume displays a $cos^n(\theta)$ dependency, where θ is the angle measured from the target surface normal and $4 < n < 30$, which depends on deposition parameters such as laser spot size and power density [24], and background pressure [21]. The ejected material comprises atoms, molecules, clusters, ions, and electrons, impinging on the substrate surface with typical kinetic energies ranging from a few tens of eV up to 100 eV. Incoming species will either diffuse on the surface and begin the film nucleation process, recoil, or desorb. After arrival at the surface, the growth of the film is influenced by parameters like substrate temperature and deposition rate, which for instance directly affect the surface diffusion mechanism and growth kinetics.

One of the main advantages of PLD is the remarkable control over film properties, thanks to the possibility of fine-tuning the deposition parameters to specific requirements. In particular, the main tunable parameters of the PLD process include (but are not limited to) laser fluence, background gas composition and pressure, substrate temperature, and target composition [21, 25]. In comparison with other techniques such as sputter deposition, the pulsed nature of PLD allows an increased degree of control on the film growth rate, while the high energy typical of the deposition process is expected to promote the stabilization of off-equilibrium

phases, such as nanocrystalline and amorphous structures. Additionally, it is possible to deposit films of compounds with volatile elements (such as complex oxides), and materials that are not suited for evaporation or sputtering (such as complex ceramics). Moreover, PLD allows for the deposition of thin films in a reactive environment, without the need for complex equipment inside the vacuum setup (the laser is located outside the vacuum and is independent of the environment). The deposition process is simple and does not require any gaseous precursors or additional equipment such as plasma sources or RF/DC power supplies, reducing the possibility of contamination and the total process time. The optimization of the growth parameters is mandatory to ensure good quality and reproducible thin-film depositions. In general, known trends based on previous reports in literature set the starting point of the growth recipe, but a detailed optimization is required to achieve high-quality films with desired properties. A more detailed discussion of the main PLD deposition parameters affecting the growth of metallic thin films investigated in this thesis can be found in the next section.

However, PLD also suffers from some drawbacks: for instance, the deposition rates are generally low compared to other techniques, and increasing the deposition rate without affecting the film quality can be challenging. Due to the relatively limited laser-target interaction area, scaling up PLD for large substrate depositions is difficult, although efforts are currently being made in this field for the mass production of micro- and nanoelectronic devices [26]. Additionally, laser ablation causes the formation of molten particles and target fragments, which are deposited on the substrate and affect the overall quality of the film (more details in the next section). Mitigation strategies are possible, like rotating mechanical filters installed in the target-substrate path, but might not be sufficient in case the requirements on the film quality are stringent. Overall, in this thesis, the choice of PLD as a fabrication technique instead of more traditional and well-established methods (like sputtering) has been dictated by the drive to develop more efficient pathways for materials design. Thanks to its unique capabilities, PLD allows a reproducible engineering of thin-film properties customized to specific requirements, opening up new opportunities for the deposition of innovative functional coatings.

1.1.3 PLD OF METALS AND ALLOYS

Nowadays, PLD is commonly used to grow functional thin films and heterostructures of complex oxides [27], for example in applications of the renewable energy sector (such as photovoltaics and energy storage). However, metals and alloys were among the first materials to be deposited as thin films with PLD [28]; similarly, this field has continued to progress and advance. In particular, several experiments showed that PLD allows to grow metallic alloys and multilayers with remarkable properties, different from the ones obtained with more conventional techniques such as sputtering or evaporation [29]. For instance, thanks to the rapid and highly-energetic nature of the PLD process, the system is in general prevented from reaching a thermodynamic equilibrium state. This allows the deposition of

alloys in off-equilibrium phases, such as fully amorphous structures over a wide range of compositions, supersaturated solid solutions of mixtures with very low solubility (e.g. Ni-Ag and Fe-Ag), and combinations of amorphous and crystalline phases [29–31]. In this context, laser-deposited alloy films are often more homogeneous than their sputtered or thermally-evaporated counterparts, which tend to decompose [29]. Moreover, the enhanced surface mobility allowed by the higher kinetic energies results in improved crystallographic orientation preference, with good *layer-by-layer* morphology and reduced number of defects [32, 33].

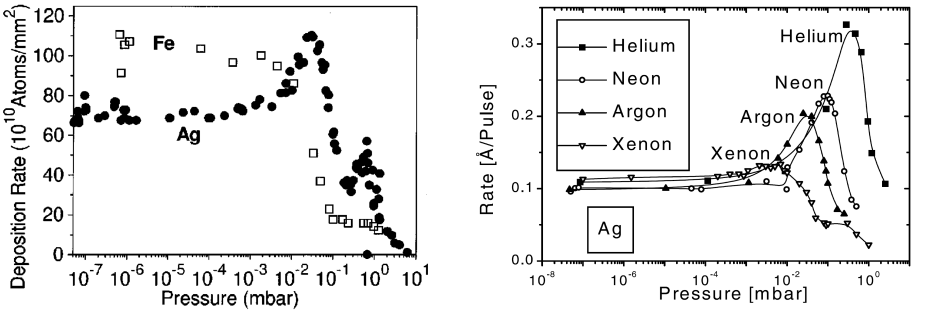

Figure 1.3 *(Left) Deposition rates of Fe and Ag as a function of Ar background pressure at a laser fluence of 4.5 J/cm^2; adapted from [34]. For Ag, the deposition rate increases to a maximum at 4.0×10^{-2} mbar: at this pressure, the mean free path of the ablated species is comparable with the target-substrate distance. The increase is ascribed to a reduction in kinetic energy of ablated Ag as a result of scattering with the Ar atoms, which reduces the sputter yield. On the other hand, the deposition rate of Fe displays a lower dependency on the background pressure, indicating a much smaller sputter yield. The decrease for pressures above 10^{-2} mbar is ascribed to the scattering of ablated Fe away from the target-substrate flight direction. (Right) Deposition rates of Ag under different inert gas atmospheres at a laser fluence of 6.0 J/cm^2; adapted from [35]. In all cases, the rate displays the same behavior of Ag deposited in Ar background pressure, i.e. an increase to a maximum with increasing pressure, and then a decrease. The atomic mass of the gas has a strong impact on the scattering efficiency, influencing the maximum value of the rate peak, and the pressure at which it occurs.*

One of the main (tunable) parameters that strongly influences the PLD process of metals and alloys is the background atmosphere (Figure 1.3). In particular, depositing the film in ultra-high vacuum (UHV) or inert gas atmosphere has a significant impact on the kinetic energies of the ablated species, the distribution of elements in the plume, and its shape. Ultra-high vacuum is generally preferred when the target material contains highly reactive elements such as Zr, which for example are easily oxidized even in a very low background pressure of water or oxygen (≈10^{-9}-10^{-10} mbar) [36], therefore impacting the purity of the film. However, one of the main drawbacks of UHV depositions is preferential resputtering effects caused by energetic species [29], which strongly affect the microstructure, the stoichiometric transfer between target and substrate, and the deposition rates

(Figure 1.3) [34, 35, 37]. On the other hand, depositing in an inert gas atmosphere reduces the kinetic energies of the ablated species due to the scattering of the plasma plume with the gas atoms. This is in general accompanied by a decrease in sputter yields and a change in deposition rates (Figure 1.3) [34, 35, 37]. In addition to background pressure, other parameters are relevant to achieve films with the desired properties, including laser fluence and repetition rate. For instance, above the ablation threshold, laser fluence affects the density and the kinetic energy of the ablated species, and the target morphology. This has strong consequences not only on the film thickness and microstructure (e.g. grain size and surface roughness) but also on the eventual formation and size of droplets [38, 39].

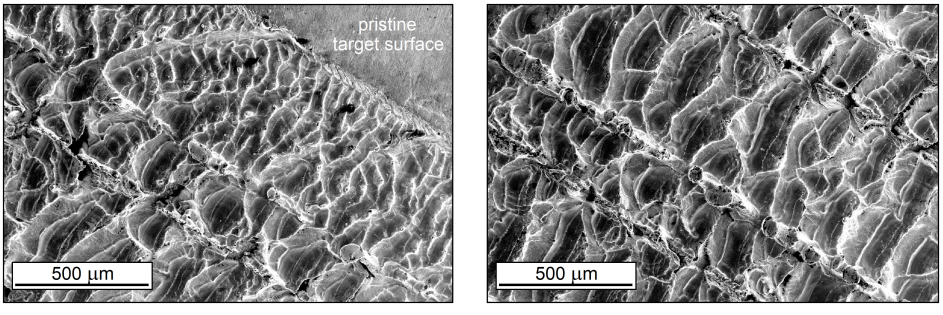

Figure 1.4 *Scanning electron microscopy (SEM) images of the surface of an HfMoNbTiZr high-entropy alloy target after several thousands of laser shots at a fluence of approximately 11.0 J/cm^2. (Left) The irradiated area shows a dramatic difference in roughness with respect to the pristine area in the top-right corner. (Right) Several protruding structures are observed on the irradiated target surface. These features are the result of the target melting-cooling cycles and can be eventually ejected as droplets and particulates during further exposure to laser shots.*

During deposition, together with atoms and ions, droplets with a diameter ranging from a few nm up to several μm are often deposited in low density on PLD-grown metallic thin films [29]. The formation of these droplets from solid metal targets is not avoidable, and it is considered one of the main drawbacks of PLD, limiting its use in commercial applications. The extent of this effect depends on the material and the properties of the target, such as roughness, morphology, and microstructure (Figure 1.4). The occurrence of droplets is mainly ascribed to hydrodynamic effects during laser-target interaction, namely subsurface boiling and recoil ejection, and the exfoliation process [22, 40]. The first two effects produce droplets via melt-ejection (also called 'splashing' phenomena), and they are in first approximation independent of the target morphology and are predominant in metals with low melting temperatures and high thermal conductivities (e.g. Al) [22]. On the other hand, the exfoliation effect relates to the ejection of droplets due to the increased surface roughening of the target during deposition (Figure 1.4). The target surface undergoes repeated melting-cooling cycles that lead to the formation of protruding structures (Figure 1.4), which eventually break

off upon further exposure to laser shots and can be ejected as particulate [22]. To mitigate the deposition of droplets, several approaches can be implemented: mechanical polishing of the target surface, for example, dramatically reduces the total number and average size of the droplets [36]. In addition, optimizing the deposition parameters, in particular fluence, background gas, and target-sample distance, has also been proven effective [29, 41]. Finally, thin films with a low level of droplets can be achieved by modifying the experimental setup and its geometry, with the implementation of dedicated mechanical velocity filters and shutters [42, 43], or even by using molten targets instead of solid ones [44].

In the context of this thesis, PLD has been chosen to explore novel pathways of materials design, going beyond some of the limitations of conventional deposition methods, like their tendency to produce ordered structures at room temperature. The unique capabilities offered by PLD, such as the level of control on specific deposition parameters, and the possibility of stabilizing off-equilibrium phases, allow a fine-tuning of material properties at the nanoscale and result in improved macroscopic performances. For instance, the atomic structure of metallic coatings plays a key role in specific applications, such as protective layers against corrosion, optical transparency, hardness, and conductivity [45–48]. The off-equilibrium regime of PLD enables control over the film structure at the atomic level, ranging from fully amorphous to crystalline to a combination of both, decoupling the widely observed co-dependence of structure and stoichiometry in alloys [36].

1.2 GROWTH KINETICS

The formation of a thin film on a solid surface is a complicated process, governed by different growth stages [49–51]. In thin-film deposition, the final macroscopic state is not necessarily the energetically most favorable one: the growth can proceed via various mechanisms, and the particular pathway taken determines the ultimate macroscopic state [49]. Thus, thin-film growth is characterized by a non-equilibrium nature, resulting from a competition between kinetics and thermodynamics [49–53]. In this context, growth kinetics involves atomistic processes such as surface adsorption, diffusion, and nucleation, each described by characteristic time scales and activation energies. During film deposition, some processes are kinetically limited, while others can be manipulated to enforce a particular growth behavior. This is in contrast with thermodynamics, which defines the equilibrium state at specific conditions so that all processes are in balance and occur in opposite directions with equal rates [49]. On the one hand, the thermodynamic aspect is influenced by parameters such as the free energy of the surface, substrate and substrate/film interface, and degree of supersaturation (defined as $S = p/p_e$, where p is the vapor pressure of the impinging species and p_e is the equilibrium vapor pressure at the substrate temperature). On the other hand, the kinetic contribution is influenced by factors like deposition flux, surface and interlayer diffusion, nucleation rate, and substrate morphology (i.e. presence/absence of defects, roughness, texture, and local atomic arrangements) [49, 52, 54, 55].

In the context of thin-film deposition, the common approach is to identify three main equilibrium growth modes, namely two-dimensional (2D), or *layer-by-layer* growth (Frank-van der Merwe mode); three-dimensional (3D), or *island* growth (Volmer-Weber mode); and a combination of 2D plus 3D, or *layer-plus-island* growth (Stranski-Krastanov mode) [49, 50, 55]. A cross-sectional view of layers growing in these modes is sketched in Figure 1.5. In general, thermodynamic considerations allow to qualitatively understand the energetic trends favoring one mode over the others. For instance, 2D growth and wetting occur when the drop in Gibbs free energy is largest if the deposited atoms bond to the substrate. Conversely, island formation (3D) is preferred if the Gibbs free energy is lowest when the atoms bond with each other [52, 55]. During deposition, however, the system is further influenced by other factors like stress buildup, and the most favorable growth mode might shift from 2D to 3D after the initial stages of film formation (*layer-plus-island* mode) [52]. The details of the growth mode directly affect important film properties at the nanoscale, such as microstructure and morphology, which have a dramatic effect on the coatings' macroscopic behavior and performance [56]. Therefore, the ability to control and tailor the nucleation and growth mode during deposition can be a pathway to customize thin-film properties. On the one hand, thermodynamics defines the energetic preference, favoring the ground-state structure and the equilibrium stoichiometry for the given combination of film, substrate, and growth conditions. On the other hand, kinetics can be leveraged to force the system away from equilibrium, allowing the formation of disordered or metastable phases. Thermodynamic preferences are generally difficult to influence since they depend on the specific system chosen (e.g. substrate and material to be deposited), while the manipulation of kinetics is, on the contrary, attainable through modification of the growth parameters [49, 52].

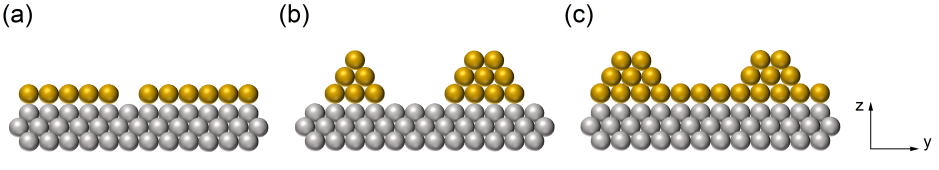

Figure 1.5 *Sketch illustrating a cross-sectional view of the three main thin-film growth modes: (a) Two-dimensional (2D), or layer-by-layer growth (Frank-van der Merwe mode); (b)Three-dimensional (3D), or island growth (Volmer-Weber mode); (c) 2D plus 3D growth (Stranski-Krastanov mode). The gray spheres represent the atoms of the substrate, while the gold spheres represent the atoms of the deposited material.*

The most important kinetic mechanisms in thin-film deposition include adatom diffusion, nucleation, and interlayer mass transport [57]. The nature of these processes can be understood by considering the case of epitaxial growth from the vapor phase. The terrace-step-kink (TSK) model of a surface gives a good illustration of the entities involved in the process [58, 59]. In Figure 1.6, the main elements of the TSK model are schematically displayed for a simple cubic crystal

surface. One of the key processes, adatom diffusion, can be described in terms of a jumping process between adsorption sites on a 2D lattice [55, 60]. In this framework, a surface diffusion coefficient can be introduced:

$$D = a^2 k_S \tag{1.1}$$

Where a is the hopping distance between atomic sites, and k_S is the site-to-site adatom hopping rate [57]. By defining a potential energy barrier V_S between sites, the rate k_S can be expressed as:

$$k_S = \nu \times exp\left(-\frac{V_S}{k_B T}\right) \tag{1.2}$$

Where ν is the attempt frequency, T is the temperature of the substrate, and k_B is the Boltzmann constant. The mean square displacement of diffusing adatoms can be mathematically described with Random-walk statistics:

$$\langle \Delta r^2 \rangle \sim Dt \tag{1.3}$$

For a flat surface, and at a constant deposition rate, the coefficient D determines the average distance an adatom travels before joining an island or meeting another adatom to nucleate a new island [57]. As nucleation proceeds, this distance decreases progressively until it becomes approximately constant in the steady-state regime. The island density N on the surface is then intuitively proportional to F^p/D^q, where F is the deposition rate and p, q are positive exponents that depend on the specific growth processes [61, 62]. Given the importance of D in kinetic processes, great effort has been dedicated to infer its value precisely. For instance, scanning tunneling microscopy (STM) experiments allow to extract the surface diffusion coefficient by counting the number of islands formed as a function of time and deposition rate, and by directly measuring the adatoms' mean square displacement $\langle \Delta r^2 \rangle$ [63].

When diffusing adatoms meet and join, they nucleate to form an island (Figure 1.6). The stability of a newly-formed island depends on competing mechanisms, which are directly or indirectly influenced by the growth parameters, such as substrate temperature and deposition rate [57]. An island is stable if it exceeds a critical size i. In a simple nucleation model [64], a set of rate equations can be defined, describing the processes an adatom can follow upon landing on the substrate, like diffuse on the surface, evaporate, nucleate, get captured by (and detach from) an existing island. Such equations can be used to determine the evolution of the number of atoms in an island as a function of time. In this context, factors like the diffusion coefficient and the (lateral) bonding energy between adatoms play an important role. For instance, at typical film growth conditions, the deposition flux and supersaturation are high, and, if the temperature is low enough, the lateral atomic bonds are strong enough to have i=1, i.e. two adatoms form a stable island: this case is also defined as irreversible nucleation [64–66]. Conversely, higher thermal energy (i.e. high substrate temperature) leads to

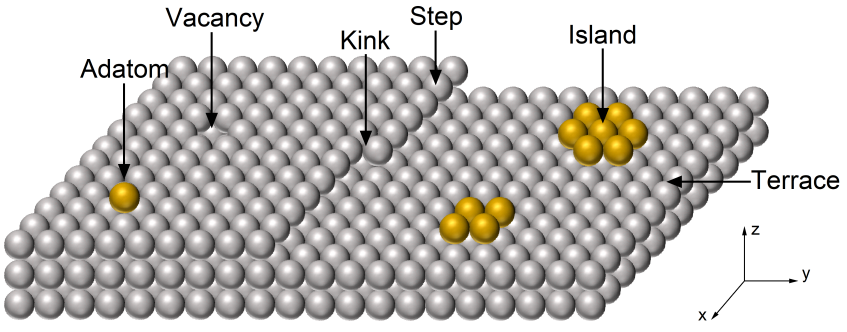

Figure 1.6 *Sketch illustrating the terrace-step-kink (TSK) model applied to a simple cubic crystal surface. The gray spheres represent the atoms of the substrate, while the gold spheres represent adsorbed atoms from the vapor phase. The figure defines the main entities of the TSK model, namely geometric elements such as terraces, steps, and kinks, crystallographic defects like substrate vacancies, and diffusing adatoms and islands.*

more probable bond-breaking events, thus driving dissociation and leading to an increased critical island size [64, 67].

As adatoms continue to diffuse, the islands grow in size, developing different morphologies. Two main categories of island growth patterns can be identified, namely compact and fractal [57]. In the first case, an ideal island assumes a geometric pattern, such as square, triangular, or hexagonal (the texture and structural preference of the substrate also plays an important role in the preferred arrangement), with well-defined and straight edges. In the second case, the island is highly anisotropic, and it is characterized by disordered and rough edges. The substrate temperature determines the degree of compactness, which directly affects the average adatoms' diffusion length: the higher the temperature, the higher the average diffusion length and the more compact and larger the islands [68]. Moreover, the temperature influences the adatoms' ability to move along the edges and across the corners of adjacent islands to find an energetically favorable site [57, 68]. For instance, at sufficiently high substrate temperature, the adatoms can diffuse along and in between islands to minimize the total free energy, relaxing at high coordination sites (bond saturation), and increasing the degree of compactness. However, as mentioned previously, thermal energy also acts as a destabilizing factor, and atoms can become more active, particularly at lower coordination sites (like edges and corners). This leads to additional island dynamic mechanisms, such as island diffusion, i.e. a displacement of the islands' center of mass, and island ripening, i.e. a redistribution of the total mass in an island and between different islands [64, 69].

After the initial stages of growth, when the density and size of the islands on the substrate terraces are sufficiently large, there is a significant probability that impinging atoms will land on top of an existing island. The interactions between atoms in the vertical direction are typically controlled by the rate of interlayer

mass transport, or interlayer diffusion, which regulates the uniformity of the film as the thickness increases [57]. An additional potential energy barrier can be defined [70], preventing the atom from hopping off the island and moving to the lower level. This happens because the atom would reduce its level of coordination, thus increasing its free energy, by leaving the top of the island before lowering it by bonding to a favorable site at the lower terrace [71]. The probability *P(t)* that an adatom remains on the surface of an island has a complicated dependency on the island radius, the adatom diffusion coefficient, and the competition between the step-edge barrier and surface diffusion barrier [72]. In general, interlayer mass transport can be enhanced in various ways, for example, by modifying the interplay between surface diffusion and step-edge crossing with increased temperature (i.e. increased mobility) [72, 73]. Interlayer mass transport plays an important role in determining the film morphology and microstructure [57, 71–73]. In particular, the step-edge energy barrier is critical for 3D (*island*) or 2D (*layer-by-layer*) growth. If such a barrier is comparable with the island surface diffusion barrier, a 2D growth is favored: the atoms on top of the island can easily move to the lower level, thus preventing the formation of additional stable islands (or layers) on top of an already existing one [71–74]. Conversely, if the diffusion term dominates over the step-edge crossing one, a multilayer 3D growth is favored [71–74]. The effect that interlayer mass transport has on film morphology can be decisive for the transition from smooth (in the case of 2D) to rough (in the case of 3D) growth [57, 73].

As mentioned above, in contrast to thermodynamics, kinetics is determined by the growth conditions. This opens pathways to modify the macroscopic outcome of the deposition by changing the growth method and parameters (e.g. growth rate and substrate temperature). For instance, supplying energy via sample temperature (global effect), or via kinetic energy of the impinging particles (local effect), gives control over the proximity to equilibrium growth and the atomistic processes atoms are allowed to follow, such as surface diffusion and nucleation. Kinetics can thus be used to modify the film properties, for instance by imposing/preventing a specific growth mode, or by favoring a characteristic morphology of the deposited material [52]. The typical evolution of the film microstructure as a function of the deposition temperature (T_S) is a good example [50, 56]. At a very low T_S with respect to the material's melting point, the adatom surface diffusion is negligible. The corresponding low mobility results in a film microstructure characterized by small crystalline grains forming a coarse, fractal, and porous texture [56, 75]. The extreme case of this regime far from equilibrium is the growth of fully disordered (or amorphous) structures. At higher deposition temperatures, surface diffusion becomes more and more relevant, leading to the formation of larger crystalline grains, with a denser, more compact morphology [56].

In metallic coatings, for example, this difference has a dramatic impact on mechanical properties, such as hardness, which is directly influenced by grain size and grain boundary behavior [76]. Tuning the substrate temperature is not the only method to modify the film microstructure. As previously mentioned, in PVD the kinetic energy of the impinging atoms plays an important role in determining the film properties [52]. For instance, in the growth of superconducting alloy

thin films, increasing the kinetic energies of the elemental species leads to increased mobility and higher local order and homogeneity, which results in a reduced detrimental impact on grain boundaries and improved superconducting behavior [77]. Moreover, in pulsed-laser-deposited thin films, high fluence leads to increased adatom kinetic energies and mobility, accelerating nucleation and directly affecting the morphology. This aspect has been for instance exploited to enhance coalescence and tune the porosity of PLD-grown oxides for applications in catalysis, sensors, and electrodes [78]. This demonstrate how kinetic mechanisms can be leveraged as additional tunable parameters in thin-film technology, emphasizing the potential of controlling growth kinetics to produce coatings with customized properties.

1.3 STRESS

Stress is present in all thin films. It originate from the fact that the atoms in a coating are not in their preferred bulk-like environment, owing to the non-equilibrium nature of the deposition process, substrate effects, and imperfections arising during growth [79]. Consequently, stress buildup is an integral part of thin-film deposition. The role of stress is decisive for coating properties, influencing the performance in technological applications [80]. For instance, high tensile stress can cause film cracking [81], while strong compressive stress can lead to film buckling, blistering, and delamination [79, 82, 83]. Excessive stress in the layers of interconnects and electrodes can form undesired deformations, resulting for example in short-circuit failures in microprocessors and electronic devices [80, 84]. Achieving a complete understanding of stresses in thin films is not straightforward, and a general theory is not available. It is well-known that many parameters strongly affect the evolution of stress, for example growth rate, temperature, microstructure, and grain boundary effects [79, 80, 85]. In this framework, two main groups of stresses can be identified, namely 'internal' (or intrinsic), and 'external' stresses [86]. The first ones build up during film growth and nucleation and can have various causes, like modifications of atomic structure and chemical composition, and growth mode. The second group includes stresses that occur after deposition, caused by external factors like changes in temperature, application of electromagnetic fields, and mechanical influences such as bending, pulling, and compression [86].

Internal stresses are by far the most studied. Internal stress is defined as the existence of a state of stress in the absence of external factors [85]. Several studies have demonstrated that internal stresses arise due to a complex combination of simultaneous causes, mainly ascribed to structural modifications in the deposited film [80, 85]. Such modifications can occur at the micro- or nanoscale, for instance by the creation of voids located at the grain boundaries or in between grain columns, and at the atomic scale, for example via the presence of dislocations and impurities [85]. A good example of atomic-scale stresses can be found in the domain of epitaxially grown films. If the substrate and deposited material have different lattice parameters, the corresponding mismatch in lattice constants

generates tensile or compressive stress, depending on the particular film/substrate system (*mismatch stress*). During the initial stages of growth, the atoms depositing on the surface will bond with the exposed atoms of the substrate. If the difference in lattice constants is significant, the atoms of the first layer will be under stress, and the layer itself will thus be strained [85]. As deposition continues, the first (strained) layer becomes the template for the additional film layers, which, as a result, will experience the same type of stress [85].

In epitaxial growth, the accumulated stress can be released through various mechanisms. For instance, a network of dislocations and mechanical faults (like fissures and voids) can form and propagate at the interface between film and substrate [86]. Furthermore, film relaxation leads to the formation of wrinkles, distortions, and grooves, which first affect the thickness and surface roughness, but can eventually break the continuity of the coating [86–88]. In addition, as briefly discussed in the previous section, stress release during heteroepitaxial deposition can modify the film growth mode. This is particularly valid for systems with strong lattice mismatch, where after the initial *layer-by-layer* growth, a significant amount of stress builds up in-plane. At this stage, the film lowers its total energy by forming isolated protrusions on the surface, which increase in size as deposition continues, resulting in the transition to the *2D plus 3D* growth mode [86, 89].

For polycrystalline films, where no well-defined epitaxial relation prevails, the discussion about stresses is more difficult, given the increased level of complexity and the higher number of contributing factors, such as additional surface orientations and interfaces given by the presence of grains. In this case, the surface (or interface) stress can be defined as follows [90]. By considering a surface area A, the work dW required to create new surface area dA can be expressed as:

$$dW = \gamma dA \tag{1.4}$$

Where γ is the surface (or interface) energy (also called surface tension). A variation in surface area dA without modification of the number of lattice sites is achieved via an elastic strain $d\epsilon_{ij}$ along the surface [91]. The work required to increase the area A via elastic strain is performed by the surface stress f_{ij}, which can be written as [90, 92]:

$$f_{ij} = \gamma\delta_{ij} + \frac{\partial\gamma}{\partial\epsilon_{ij}} \tag{1.5}$$

Where δ_{ij} is the Kronecker delta. The first term takes into account a change in area due to elastic deformation, while the second term takes into account a change in surface energy with elastic strain. The elements in Equation 1.5 (and their signs) cannot always be determined *a priori*, but they depend on the interatomic interactions (attractive or repulsive) and the morphology/structure of the surface under consideration (such as the presence of ledges or dislocations). Intuitively, surface stress acts as a stretched or compressed 'membrane' applying lateral forces in the surface plane [90].

The surface stress in films and multilayers can be measured in different ways. For instance, by depositing the coating on a thin substrate, and determining

the force per unit of width *F/w* that the film exerts on the substrate from the variation of the radius of curvature. Some examples of substrates for this purpose include free-standing membranes and cantilevers [90]. The stress evolution can be monitored during deposition by measuring the substrate curvature as a function of time and at a constant deposition rate. In this case, the quantity *F/w* can be defined as [90]:

$$\frac{F}{w} = \frac{1}{6} Y_S {t_S}^2 \frac{1}{R} = \langle \sigma \rangle t_F + N f \tag{1.6}$$

Where Y_S, t_S, and R are the biaxial modulus, the thickness, and the radius of curvature of the substrate, while $\langle \sigma \rangle$ is the average film stress, t_F is the thickness of the film, N is the number of interfaces (in the case of a multilayer), and f is the surface stress. A typical curve of *F/w* as a function of deposition time (or average film thickness) for a film following *island* growth mode is reported in Figure 1.7: after an initial compressive behavior (*F/w < 0*), the stress turns to tensile (*F/w > 0*) and reaches a maximum before turning again to incremental compressive [90].

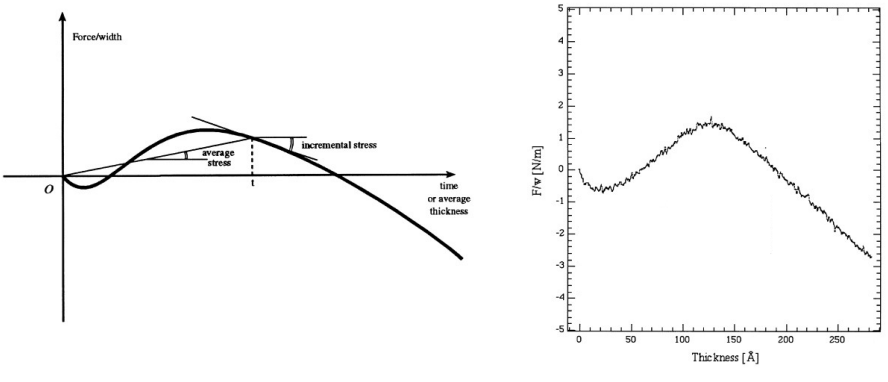

Figure 1.7 *(Left) Typical curve of the force per unit of width F/w exerted by the film on a curved substrate, as a function of deposition time (or thickness), adapted from [90]. (Right) F/w curve obtained during continuous deposition of a Cu film, adapted from [90, 93].*

The magnitude of stresses and even their nature (e.g. from tensile to compressive and *vice versa*) can vary at different growth stages [86, 90]. For instance, during *island* growth and before coalescence, compressive stress tends to develop in films. This has been observed experimentally by detecting a positive substrate curvature in the initial stages of film deposition. In this case, an island on the substrate can be approximated as a spherical cluster. Similarly to a droplet of liquid, where the surface tension determines a pressure difference Δp between the inside and outside of the droplet (termed *Laplace pressure*), for a solid particle the mechanical action of the surface is determined by the surface stress, and Δp can be defined as [90, 94]:

$$\Delta p = \frac{2f}{r} \tag{1.7}$$

Where r is the radius of the cluster, and f is the surface stress. Therefore, the surface stress plays a fundamental role in determining if the island would be under compression ($f < 0$) or tension ($f > 0$), depending on the sign of f, which is not determined *a priori*. The island will then exert a mechanical action on the substrate, influencing its curvature, which can be written as [90]:

$$\frac{1}{R} \propto -4 f sin^2(\theta) \tag{1.8}$$

Where θ is the wetting angle of the island. The experimental observation of an initial positive substrate curvature ($R > 0$) for many samples showing island growth indicates that, within this framework, the surface stress is indeed compressive ($f < 0$) [90]. It has been proposed that this is caused by the mismatch with the substrate in-plane lattice, which keeps an island above a critical size from reaching its equilibrium bulk lattice spacing. This is valid mostly for materials with smaller in-plane lattice spacing with respect to the bulk, which applies to many examples of low-index metallic surfaces on ceramic substrates [94]. Another possible explanation involves the interaction between adatoms and the substrate surface [95]. In this view, the adatom is attracted to the surface to maximize its level of coordination, generating an elastic displacement of the atoms of the substrate away from their equilibrium position, thus leading to the development of compressive stress. During the initial stage of deposition, the rate of increase in adatom population on the surface is large, and it decays as soon as a steady state is reached. The substrate will therefore experience an initial compressive stress that rapidly reaches zero, as observed in many experiments.

When islands grow in size and eventually coalesce in a continuous film, the nature of the stress tends to switch to tensile (Figure 1.7). This arises from the fact that, as grains come into contact with each other, the external surfaces are 'zipped together' to form a grain boundary [90, 96]. Within a global energetic framework, the free energies of the grain surfaces and grain boundaries determine the tensile stress developing in the film: the total energy is reduced by stretching the grains during coalescence and by replacing two surfaces with one grain boundary, while the energy cost due to stress is increased [96]. After the completion of the 'zipping' process, the crystallite size determines the length of the grain boundary and the average stress. For small grains, the interfacial forces are strong enough to completely close the gap between the grain surfaces. Conversely, for larger grains, only small sections of the grains are 'zipped together' to form a continuous film [96].

After the initial growth stages, when the film reaches continuity, stress depends on factors like deposition conditions and the particular materials involved, and it is usually the result of a complex interplay not only between competing tensile and compressive effects but also between different relaxation mechanisms [86]. In continuous polycrystalline films, adatom mobility for diffusion is an important parameter in determining the nature of internal stress [86]. As noted in the previous section, this factor is typically described in terms of the ratio between the deposition temperature T_S and the material's melting point T_M. When the

adatom mobility for diffusion is low ($T_S/T_M < 0.2$), tensile stresses due to crystallite coalescence tend to keep increasing linearly with increasing thickness. On the contrary, when the adatom mobility for diffusion is higher (or the deposition rate is lower), a transition in internal stress from tensile to compressive is observed as deposition continues [97]. In the low-mobility case, after island coalescence, the additional layers of the film grow on top of already formed grains (columnar growth), without recrystallization or long-range diffusion processes. Consequently, the grain boundary volume keeps increasing linearly with thickness, and the same occurs for the tensile stress [86, 98].

The case of compressive stress arising after the tensile stage at increased diffusion mobility is still not fully understood, and a complete theory is currently missing [86]. A model based on kinetic considerations has been recently developed, and was proven successful in explaining most of the experimental findings [86, 99]. The tensile stress characteristic of the coalescence growth stage can turn to compressive by atom diffusion from the surface into the grain boundaries. When the flux of insertion becomes significant, an excessive amount of atoms are embedded into the grain boundaries, and compressive stress becomes dominating [99]. According to the model, the driving force of this process is the free energy difference between the two atomic sites considered, i.e. on the surface and inside the grain boundary. This difference is a consequence of the fact that the surface and grain boundaries are not in their equilibrium state during growth. The energy on the surface increases due to supersaturation or modifications in surface morphology, with the creation of high-energy terraces. Similarly, the energy in the grain boundary decreases from its equilibrium value: if tensile stress is present, atoms will tend to move into the grain boundary to relieve it [99]. The dependence of internal compressive stress on parameters like surface diffusion (i.e. mobility) and growth temperature can therefore be explained using a kinetic model applied to a system where only two atomic sites are available (on the surface and inside the grain boundary), separated by an activation barrier [99]. The model also allows to give qualitative insight into variations of film properties, for example microstructure and morphology of the grain surfaces, which are the result of the competition between tensile and compressive stresses determined by grain boundary diffusion [100, 101].

Furthermore, tensile stresses can also become dominant over compressive ones in thin films characterized by high mobility. In this case, as the film continues growing, the number of grain boundaries decreases. The free volume is therefore reduced and redistributed, and the film tends to become more compact by reducing its size [86]. Since the film is bound to the substrate, this densification leads to the development of in-plane tensile stress [86, 102]. If such tensile stress becomes excessively high, further grain growth can be inhibited, and the formation of a fine-grained microstructure is observed [86, 102].

The second class of stresses develops under the influence of external forces after the growth of the film is completed. This class includes stresses arising due to thermal effects, application of electromagnetic fields, variations in chemical composition and microstructure, and mechanical modifications [86]. Here, thermal

stresses caused by temperature changes after deposition are discussed in more detail, since they are most relevant for the research presented in the next chapter. A common reason for thermal stresses to develop is the difference in coefficients of thermal expansion (CTE) between film and substrate [86]. For instance, most metals have a CTE at least one order of magnitude higher than most semiconductor substrates like silicon. In this case, once the deposition of a metal on silicon at elevated temperature is completed and the system cools down, the film experiences a greater reduction in size than the substrate. As a result, tensile stress develops in the film to match the substrate. If the system is annealed above the deposition temperature, the reverse effect takes place, and the film experiences compressive stress [86]. If the substrate has higher CTE than the film (which is commonly the case for an oxide or ceramic coating deposited onto a metal), the development of stresses is inverted with respect to the previous case.

When thermal stresses become strong, eventually exceeding the elastic limit of the film, they are relaxed through microstructural deformations, such as dislocations glide, diffusional creep, and shrinkage [103]. The resulting change in properties is not necessarily negative, but can also be exploited intentionally to improve characteristics dedicated to the material's application [104]. For instance, three-dimensional microstructures such as flow sensors and actuators can be fabricated by depositing multilayers of different materials, each characterized by a different CTE [105]. Moreover, thermal treatments can indirectly lead to stress development by enabling interface diffusion and intermixing. An example is the formation of metal silicides by annealing a metallic thin film deposited onto a Si substrate. The formation of the new compound from the initial elements is typically accompanied by a significant modification in volume, which is accommodated by an increase in thickness. The consequent buildup of compressive stress in the film can be released through various mechanisms, like delamination and plastic deformations [104, 106].

The stress level in thin films is a key property that directly affects their performance. Understanding the origin of stress and controlling its level is thus essential for the fabrication of reliable films in devices. In particular, intentional modification of stress serves as an additional pathway to modify the capabilities of functional coatings [105]. For instance, the manipulation of internal stresses allows for the fabrication of stress-induced out-of-plane nanostructures, such as bending cantilevers, nanotubes and helices, buckled ribbons, and membranes [105]. Applications of such nanostructures can be found in the domain of sensors, optical systems, protective pellicles, robotics, MEMS/NEMS devices, and wearable electronics [105]. Along these themes, chapter 2 describes an example of a stress-based modification, resulting in the formation of versatile centimeter-sized free-standing nanolayers, produced via post-deposition annealing of Ru thin films on Si substrates [104]. These examples show the importance of connecting the fundamental understanding of stress at the nanoscale to application-oriented macroscopic properties, emphasizing its relevance in modern-day thin-film technology.

REFERENCES

[1] D. M. Mattox. “Physical Sputtering and Sputter Deposition (Sputtering)”. In: *Handbook of Physical Vapor Deposition (PVD) Processing (Second Edition)*. Second Edition. William Andrew Publishing, 2010, pp. 237–286. ISBN: 978-0-8155-2037-5. DOI: 10.1016/B978-0-8155-2037-5.00007-1.

[2] M. M. Singh, G. Vijaya, M. Krupashankara, B. Sridhara, and T. Shridhara. “Studies on Thin Film Multilayer Coatings Deposited using Sputtering Process”. In: *Materials Today: Proceedings* 5 (2018), pp. 2994–2999. ISSN: 2214-7853. DOI: 10.1016/j.matpr.2018.01.098.

[3] E. Carneiro, N. M. G. Parreira, T. Vuchkov, A. Cavaleiro, J. Ferreira, M. Andritschky, and S. Carvalho. “Cr-Based Sputtered Decorative Coatings for Automotive Industry”. In: *Materials* 14.19 (2021), p. 5527. ISSN: 1996-1944. DOI: 10.3390/ma14195527.

[4] J. E. Greene. “Review Article: Tracing the recorded history of thin-film sputter deposition: From the 1800s to 2017”. In: *Journal of Vacuum Science and Technology A* 35.5 (2017), p. 05C204. ISSN: 0734-2101. DOI: 10.1116/1.4998940.

[5] E. Aydin, C. Altinkaya, Y. Smirnov, M. A. Yaqin, K. P. Zanoni, A. Paliwal, Y. Firdaus, T. G. Allen, T. D. Anthopoulos, H. J. Bolink, M. Morales-Masis, and S. De Wolf. “Sputtered transparent electrodes for optoelectronic devices: Induced damage and mitigation strategies”. In: *Matter* 4.11 (2021), pp. 3549–3584. ISSN: 2590-2385. DOI: 10.1016/j.matt.2021.09.021.

[6] A. Sarangan. “Nanofabrication”. In: *Fundamentals and Applications of Nanophotonics*. Woodhead Publishing, 2016, pp. 149–184. ISBN: 978-1-78242-464-2. DOI: 10.1016/B978-1-78242-464-2.00005-1.

[7] M. Ohring. “Discharges, Plasmas, and Ion–Surface Interactions”. In: *Materials Science of Thin Films*. Second Edition. Academic Press, 2002, pp. 145–202. ISBN: 978-0-12-524975-1. DOI: 10.1016/B978-012524975-1/50007-0.

[8] D. Depla, S. Mahieu, and J. Greene. “Chapter 5 - Sputter Deposition Processes”. In: *Handbook of Deposition Technologies for Films and Coatings*. Third Edition. William Andrew Publishing, 2010, pp. 253–296. ISBN: 978-0-8155-2031-3. DOI: 10.1016/B978-0-8155-2031-3.00005-3.

[9] Y. Taga and R. Takahasi. “Role of kinetic energy of sputtered particles in thin film formation”. In: *Surface Science* 386.1 (1997), pp. 231–240. ISSN: 0039-6028. DOI: 10.1016/S0039-6028(97)00313-0.

[10] R. Behrisch. *Sputtering by Particle Bombardment I.* Springer Berlin, Heidelberg, 1981. ISBN: 978-3-662-30888-2. DOI: 10.1007/3-540-10521-2.

[11] "Physics of sputtering". In: *PVD for Microelectronics.* Ed. by R. A. Powell and S. M. Rossnagel. Vol. 26. Thin Films. Elsevier, 1999, pp. 23–49. DOI: 10.1016/S1079-4050(99)80005-2.

[12] C. Sfiligoj. "Towards stable nanolayers for EUV optics". PhD thesis. University of Amsterdam, 2021. URL: https://hdl.handle.net/11245.1/eb38c693-37b4-483f-9e07-fec239c7c132.

[13] A. Baptista, F. Silva, J. Porteiro, J. Míguez, and G. Pinto. "Sputtering Physical Vapour Deposition (PVD) Coatings: A Critical Review on Process Improvement and Market Trend Demands". In: *Coatings* 8.11 (2018), p. 402. ISSN: 2079-6412. DOI: 10.3390/coatings8110402.

[14] K. A. Petroski and J. C. Sagás. "Alternative anode geometry for magnetron sputtering". In: *Vacuum* 182 (2020), p. 109703. ISSN: 0042-207X. DOI: 10.1016/j.vacuum.2020.109703.

[15] D. H. Lowndes, D. B. Geohegan, A. A. Puretzky, D. P. Norton, and C. M. Rouleau. "Synthesis of Novel Thin-Film Materials by Pulsed Laser Deposition". In: *Science* 273.5277 (1996), pp. 898–903. DOI: 10.1126/science.273.5277.898.

[16] H. M. Smith and A. F. Turner. "Vacuum Deposited Thin Films Using a Ruby Laser". In: *Appl. Opt.* 4.1 (1965), pp. 147–148. DOI: 10.1364/AO.4.000147.

[17] J. T. Cheung. "Epitaxial growth of $Hg_{0.7}Cd_{0.3}Te$ by laser-assisted deposition". In: *Applied Physics Letters* 43.3 (1983), pp. 255–257. ISSN: 0003-6951. DOI: 10.1063/1.94317.

[18] D. Dijkkamp, T. Venkatesan, X. D. Wu, S. A. Shaheen, N. Jisrawi, Y. H. Min-Lee, W. L. McLean, and M. Croft. "Preparation of Y-Ba-Cu oxide superconductor thin films using pulsed laser evaporation from high Tc bulk material". In: *Applied Physics Letters* 51.8 (1987), pp. 619–621. ISSN: 0003-6951. DOI: 10.1063/1.98366.

[19] H. Fujioka. "Pulsed Laser Deposition (PLD)". In: *Handbook of Crystal Growth.* Second Edition. North-Holland, 2015, pp. 365–397. ISBN: 978-0-444-63304-0. DOI: 10.1016/B978-0-444-63304-0.00008-1.

[20] O. Nur and M. Willander. "Conventional nanofabrication methods". In: *Low Temperature Chemical Nanofabrication.* William Andrew Publishing, 2020, pp. 49–86. ISBN: 978-0-12-813345-3. DOI: 10.1016/B978-0-12-813345-3.00003-4.

[21] N. A. Shepelin, Z. P. Tehrani, N. Ohannessian, C. W. Schneider, D. Pergolesi, and T. Lippert. "A practical guide to pulsed laser deposition". In: *Chem. Soc. Rev.* 52 (2023), pp. 2294–2321. DOI: 10.1039/D2CS00938B.

[22] P. R. Willmott and J. R. Huber. "Pulsed laser vaporization and deposition". In: *Rev. Mod. Phys.* 72 (2000), pp. 315–328. DOI: 10.1103/RevModPhys.72.315.

[23] R. K. Singh and J. Narayan. “Pulsed-laser evaporation technique for deposition of thin films: Physics and theoretical model”. In: *Phys. Rev. B* 41 (1990), pp. 8843–8859. DOI: 10.1103/PhysRevB.41.8843.

[24] I. Weaver and C. L. S. Lewis. “Polar distribution of ablated atomic material during the pulsed laser deposition of Cu in vacuum: Dependence on focused laser spot size and power density”. In: *Journal of Applied Physics* 79.9 (1996), pp. 7216–7222. ISSN: 0021-8979. DOI: 10.1063/1.361437.

[25] A. Ojeda-G-P, M. Döbeli, and T. Lippert. “Influence of Plume Properties on Thin Film Composition in Pulsed Laser Deposition”. In: *Advanced Materials Interfaces* 5.18 (2018), p. 1701062. DOI: 10.1002/admi.201701062.

[26] Z. Vakulov, D. Khakhulin, E. Zamburg, A. Mikhaylichenko, V. A. Smirnov, R. Tominov, V. S. Klimin, and O. A. Ageev. “Towards Scalable Large-Area Pulsed Laser Deposition”. In: *Materials* 14.17 (2021), p. 4854. ISSN: 1996-1944. DOI: 10.3390/ma14174854.

[27] “Advanced functional oxide thin films grown by pulsed-laser deposition”. In: *Applied Surface Science* 278 (2013), pp. 2–6. ISSN: 0169-4332. DOI: 10.1016/j.apsusc.2012.10.190.

[28] “Pulsed Laser Deposition of Thin Films”. In: *Handbook of Laser Technology and Applications*. Ed. by B. Subedi, V. S. Puli, I. W. Boyd, and D. B. Chrisey. Second Edition. CRC Press, 2021, pp. 111–124. ISBN: 978-1-315-31085-5. DOI: 10.1201/9781315310855.

[29] H.-U. Krebs. “Pulsed Laser Deposition of Metals”. In: *Pulsed Laser Deposition of Thin Films*. John Wiley & Sons, Ltd, 2006, pp. 363–382. ISBN: 9780470052129. DOI: 10.1002/9780470052129.ch16.

[30] H.-U. Krebs, O. Bremert, Y. Luo, S. Fähler, and M. Störmer. “Structure of laser-deposited metallic alloys and multilayers”. In: *Thin Solid Films* 275.1 (1996), pp. 18–21. ISSN: 0040-6090. DOI: 10.1016/0040-6090(95)07010-9.

[31] M. Störmer, K. Sturm, S. Fähler, M. Weisheit, J. Winkler, S. Kahl, P. Kesten, A. Pundt, M. Seibt, S. Senz, and H.-U. Krebs. “Study of laser-deposited metallic thin films by a combination of high-resolution ex situ and time-resolved in situ experiments”. In: *Applied Physics A* 69 (1999), S455–S457. ISSN: 1432-0630. DOI: 10.1007/s003390051437.

[32] S. Fähler, S. Kahl, M. Weisheit, K. Sturm, and H. Krebs. “The interface of laser deposited Cu/Ag multilayers: evidence of the ‘subsurface growth mode’ during pulsed laser deposition”. In: *Applied Surface Science* 154-155 (2000), pp. 419–423. ISSN: 0169-4332. DOI: 10.1016/S0169-4332(99)00471-7.

[33] S. Sundar Manoharan, M. Klaua, J. Shen, J. Barthel, H. Jenniches, and J. Kirschner. “Artificially ordered Fe-Cu alloy superlattices on Cu(001). I. Studies on the structural and magnetic properties”. In: *Phys. Rev. B* 58 (1998), pp. 8549–8555. DOI: 10.1103/PhysRevB.58.8549.

[34] S. Fähler, K. Sturm, and H.-U. Krebs. “Resputtering during the growth of pulsed-laser-deposited metallic films in vacuum and in an ambient gas”. In: *Applied Physics Letters* 75.24 (1999), pp. 3766–3768. ISSN: 0003-6951. DOI: 10.1063/1.125449.

[35] T. Scharf, J. Faupel, K. Sturm, and H.-U. Krebs. “Pulsed laser deposition of metals in various inert gas atmospheres”. In: *Applied Physics A* 79 (2004), pp. 1587–1589. ISSN: 1432-0630. DOI: 10.1007/s00339-004-2855-z.

[36] A. Troglia, V. Vollema, S. Cassanelli, E. van Heumen, J. van de Groep, A. de Visser, and R. Bliem. “Tuning material properties via disorder: From crystalline alloy to metallic glass”. In: *Materials Today Physics* 29 (2022), p. 100893. ISSN: 2542-5293. DOI: 10.1016/j.mtphys.2022.100893.

[37] K. Sturm and H.-U. Krebs. “Quantification of resputtering during pulsed laser deposition”. In: *Journal of Applied Physics* 90.2 (2001), pp. 1061–1063. ISSN: 0021-8979. DOI: 10.1063/1.1379050.

[38] W.-K. Lee, H.-Y. Wong, K.-Y. Chan, T.-K. Yong, S.-S. Yap, and T.-Y. Tou. “Effects of laser fluence on the structural properties of pulsed laser deposited ruthenium thin films”. In: *Applied Physics A* 100 (2010), pp. 561–568. ISSN: 1432-0630. DOI: 10.1007/s00339-010-5875-x.

[39] L. Doeswijk, G. Rijnders, and D. Blank. “Pulsed laser deposition: metal versus oxide ablation”. In: *Applied Physics A* 78 (2004), pp. 263–268. ISSN: 1432-0630. DOI: 10.1007/s00339-003-2332-0.

[40] W.-O. Siew, W.-K. Lee, H.-Y. Wong, T.-K. Yong, S.-S. Yap, and T.-Y. Tou. “Investigation of droplet formation in pulsed Nd:YAG laser deposition of metals and silicon”. In: *Applied Physics A* 101 (2010), pp. 627–632. ISSN: 1432-0630. DOI: 10.1007/s00339-010-5914-7.

[41] J. Fishburn, M. Withford, D. Coutts, and J. Piper. “Study of the fluence dependent interplay between laser induced material removal mechanisms in metals: Vaporization, melt displacement and melt ejection”. In: *Applied Surface Science* 252.14 (2006), pp. 5182–5188. ISSN: 0169-4332. DOI: https://doi.org/10.1016/j.apsusc.2005.07.053.

[42] S. Fähler, M. Störmer, and H. Krebs. “Origin and avoidance of droplets during laser ablation of metals”. In: *Applied Surface Science* 109-110 (1997), pp. 433–436. ISSN: 0169-4332. DOI: 10.1016/S0169-4332(96)00782-9.

[43] A. Gorbunov, W. Pompe, A. Sewing, S. Gaponov, A. Akhsakhalyan, I. Zabrodin, I. Kas’kov, E. Klyenkov, A. Morozov, N. Salaschenko, R. Dietsch, H. Mai, and S. Völlmar. “Ultrathin film deposition by pulsed laser ablation using crossed beams”. In: *Applied Surface Science* 96-98 (1996), pp. 649–655. ISSN: 0169-4332. DOI: 10.1016/0169-4332(95)00537-4.

[44] T. Szörényi, Z. Kántor, Z. Tóth, and P. Heszler. “Pulsed laser deposition from solid and molten metals”. In: *Applied Surface Science* 138-139 (1999), pp. 275–279. ISSN: 0169-4332. DOI: 10.1016/S0169-4332(98)00407-3.

[45] Y. Xu, L. Jeurgens, L. Lin, S. Ma, S. Zhu, Y. Huang, Y. Liu, J. Qiao, and Z. Wang. "Revealing the univariate effect of structural order on the oxidation of ternary alloys: Amorphous vs. crystalline Cu–Zr–Al alloys". In: *Corrosion Science* 183 (2021), p. 109309. ISSN: 0010-938X. DOI: 10.1016/j.corsci.2021.109309.

[46] K. R. Lim, J. M. Park, S. J. Kim, E.-S. Lee, W. T. Kim, A. Gebert, J. Eckert, and D. H. Kim. "Enhancement of oxidation resistance of the supercooled liquid in Cu–Zr-based metallic glass by forming an amorphous oxide layer with high thermal stability". In: *Corrosion Science* 66 (2013), pp. 1–4. ISSN: 0010-938X. DOI: 10.1016/j.corsci.2012.09.018.

[47] R. C. Munoz and C. Arenas. "Size effects and charge transport in metals: Quantum theory of the resistivity of nanometric metallic structures arising from electron scattering by grain boundaries and by rough surfaces". In: *Applied Physics Reviews* 4 (2017), p. 011102. DOI: 10.1063/1.4974032.

[48] J. P. Chu, J. Jang, J. Huang, H. Chou, Y. Yang, J. Ye, Y. Wang, J. Lee, F. Liu, P. Liaw, Y. Chen, C. Lee, C. Li, and C. Rullyani. "Thin film metallic glasses: Unique properties and potential applications". In: *Thin Solid Films* 520 (2012), pp. 5097–5122. ISSN: 0040-6090. DOI: 10.1016/j.tsf.2012.03.092.

[49] J. A. Venables, G. D. T. Spiller, and M. Hanbucken. "Nucleation and growth of thin films". In: *Reports on Progress in Physics* 47.4 (1984), p. 399. DOI: 10.1088/0034-4885/47/4/002.

[50] N. Kaiser. "Review of the fundamentals of thin-film growth". In: *Appl. Opt.* 41.16 (2002), pp. 3053–3060. DOI: 10.1364/AO.41.003053.

[51] G. Gilmer, H. Huang, and C. Roland. "Thin film deposition: fundamentals and modeling". In: *Computational Materials Science* 12.4 (1998), pp. 354–380. ISSN: 0927-0256. DOI: 10.1016/S0927-0256(98)00022-6.

[52] P. Willmott. "Deposition of complex multielemental thin films". In: *Progress in Surface Science* 76.6 (2004), pp. 163–217. ISSN: 0079-6816. DOI: 10.1016/j.progsurf.2004.06.001.

[53] G. Rijnders and D. H. A. Blank. "Growth Kinetics During Pulsed Laser Deposition". In: *Pulsed Laser Deposition of Thin Films*. John Wiley & Sons, Ltd, 2006, pp. 177–190. ISBN: 9780470052129. DOI: 10.1002/9780470052129.ch8.

[54] R. W. Vook. "Structure and growth of thin films". In: *International Metals Reviews* 27.1 (1982), pp. 209–245. DOI: 10.1179/imr.1982.27.1.209.

[55] K. Oura, M. Katayama, A. V. Zotov, V. G. Lifshits, and A. A. Saranin. "Growth of Thin Films". In: *Surface Science: An Introduction*. Springer Berlin Heidelberg, 2003, pp. 357–387. ISBN: 978-3-662-05179-5. DOI: 10.1007/978-3-662-05179-5_14.

[56] I. Petrov, P. B. Barna, L. Hultman, and J. E. Greene. "Microstructural evolution during film growth". In: *Journal of Vacuum Science & Technology A* 21.5 (2003), S117–S128. ISSN: 0734-2101. DOI: 10.1116/1.1601610.

[57] Z. Zhang and M. G. Lagally. “Atomistic Processes in the Early Stages of Thin-Film Growth”. In: *Science* 276.5311 (1997), pp. 377–383. DOI: 10.1126/science.276.5311.377.

[58] J. Kollár, L. Vitos, B. Johansson, and H. Skriver. “Metal Surfaces: Surface, Step and Kink Formation Energies”. In: *physica status solidi (b)* 217.1 (2000), pp. 405–418. DOI: 10.1002/(SICI)1521-3951(200001)217:1<405::AID-PSSB405>3.0.CO;2-6.

[59] W. K. Burton, N. Cabrera, F. C. Frank, and N. F. Mott. “The growth of crystals and the equilibrium structure of their surfaces”. In: *Philosophical Transactions of the Royal Society of London. Series A, Mathematical and Physical Sciences* 243.866 (1951), pp. 299–358. DOI: 10.1098/rsta.1951.0006.

[60] S. J. Lombardo and A. T. Bell. “A review of theoretical models of adsorption, diffusion, desorption, and reaction of gases on metal surfaces”. In: *Surface Science Reports* 13.1 (1991), pp. 3–72. ISSN: 0167-5729. DOI: 10.1016/0167-5729(91)90004-H.

[61] Y. W. Mo, J. Kleiner, M. B. Webb, and M. G. Lagally. “Activation energy for surface diffusion of Si on Si(001): A scanning-tunneling-microscopy study”. In: *Phys. Rev. Lett.* 66 (1991), pp. 1998–2001. DOI: 10.1103/PhysRevLett.66.1998.

[62] A. Pimpinelli, J. Villain, and D. E. Wolf. “Surface diffusion and island density”. In: *Phys. Rev. Lett.* 69 (1992), pp. 985–985. DOI: 10.1103/PhysRevLett.69.985.

[63] B. S. Swartzentruber. “Direct Measurement of Surface Diffusion Using Atom-Tracking Scanning Tunneling Microscopy”. In: *Phys. Rev. Lett.* 76 (1996), pp. 459–462. DOI: 10.1103/PhysRevLett.76.459.

[64] C. Ratsch and J. A. Venables. “Nucleation theory and the early stages of thin film growth”. In: *Journal of Vacuum Science & Technology A* 21.5 (2003), S96–S109. ISSN: 0734-2101. DOI: 10.1116/1.1600454.

[65] J.-K. Zuo, J. F. Wendelken, H. Dürr, and C.-L. Liu. “Growth and coalescence in submonolayer homoepitaxy on Cu(100) studied with high-resolution low-energy electron diffraction”. In: *Phys. Rev. Lett.* 72 (1994), pp. 3064–3067. DOI: 10.1103/PhysRevLett.72.3064.

[66] J. A. Stroscio and D. T. Pierce. “Scaling of diffusion-mediated island growth in iron-on-iron homoepitaxy”. In: *Phys. Rev. B* 49 (1994), pp. 8522–8525. DOI: 10.1103/PhysRevB.49.8522.

[67] P. A. Thiel and J. W. Evans. “Nucleation, Growth, and Relaxation of Thin Films: Metal(100) Homoepitaxial Systems”. In: *The Journal of Physical Chemistry B* 104.8 (2000), pp. 1663–1676. DOI: 10.1021/jp9933471.

[68] H. Röder, E. Hahn, H. Brune, J.-P. Bucher, and K. Kern. “Building one- and two-dimensional nanostructures by diffusion-controlled aggregation at surfaces”. In: *Nature* 366 (1993), pp. 141–143. ISSN: 1476-4687. DOI: 10.1038/366141a0.

[69] J.-M. Wen, S.-L. Chang, J. W. Burnett, J. W. Evans, and P. A. Thiel. “Diffusion of Large Two-Dimensional Ag Clusters on Ag(100)”. In: *Phys. Rev. Lett.* 73 (1994), pp. 2591–2594. DOI: 10.1103/PhysRevLett.73.2591.

[70] G. Ehrlich and F. G. Hudda. “Atomic View of Surface Self-Diffusion: Tungsten on Tungsten”. In: *The Journal of Chemical Physics* 44.3 (1966), pp. 1039–1049. ISSN: 0021-9606. DOI: 10.1063/1.1726787.

[71] K. Bromann, H. Brune, H. Röder, and K. Kern. “Interlayer Mass Transport in Homoepitaxial and Heteroepitaxial Metal Growth”. In: *Phys. Rev. Lett.* 75 (1995), pp. 677–680. DOI: 10.1103/PhysRevLett.75.677.

[72] S. Harris. “Kinetics of interlayer transport prior to nucleation”. In: *Phys. Rev. B* 52 (1995), pp. 16793–16795. DOI: 10.1103/PhysRevB.52.16793.

[73] J. A. Meyer, J. Vrijmoeth, H. A. van der Vegt, E. Vlieg, and R. J. Behm. “Importance of the additional step-edge barrier in determining film morphology during epitaxial growth”. In: *Phys. Rev. B* 51 (1995), pp. 14790–14793. DOI: 10.1103/PhysRevB.51.14790.

[74] R. Kunkel, B. Poelsema, L. K. Verheij, and G. Comsa. “Reentrant layer-by-layer growth during molecular-beam epitaxy of metal-on-metal substrates”. In: *Phys. Rev. Lett.* 65 (1990), pp. 733–736. DOI: 10.1103/PhysRevLett.65.733.

[75] R. Messier. “Toward quantification of thin film morphology”. In: *Journal of Vacuum Science & Technology A* 4.3 (1986), pp. 490–495. ISSN: 0734-2101. DOI: 10.1116/1.573866.

[76] S. N. Naik and S. M. Walley. “The Hall–Petch and inverse Hall–Petch relations and the hardness of nanocrystalline metals”. In: *Journal of Materials Science* 55 (2020), pp. 2661–2681. ISSN: 1573-4803. DOI: 10.1007/s10853-019-04160-w.

[77] N. Schäfer, D. Günzing, T. Jiang, N. Karabas, A. Arzumanov, D. Motta-Meira, K. Ollefs, P. Komissinskiy, M. Major, M. Arnold, N. Pietralla, H. Wende, L. Molina-Luna, D. Lützenkirchen-Hecht, and L. Alff. “Role of kinetic energy on Nb_3Sn thin films by low-temperature co-sputtering”. In: *Journal of Applied Physics* 134.4 (2023), p. 043903. ISSN: 0021-8979. DOI: 10.1063/5.0145181.

[78] H. Guo, X. Wang, A. D. Dupuy, J. M. Schoenung, and W. J. Bowman. “Growth of nanoporous high-entropy oxide thin films by pulsed laser deposition”. In: *Journal of Materials Research* 37 (2022), pp. 124–135. ISSN: 1573-4803. DOI: 10.1557/s43578-021-00473-2.

[79] E. Chason and P. R. Guduru. “Tutorial: Understanding residual stress in polycrystalline thin films through real-time measurements and physical models”. In: *Journal of Applied Physics* 119.19 (2016), p. 191101. DOI: 10.1063/1.4949263.

[80] G. Abadias, E. Chason, J. Keckes, M. Sebastiani, G. B. Thompson, E. Barthel, G. L. Doll, C. E. Murray, C. H. Stoessel, and L. Martinu. “Review Article: Stress in thin films and coatings: Current status, challenges, and prospects”. In: *Journal of Vacuum Science & Technology A* 36.2 (2018), p. 020801. ISSN: 0734-2101. DOI: 10.1116/1.5011790.

[81] I. Mizushima, P. T. Tang, H. N. Hansen, and M. A. Somers. “Residual stress in Ni–W electrodeposits”. In: *Electrochimica Acta* 51.27 (2006). ChargeTransfer at Electrochemical Interfaces "Two Hundred Years of Electrlysis", pp. 6128–6134. ISSN: 0013-4686. DOI: 10.1016/j.electacta.2005.11.053.

[82] M.-W. Moon, J.-W. Chung, K.-R. Lee, K. Oh, R. Wang, and A. Evans. “An experimental study of the influence of imperfections on the buckling of compressed thin films”. In: *Acta Materialia* 50.5 (2002), pp. 1219–1227. ISSN: 1359-6454. DOI: 10.1016/S1359-6454(01)00423-2.

[83] J. Wang and A. Evans. “Effects of strain cycling on buckling, cracking and spalling of a thermally grown alumina on a nickel-based bond coat”. In: *Acta Materialia* 47.2 (1999), pp. 699–710. ISSN: 1359-6454. DOI: 10.1016/S1359-6454(98)00328-0.

[84] P. Gudmundson and A. Wikström. “Stresses in thin films and interconnect lines”. In: *Microelectronic Engineering* 60.1 (2002), pp. 17–29. ISSN: 0167-9317. DOI: 10.1016/S0167-9317(01)00577-9.

[85] M. Huff. “Review Paper: Residual Stresses in Deposited Thin-Film Material Layers for Micro- and Nano-Systems Manufacturing”. In: *Micromachines* 13.12 (2022), p. 2084. ISSN: 2072-666X. DOI: 10.3390/mi13122084.

[86] A. R. Shugurov and A. V. Panin. “Mechanisms of Stress Generation in Thin Films and Coatings”. In: *Technical Physics* 65 (2020), pp. 1881–1904. ISSN: 0167-9317. DOI: 10.1134/S1063784220120257.

[87] H. V. Thang, S. Tosoni, and G. Pacchioni. “The epitaxial growth of ZnO films on Cu(111) surface: Thickness dependence”. In: *Applied Surface Science* 483 (2019), pp. 133–139. ISSN: 0169-4332. DOI: 10.1016/j.apsusc.2019.03.240.

[88] Y. Pang and R. Huang. “Nonlinear effect of stress and wetting on surface evolution of epitaxial thin films”. In: *Phys. Rev. B* 74 (2006), p. 075413. DOI: 10.1103/PhysRevB.74.075413.

[89] D. J. Eaglesham and M. Cerullo. “Dislocation-free Stranski-Krastanow growth of Ge on Si(100)”. In: *Phys. Rev. Lett.* 64 (1990), pp. 1943–1946. DOI: 10.1103/PhysRevLett.64.1943.

[90] F. Spaepen. “Interfaces and stresses in thin films”. In: *Acta Materialia* 48.1 (2000), pp. 31–42. ISSN: 1359-6454. DOI: 10.1016/S1359-6454(99)00286-4.

[91] J. W. Cahn. “Surface stress and the chemical equilibrium of small crystals—I. the case of the isotropic surface”. In: *Acta Metallurgica* 28.10 (1980), pp. 1333–1338. ISSN: 0001-6160. DOI: 10.1016/0001-6160(80)90002-4.

[92] R. C. Cammarata. “Surface and interface stress effects in thin films”. In: *Progress in Surface Science* 46.1 (1994), pp. 1–38. ISSN: 0079-6816. DOI: 10.1016/0079-6816(94)90005-1.

[93] A. L. Shull and F. Spaepen. “Measurements of stress during vapor deposition of copper and silver thin films and multilayers”. In: *Journal of Applied Physics* 80.11 (1996), pp. 6243–6256. ISSN: 0021-8979. DOI: 10.1063/1.363701.

[94] R. C. Cammarata, T. M. Trimble, and D. J. Srolovitz. “Surface stress model for intrinsic stresses in thin films”. In: *Journal of Materials Research* 15 (2000), pp. 2468–2474. ISSN: 2044-5326. DOI: 10.1557/JMR.2000.0354.

[95] C. Friesen and C. V. Thompson. “Reversible Stress Relaxation during Precoalescence Interruptions of Volmer-Weber Thin Film Growth”. In: *Phys. Rev. Lett.* 89 (2002), p. 126103. DOI: 10.1103/PhysRevLett.89.126103.

[96] W. D. Nix and B. M. Clemens. “Crystallite coalescence: A mechanism for intrinsic tensile stresses in thin films”. In: *Journal of Materials Research* 14 (1999), pp. 3467–3473. ISSN: 2044-5326. DOI: 10.1557/JMR.1999.0468.

[97] H. Z. Yu and C. V. Thompson. “Grain growth and complex stress evolution during Volmer–Weber growth of polycrystalline thin films”. In: *Acta Materialia* 67 (2014), pp. 189–198. ISSN: 1359-6454. DOI: 10.1016/j.actamat.2013.12.031.

[98] R. Koch. “The intrinsic stress of polycrystalline and epitaxial thin metal films”. In: *Journal of Physics: Condensed Matter* 6 (1994), p. 9519. DOI: 10.1088/0953-8984/6/45/005.

[99] E. Chason. “A kinetic analysis of residual stress evolution in polycrystalline thin films”. In: *Thin Solid Films* 526 (2012), pp. 1–14. ISSN: 0040-6090. DOI: 10.1016/j.tsf.2012.11.001.

[100] J. W. Shin and E. Chason. “Compressive Stress Generation in Sn Thin Films and the Role of Grain Boundary Diffusion”. In: *Phys. Rev. Lett.* 103 (2009), p. 056102. DOI: 10.1103/PhysRevLett.103.056102.

[101] H. Z. Yu and C. V. Thompson. “Correlation of shape changes of grain surfaces and reversible stress evolution during interruptions of polycrystalline film growth”. In: *Applied Physics Letters* 104.14 (2014), p. 141913. ISSN: 0003-6951. DOI: 10.1063/1.4871214.

[102] C. V. Thompson and R. Carel. “Stress and grain growth in thin films”. In: *Journal of the Mechanics and Physics of Solids* 44.5 (1996). Mechanics and Physics of Layered and Graded Materials, pp. 657–673. ISSN: 0022-5096. DOI: 10.1016/0022-5096(96)00022-1.

[103] M. Murakami. “Deformation in thin films by thermal strain”. In: *Journal of Vacuum Science & Technology A* 9.4 (1991), pp. 2469–2476. ISSN: 0734-2101. DOI: 10.1116/1.577258.

[104] A. Troglia, S. van Vliet, G. Yetik, I. E. Wakil, J. Momand, B. J. Kooi, and R. Bliem. “Free-standing nanolayers based on Ru silicide formation on Si(100)”. In: *Phys. Rev. Mater.* 6 (2022), p. 043402. DOI: 10.1103/PhysRevMaterials.6.043402.

[105] T.-A. Truong, T.-K. Nguyen, H. Zhao, N.-K. Nguyen, T. Dinh, Y. Park, T. Nguyen, Y. Yamauchi, N.-T. Nguyen, and H.-P. Phan. “Engineering Stress in Thin Films: An Innovative Pathway Toward 3D Micro and Nanosystems”. In: *Small* 18.4 (2022), p. 2105748. DOI: 10.1002/smll.202105748.

[106] O. Thomas, P. Gergaud, C. Rivero, and F. M. d’Heurle. “Stress Development during the Reactive Formation of Silicide Films”. In: *Diffusion in Materials - DIMAT2004*. Vol. 237. Trans Tech Publications Ltd, 2005, pp. 801–812. DOI: 10.4028/www.scientific.net/DDF.237-240.801.

2

FREE-STANDING NANOLAYERS BASED ON RU SILICIDE FORMATION ON SI(100)

Free-standing layers of nanoscale thickness are essential in numerous applications but challenging to fabricate for all but a small selection of materials. We report a versatile, chemical-free pathway of exfoliating centimeter-sized free-standing nanolayers from Si(100) with native oxide based on the spontaneous delamination of thin Ru and Ru-based films upon annealing at temperatures as low as 400° C. Combining results from x-ray photoelectron spectroscopy (XPS), and transmission and scanning electron microscopy (TEM, SEM), we identify that the element Ru, a thin SiO_2 layer, and the Si(100) substrate are essential ingredients for the delamination and propose a stress-based mechanism to explain the effect. The diffusion of Si into the layer upon annealing leads to the formation of a Ru-Si compound at the thin-film side of the Ru/Si(100) interface and pyramidal cavities in the Si(100) substrate. Moreover, the uptake of Si results in an increase in layer thickness and the buildup of in-plane compressive stress, which is reduced by local buckling and finally by the separation of the full layer from the substrate at the SiO_2-Si(100) interface. The use of a thin Ru-buffer layer allows us to apply this delamination process to produce free-standing nanolayers of Mo and HfMoNbTiZr in this simple, chemical-free, and vacuum-compatible manner. These results indicate the potential of the reported effect for the fabrication of free-standing layers using a wide range of compositions, deposition techniques, and growth conditions below the onset temperature of delamination.

A. Troglia, S. van Vliet, G. Yetik, I. El Wakil, J. Momand, B. J. Kooi, and R. Bliem. *Free-standing nanolayers based on Ru silicide formation on Si(100).* Physical Review Materials **6**, 043402 (2022).

2.1 INTRODUCTION

Thin free-standing membranes are indispensable in technological applications such as frequency filters [1–3], advanced electronics [4, 5], gas-separation membranes [6, 7], or transparent sheets for short-wavelength radiation [8–11]. They also find application in catalysis [12, 13], as electrodes in advanced battery concepts [14–16], and as interconnects [17]. Each of these applications has its own, demanding set of requirements to the respective free-standing films. Customized materials are thus required for good functionality. Manufacturing customized layers in a reproducible way is challenging and often requires complex processing and the intensive use of chemicals, for example for the chemical removal of the entire substrate after depositing the thin films. New, chemical-free ways of producing free-standing films would contribute to developing simpler and more sustainable production methods with a better environmental footprint and potentially a lower price.

The production of free-standing layers typically starts with the deposition of a thin film on the substrate of choice. Thin-film growth is typically accompanied by the buildup of stress, which finds its origin in intrinsic and extrinsic sources [18, 19]. Intrinsic stress is attributed to the formation of defects in the layer during grain growth and to the coalescence of grains. It increases with film thickness and is specific to the combination of deposited material, substrate, and growth conditions [18]. Extrinsic stress components, on the other hand, are not directly related to the atomic-scale structure of a film, but originate for example in the difference in thermal expansion coefficients between the substrate and a film deposited at elevated temperature [19, 20]. The superposition of these stress components compromises the adhesion of the film to the substrate and can lead to failure in the form of cracking or uncontrolled delamination if a critical stress value is exceeded.

The stress in a layer of a defined phase and composition varies substantially if its density and structure are modified by processes such as diffusion, intercalation [21], phase transformations [19], and compound formation [22, 23]. The formation of silicides by annealing thin films of transition metals deposited onto Si is a good example of this process [24]. The formation of a silicide by Si diffusion typically leads to compressive stress in the layer due to the addition of material, which usually requires a volume expansion to match the different density of the compound formed. Various relaxation mechanisms may lead to a reduction of the total stress in the film [25].

In this article we report the observation that Ru-based metal films on native-oxide-terminated Si(100) substrates delaminate spontaneously at the Si(100)-SiO_2 interface upon annealing at approximately 400 °C, yielding centimeter-scale free-standing layers with thicknesses starting at 20 nm. We further observed that a Ru silicide phase was formed by Si diffusion through the native SiO_2 layer during annealing. The uptake of Si substantially increased the equilibrium volume of the film, adding a strong compressive component to the stress in the layer and at the interface. We propose that this buildup of compressive stress is at the root of the delamination and causes the Ru-Si/SiO_2/Si(100) stack to cleave at the Si-SiO_2

interface. This mechanism reconciles our observations on thin films of various thicknesses and compositions, grown using two different techniques. Moreover, we demonstrate that Mo and HfMoNbTiZr films on Si(100) with an ultrathin Ru silicide buffer layer follow the same delamination pattern, indicating a potential application of the reported Ru-based delamination for the chemical-free exfoliation of customized free-standing metal layers via a versatile, vacuum-compatible, and environmentally friendly process.

2.2 METHODS

2.2.1 SAMPLE PREPARATION

Pure Ru, Mo, and $Ru_{100-x}Mo_x$ alloy thin films were sputter-deposited onto p-doped Si(100) substrates with native oxide using a Polyteknik Flextura M506 S system. The substrates were cleaned with a sequential ultrasonic bath of acetone and isopropanol; the native oxide of Si was not removed prior to deposition. The base pressure of the system was approximately 1.0×10^{-7} mbar. Pure Ru and Mo thin films were deposited by DC sputtering with a power of 200 and 75 W and Ar background pressure of 2.0×10^{-3} and 1.33×10^{-2} mbar, respectively. $Ru_{100-x}Mo_x$ alloy thin films were co-deposited from separate sources by RF and DC sputtering, respectively, with an argon background pressure of 2.0×10^{-3} mbar. During deposition, the substrates were kept at room temperature and rotated in order to optimize the homogeneity of the deposition. The Ru silicide reference sample was synthesized by depositing a 25 nm thick Ru thin film onto clean Si(100) substrates with native oxide by pulsed laser deposition using a KrF excimer laser at an energy density of 7.5 J/cm^2 and laser repetition rate of 10 Hz. A 99.95 % pure Ru target (Alineason Materials Technology GmbH) was used for the deposition process. The substrate was kept at room temperature and the background deposition pressure was 1.0×10^{-9} mbar. The Ru thin film was subsequently annealed at 550°C to ensure homogeneous conversion of the entire film to Ru silicide [26]. HfMoNbTiZr thin films were deposited with pulsed laser deposition in 4.0×10^{-2} mbar Ar background pressure at an energy density of 11.0 J/cm^2 and a laser repetition rate of 10 Hz. A custom-made HfMoNbTiZr (20:20:20:20:20 at.%) target was used for the deposition process.

2.2.2 X-RAY PHOTOELECTRON SPECTROSCOPY

The step-by-step XPS investigation of the delamination process was performed *in situ* in a UHV setup (base pressure better than 1.0×10^{-9} mbar) equipped with a Scienta Omicron R4000 HiPP-3 analyzer (swift acceleration mode, 1 mm slit entrance) and a monochromatic Al-Kα source (1486.6 eV). An as-grown Ru thin film (thickness approximately 100 nm) was loaded in the setup via a load lock: the annealing treatment was performed in UHV at approximately 400°C with a radiative heater; the temperature was measured both with a thermocouple and a pyrometer. The delamination of the Ru thin film was performed directly in UHV

with carbon tape, allowing the XPS measurement of the film-substrate interface side of the delaminated layer and bare substrate separately, avoiding any surface contamination due to air exposure. Survey spectra were recorded at 500 eV of pass energy (PE), while detailed spectra were recorded at PE=100 eV.

2.2.3 SCANNING ELECTRON MICROSCOPY

SEM measurements were performed using a FEI Verios 460 SEM system with a Schottky field electron gun. The SEM micrographs were taken at an electron energy of 5 keV and a beam current of 100 pA. The immersion field mode was used in order to optimize the spatial resolution.

2.2.4 TRANSMISSION ELECTRON MICROSCOPY

Cross sectional specimens of the $Ru_{47}Mo_{53}$ thin film were prepared with an FEI Helios G4 CX dual beam system at 30 kV ion energy and polished at 5 and 2 keV to remove residual surface damage. These specimens were analyzed with a double-aberration-corrected FEI Themis Z scanning transmission electron microscopy system at 300 kV. EDX spectrum mapping was performed with a probe current of 1 nA, where the spectra were recorded with a Dual-X system, providing in total 1.76 sr EDX detector.

2.3 RESULTS AND DISCUSSION

Figure 2.1 depicts a schematic of the observed delamination of Ru thin films upon annealing. After sputter deposition of Ru on native-oxide terminated Si(100), as described in the Methods section, the 20 to 200 nm thick Ru films were found to detach completely from the substrate upon annealing at 400°C. This delamination was characterized by visible changes in the appearance of the films. The film surface developed visible patches of lower reflectivity and higher apparent roughness. These modified areas expanded, propagating across the sample on a timescale of several seconds and finally leading to a changed appearance of the entire film (see video link in the Appendix [27]). What seemed to be a roughening transition was concomitant with a loss of adhesion between the substrate and the entire Ru layer. The resulting free-standing nanolayers were harvested from the substrate using adhesive tape. For thicknesses of 100 nm and higher, centimeter-sized flakes were directly exfoliated with tweezers, as shown in Figure 2.1 (c).

The composition and chemical properties of the exposed Si(100) substrate and the thin-film side of the Ru/Si(100) interface were investigated *in situ* after delamination of a 100 nm thick Ru film in ultrahigh vacuum (UHV) by means of x-ray photoelectron spectroscopy (XPS). The survey spectrum of the 100 nm thick Ru film (Figure 2.5 [27]) shows only peaks corresponding to Ru and oxygen, which was present due to exposure to air before annealing, whereas Ru, O, and Si were observed at the thin-film side of the interface (Figure 2.6 [27]). Figure 2.2 (a) shows

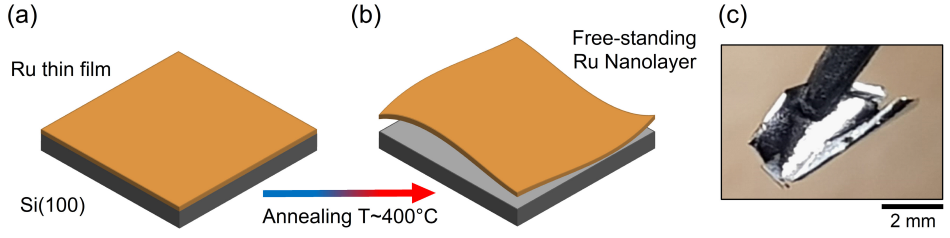

Figure 2.1 *Sketch of the delamination process. (a) Ru-based thin films (thickness ranging from approximately 20 nm up to 200 nm) are sputter-deposited onto clean Si(100) substrates with native oxide. (b) Annealing at T≈400°C causes the delamination of the film from the substrate. (c) Centimeter-sized free-standing layer (200 nm $Ru_{77}Mo_{23}$) exfoliated from the substrate with tweezers.*

the XPS spectra of the extended Ru 3d region of the as-grown Ru thin film before annealing (black), the thin-film side of the Ru/Si(100) interface after annealing and delamination in UHV (red), and a separately prepared, thin Ru silicide film that was used as a reference specimen (blue). The spectrum of the as-grown Ru thin film is characterized by the Ru $3d_{5/2}$ peak at a binding energy of 279.9 eV, a doublet peak splitting of 4.1 eV, and an asymmetric peak shape, in good agreement with reports for metallic Ru in the literature [28]. Moreover, the extended Ru 3d region in Figure 2.2 (a) shows the presence of a broad plasmon loss feature at a binding energy value of approximately 312 eV, corresponding to an electron energy difference of ΔE≈32 eV with respect to the main Ru $3d_{5/2}$ peak.

In the XPS spectra of the thin-film side of the exfoliated Ru/Si(100) interface (red), the main Ru $3d_{5/2}$ peak of the spectrum is shifted by 0.45 eV towards lower binding energy with respect to metallic Ru, comparable to the binding energy shift attributed to the formation of a metal-rich Ru silicide in the literature [29]. The extended Ru 3d region in Figure 2.2 (a) shows a plasmon loss peak at approximately 305 eV (ΔE≈25.5 eV), which is close to its position in the Ru silicide reference sample at 303 eV (blue). Moreover, the peak shape of the Ru 3d doublet of the thin-film side of the Ru/Si(100) interface spectrum in Figure 2.2 (b) shows a sharp contrast to the asymmetric shape that is characteristic of metallic Ru (black) [28], and resembles the symmetric peak shapes of the Ru silicide Ru 3d doublet (blue). The increased width and shifted binding energy of the plasmon loss peak at the thin-film side of the Ru/Si(100) interface compared to the silicide reference as well as the small residual asymmetry of the Ru 3d peaks indicate the presence of a small amount of metallic Ru close to the interface. This comparison indicates a change in electronic structure with the annealing treatment and suggests the formation of a nonmetallic Ru silicide at the interface between the Ru thin film and the substrate. A detailed XPS investigation to discern the type of silicide that is formed is beyond the scope of this study.

A survey spectrum of the thin-film side of the Ru/Si(100) interface reveals the presence of silicon and oxygen (see Appendix Figure 2.6 (a) [27]). From the

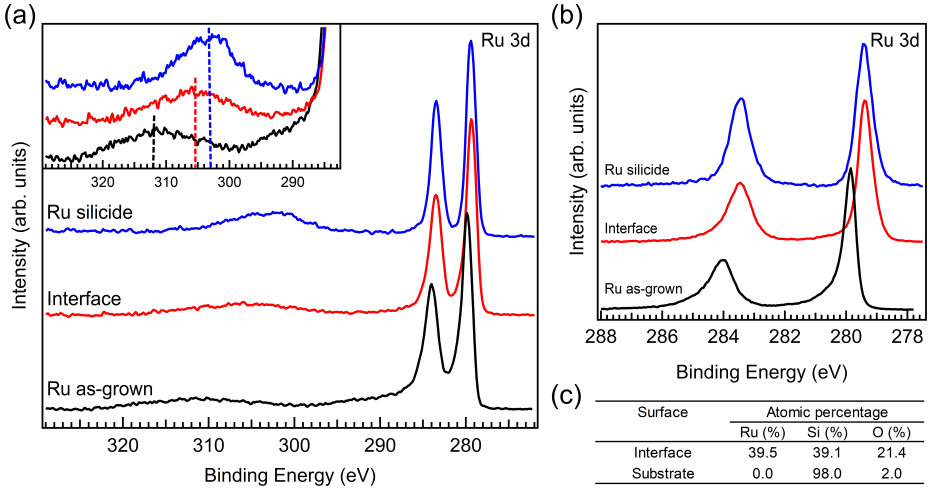

Surface	Atomic percentage		
	Ru (%)	Si (%)	O (%)
Interface	39.5	39.1	21.4
Substrate	0.0	98.0	2.0

Figure 2.2 *XPS results of the Ru layer before and after delamination. (a) Extended Ru 3d region of the as-grown Ru thin film (black), the thin-film side of the Ru/Si(100) interface after annealing and tape delamination in UHV (red), and a Ru silicide thin-film reference (blue). The shift of the plasmon loss peak maximum is highlighted in the inset with dashed lines. (b) Ru 3d detailed spectra of the as-grown Ru thin film (black), thin-film side of the Ru/Si(100) interface (red), and Ru silicide reference (blue). (c) Surface compositions of the thin-film side of the Ru/Si(100) interface and the Si(100) substrate after annealing and exfoliation in UHV.*

measured XPS peak area we estimated the relative composition of Ru, Si, and O in the surface region to be 39.5%, 39.1%, and 21.4%, respectively, as reported in Figure 2.2 (c). Variations in probing depth with different electron kinetic energies were not taken into account. The detailed spectrum of the Si 2p region [Figure 2.6 (b)] shows a small shift of the main Si $2p_{3/2}$ peak of 0.3 eV towards a higher binding energy value compared to elemental Si, which is in agreement with literature on Ru silicide [29]. The presence of SiO_2 was only observed on the thin-film side of the delaminated Ru/Si(100) interface, whereas on the substrate the signal from SiO_x species was below the detection limit in the Si 2p region [Figure 2.6 (c) and Figure 2.6 (d)] and the O 1s signal was very low [≤2%, see Figure 2.2 (c)]. In the region probed by XPS, the thin-film side of the Ru/Si(100) interface exhibited a ratio of oxidized silicon to the sum of Ru and total Si of $SiO_x/(Ru + Si_{tot})$≈20%, a value that is higher than the SiO_2/Si_{tot} ratio measured for a Si(100) substrate with native oxide (approximately 11%). No traces of ruthenium were detected on the substrate after the delamination. We conclude that the native oxide delaminated from the substrate together with the Ru thin film in its entirety and remained at least partly intact. The higher SiO_2 signal on Ru silicide is attributed to a shorter inelastic mean-free path of photoelectrons in the Ru silicide layer, which led to a lower measured intensity of Ru and Si. These observations indicate a sharp

separation at the Si-SiO_2 interface with negligible intermixing after Si diffusion.

We tested whether or not the observed delamination behavior is specific for Ru layers on Si(100) by repeating the same procedure for Mo and for Ru-Mo alloys of four different compositions ($Ru_{100-x}Mo_x$). In addition to the effect of composition, the study of Ru-Mo alloys allowed us to assess the effect of structural disorder, since a high Ru content was reported to favor the growth of polycrystalline films, while approximately equiatomic compositions were found to assume an amorphous structure for deposition at room temperature [30]. Figure 2.3 (a) summarizes the observed effect of composition and structure on the delamination of Ru-Mo films. Reproducible delamination was achieved for all five investigated Ru-containing compositions (pure Ru to $Ru_{41}Mo_{59}$), proving that the effect is not limited to a narrow compositional range or a certain crystallographic structure. For pure Mo, we did not succeed in producing free-standing nanolayers by delamination from the substrate up to annealing temperatures of 700°C [red line in Figure 2.3 (a)]. No other indications of reduced adhesion were observed for the annealed Mo films. We therefore conclude that for the binary Ru-Mo system the presence of Ru is essential for the reported delamination mechanism.

The necessary ingredients for delamination were further explored by varying the substrate properties and deposition technique. No delamination was observed for Ru films on Si(100) without its native SiO_2 layer, which had been removed via etching with hydrofluoric acid. Thicker interlayers of SiO_2 (approximately 20 nm), achieved by annealing the substrates in air, also prevented delamination, most likely by inhibiting Si diffusion. The orientation of the substrate plays a decisive role as well, demonstrated by annealing Ru layers on native-oxide terminated Si(111), for which no tendency towards lower adhesion was observed. Also a change in deposition method to pulsed laser deposition (PLD) in UHV modified the Ru/SiO_2/Si(100) sufficiently to avoid delamination, whereas silicide formation was still observed upon annealing. The highly reproducible effect observed on sputter-deposited Ru/SiO_2/Si(100) was thus found to be strongly affected by small variations in interface properties, such as surface energy, defect density, and diffusivity in the oxide layer.

Figure 2.3 (b) and Figure 2.3 (c) show scanning electron microscopy (SEM) images of the free-standing film at the thin-film side of the Ru/Si(100) interface [Figure 2.3 (b)] and of the substrate [Figure 2.3 (c)] after delaminating a 200 nm thick $Ru_{77}Mo_{23}$ film. The thin-film side of the Ru/Si(100) interface is imaged as a smooth surface with nanoscale speckles that we attribute to small crystallites in the annealed silicide layer. The most prominent features in the images are micrometer-sized protrusions with a volcanolike shape, characterized by a thin cracked layer lifted off the film and a dark “crater”. A large fraction of the electrons from this central region is prevented from reaching the detector, which is positioned at an angle of approximately 30° with respect to the sample surface, resulting in a lack of signal. The volcanolike appearance indicates a violent process of formation, breaking up a thin overlayer of the Ru-based film by pulling (or pushing) it upwards. We propose that these structures form during the exfoliation step at locations where the film is still connected to the substrate after annealing.

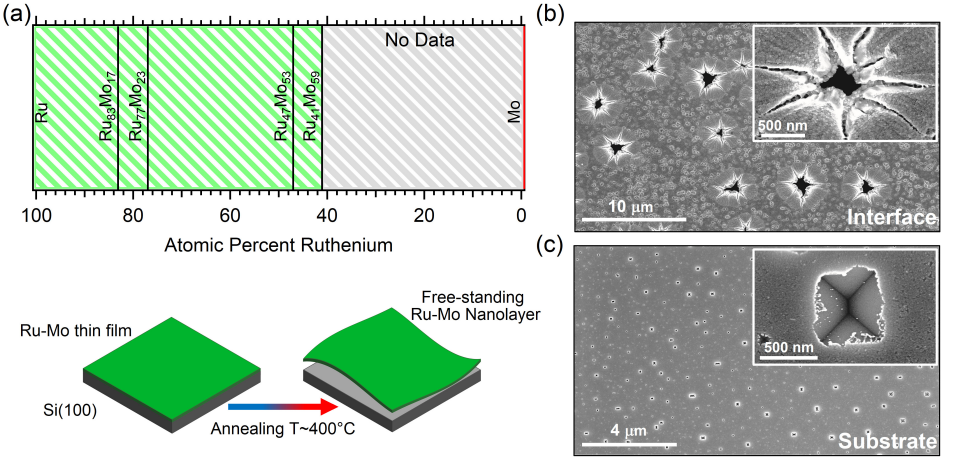

Figure 2.3 *(a) Schematic summary of the different Ru-Mo thin films investigated. The production of free-standing Ru-Mo nanolayers (sketch at the bottom) was successful for pure Ru and all alloy compositions in this study (green area). For pure Mo (red line) no delamination was observed. (b) SEM micrograph of a 200 nm thick $Ru_{77}Mo_{23}$ film, delaminated upon annealing at 700 °C and viewed from the side that had been in contact with the Si(100) substrate. (c) SEM micrograph of the Si(100) substrate after annealing and exfoliation of the same $Ru_{77}Mo_{23}$ film.*

The strong adhesion at these "defects" leads to a local breakup of an overlayer upon mechanical exfoliation. In Figure 2.3 (c) a SEM micrograph of the substrate after exfoliation shows the presence of a high number of rectangular cavities. The zoomed-in image in the inset reveals that these cavities have the shape of inverse pyramids of missing silicon in the single-crystalline Si(100) substrate. In the context of the silicide formation reported above, it is likely that these inverse pyramids are etch pits, which have been observed as a result of silicide formation on Si(100) for several metals [31, 32]. Typically the faces of the pyramids follow the crystal plane with the lowest surface energy. For Si, these are the 111 planes [33], which form facets at an angle of 54.7° with respect to the (100) plane [34].

The high-resolution transmission electron microscopy (HR-TEM) measurements of a 20 nm thick $Ru_{47}Mo_{53}$ thin film in Figure 2.4 provide mechanistic insights into the delamination process. Figure 2.4 (a) shows a cross-sectional high-resolution TEM image of the as-grown amorphous $Ru_{47}Mo_{53}$ thin film on a Si(100) substrate with native SiO_2 layer. The topmost layer labeled Pt/C is required for TEM sample preparation using focused-ion-beam cutting. In Figure 2.4 (b) a zoomed-in section of the $Ru_{47}Mo_{53}$ thin film is reported, highlighted with a dashed square in Figure 2.4 (a). The complete lack of long-range order is evident in the image and can also be inferred from the two-dimensional fast Fourier transform (2D-FFT) pattern in the inset. The absence of preferred orientations and of long-range order results in a broad ring without sharp features in reciprocal space [30]. The

right-hand side of Figure 2.4 shows HR-TEM images of the $Ru_{47}Mo_{53}$ thin film after annealing. The image in Figure 2.4 (c) shows that the amorphous Ru-Mo film has detached from the Si(100) surface with annealing at 400°C. The light gray region between the Ru-Mo layer and the Si substrate corresponds to empty space created by the detachment of the alloy layer. The darker shaded regions close to the substrate and the metal film are a result of oxidation and carbon accumulation during focused-ion-beam cutting (see also Figure 2.10 [27]). A detailed image of the amorphous Ru-Mo layer after annealing is available in Figure 2.7 [27]. The dashed white box in Figure 2.4 (c) highlights one of the few locations where the nanolayer remained locally attached to the substrate since no mechanical force was applied to complete the exfoliation. The composition of the highlighted region was investigated using energy-dispersive x-ray spectroscopy (EDX) maps of Ru, Mo, Si, and O in Figure 2.4 (d)–(g). These measurements reveal the diffusion of silicon from the substrate into the alloy thin film with annealing. The delaminated Ru-Mo layer contains a substantial fraction of Si, whereas the as-deposited Ru-Mo film contains no Si (Figure 2.8 [27]). On the other hand, no diffusion of Ru and Mo to the Si substrate was observed, as shown in Figure 2.4 (e) and Figure 2.4 (f), respectively. In addition to the change in composition, the TEM measurements show that the thickness of the metallic thin film has increased from 20 nm before annealing [Figure 2.4 (a)] to approximately 32–33 nm afterwards [Figure 2.4 (c)], corresponding to a swelling by more than 60% with respect to the as-grown film.

In addition to the production of Ru-based membranes, we demonstrate that Ru delamination can serve as a pathway to achieve free-standing layers of custom composition. Very thin Ru buffer layers were found sufficient to enable the exfoliation of free-standing metal nanolayers. For sputter-deposited, 200 nm thick Mo films, a Ru buffer layer of only 5 nm thickness was enough to enable exfoliation after annealing at 600°C. The characteristic change in reflectivity that indicates the detachment from the substrate was observed already at around 400°C. For a 45 nm thick film of the high-entropy alloy HfMoNbTiZr (20:20:20:20:20 at.%) deposited using PLD, no delamination occurred for 5 nm Ru, but successful exfoliation of an intact stack of HfMoNbTiZr/Ru/SiO_2 [Figure 2.9 (a)] was achieved for a 20 nm thick Ru buffer layer. We attribute the higher required thickness to intermixing of the deposited HfMoNbTiZr with the thin Ru layer upon deposition, caused by the high kinetic energy of the material arriving at the surface during the PLD process. XPS spectra of successfully delaminated films showed only Ru and Si close to the interface with the Si substrate [Figure 2.9 (b)], indicating that no significant alloying between Ru and other metals in the stack occurred at the temperature required for delamination.

The combined evidence from *in situ* XPS, visual observation during annealing, HR-TEM, EDX, and SEM enables us to propose a qualitative delamination mechanism. Already at 400°C, Si atoms diffuse through the native SiO_2 layer on Si(100) into the Ru film. The formation of Ru silicide is thermodynamically favorable and readily proceeds at 400°C, leading to the incorporation of substantial amounts of Si. The incorporated Si results in swelling of the film and the buildup of in-plane compressive stress. However, with all bonds at the interface intact, the

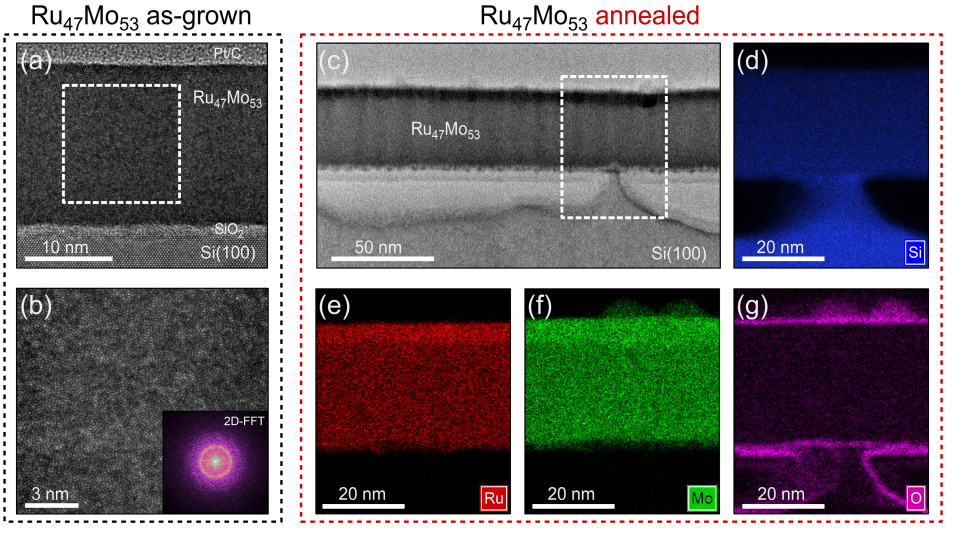

Figure 2.4 *HR-TEM measurements of a 20 nm thick $Ru_{47}Mo_{53}$ thin film. (a) TEM image of the as-grown sample showing the crystalline Si(100) substrate, the disordered native SiO_2, and the amorphous metallic thin film. (b) Zoomed-in region of the $Ru_{47}Mo_{53}$ thin film [white square in (a)], and corresponding 2D-FFT filtered using a Hann function (inset), both adapted from Yetik et al. [30]. (c) TEM image of the $Ru_{47}Mo_{53}$ thin film after annealing at 400 °C. (d)–(g) EDX maps of the white dashed rectangular area in (c) for Si, Ru, Mo and O.*

barrier for cleaving is high and the $Ru/SiO_2/Si$ structure remains intact. However, if the layer detaches in one location, for example at one of the pyramidal cavities in the Si substrate, the layer can buckle to locally release the compressive stress caused by Si incorporation. The atoms directly adjacent to this detached region experience a strong localized force pulling them off the substrate in addition to the high compressive stress in the layer. This combination results in the breaking of bonds and the growth of the delaminated region, which propagates across the sample in an avalanchelike manner. The *in situ* XPS results confirm that the breaking point is the interface between Si(100) and SiO_2. This interface is expected to be the energetically most favorable one to cleave, based on reports of the surface energies of low-index Si surfaces [35], their native SiO_2 layers [36], and on a higher surface energy of Ru silicide compared to Si(111) [37]. The delaminated layer remains attached to the substrate at a small number of locations, for example at defects leading to crystallization of particles at the interface, and is removed upon mechanical exfoliation.

The HR-TEM images support the proposed mechanism in several respects. In combination with EDX, they provide information on the diffusing species, the presence of the native oxide, and the total layer thickness. The EDX results demonstrate that annealing treatment results in the diffusion of silicon into the film, whereas no indications for metal diffusion are observed, which is the

dominant mechanism of silicide formation for several transition metals such as Ni [38]. The images further indicate that the native oxide layer remains largely intact, which is also confirmed using *in situ* XPS. In Figure 2.4 (g) the oxide layer appears to be thinner and shows spatial variations in density at the connecting point between film and substrate: this observation indicates that defects in the silicon native oxide may facilitate the diffusion of Si. This is particularly relevant since no Si diffusion in amorphous silica is expected at 400°C [39], in agreement with the absence of the delamination effect for Ru on thicker SiO_2 layers at otherwise comparable conditions. The formation of silicide thus indicates that the native oxide is either sufficiently thin to allow for Si diffusion or locally damaged, for example during sputter deposition, where energetic ions can create defects that act as diffusion channels and define the starting points of silicide formation. According to the TEM results, however, the Si is not localized to a small number of channels but homogeneously distributed in the metal film converted to silicide. This conversion leads to a considerable increase in equilibrium volume (from about 0.014 to 0.034 nm^3/Ru for the example of Ru_2Si_3) [40], which exceeds the thermal expansion of all materials in this study over the relevant temperature range by several orders of magnitude. This increase in volume is borne out by a substantially larger film thickness (by ≈ 60%) observed in TEM images. In-plane expansion, however, is blocked by bonds at the interface, preventing full equilibration of the volume and creating extrinsic compressive stress in the layer [25]. This is in agreement with the observed buckling upon delamination.

The proposed mechanism further highlights that all three components of the Ru/SiO_2/Si(100) stack are imperative for the delamination to occur. The interface between Si(100) and its thin native SiO_2 layer is crucial as the location of separation, indicated by the unsuccessful attempts to generalize the effect to modified interfaces, for example without SiO_2, with a thicker SiO_2 layer, or with different surface orientation of Si. An oxide layer of finite thickness is essential for the detachment, since it ensures a favorable cleavage point with low-energy surfaces for both the substrate and the free-standing film. The absence of oxygen from the Si(100) substrate indicates the preference to cleave at a well-defined plane, minimizing the roughness and number of broken Si-O bonds. The importance of an intact SiO_2-Si interface and oxide layer is highlighted by the absence of delamination for pulsed laser deposited films, which most likely grow on an oxide that is damaged by high-energy atoms and ions during the deposition process. The relevance of the surface orientation is most likely related to the removal of Si from the surface layer. In the case of Si(100), this removal leads to the formation of cavities with 111-oriented faces, which are not expected to occur in the same way on Si(111) but could have an essential role, for example as starting points for the detachment and buckling of the film. The importance of the element Ru is clear from the reported observations, but the reasons for this selectivity remain unclear. The preference for Si as a diffusing species in the formation of Ru silicide establishes a clear difference to other transition metals such as Ni [38]. The tendency of Ru to form silicides with significantly larger volume at low temperature is not sufficiently different from Mo [41] to explain the observed selectivity. The

preference of Ru for hexagonal structures is not expected to play a decisive role based on the observed delamination of amorphous Ru-Mo layers. We speculate that a strong interfacial adhesion at the Ru-SiO_2 interface mediates the transfer of strain to the SiO_2-Si(100) interface, potentially related to the coexistence of Ru silicide and small metallic contributions observed in XPS of the thin-film side of the delaminated Ru/Si(100) interface.

Finally, the templating experiments with thin Ru buffer layers can also be explained with the same mechanism. The results indicate that Ru is essential at the interface, but already 5 nm of Ru buffer layer is sufficient to allow for major modifications of the metal film without interfering with the delamination. The increase in required thickness for the high-entropy alloy deposited using PLD, a deposition technique with high-energy particles impinging at the surface, indicates that an intact interface with SiO_2 and a minimum thickness of continuous Ru in the first nanometers of the film is essential. For Ru thicknesses surpassing a critical value, the process is expected to be independent of the deposition technique and should even allow for growth in reactive atmosphere and at elevated temperature, provided the Ru layer remains intact and silicide formation does not occur before inducing delamination. Moreover, this approach could also be applicable to other functional materials, such as oxides, other ceramics, and high-temperature polymers.

2.4 CONCLUSIONS

Our results demonstrate that annealing thin Ru-based films on Si(100) with native oxide leads to the delamination of centimeter-sized free-standing nanolayers, which detach from the substrate at the sharp interface between Si and its native oxide. We propose an explanation of the effect based on stress caused by the conversion of the Ru layer to Ru silicide, concomitant with a strong increase in the equilibrium volume of the film and the buildup of compressive stress. The layer responds by buckling, starting locally at pyramidal cavities in the Si substrate. Once the layer can detach locally, which is easiest at the pyramidal cavities in the Si substrate, it starts buckling. The detached region grows in an avalanchelike manner, creating an ultrathin free-standing membrane and leaving behind a clean Si substrate. We demonstrate that the delamination effect can be generalized to the pure metal Mo and the PLD-grown complex alloy HfMoNbTiZr by making use of thin Ru buffer layers. The delamination of Ru-supported layers thus shows potential to enable the chemical-free fabrication of metal nanolayers of custom composition. This approach is compatible with a variety of deposition techniques and growth conditions as well as fully vacuum-based processing, while remaining simple and environmentally friendly.

REFERENCES

[1] Y. Liang, S. Zhang, X. Cao, Y. Lu, and T. Xu. "Free-standing plasmonic metal-dielectric-metal bandpass filter with high transmission efficiency". In: *Scientific Reports* 7.1 (2017), p. 4357. ISSN: 20452322. DOI: 10.1038/s41598-017-04540-9.

[2] F. R. Powell, P. W. Vedder, J. F. Lindblom, and S. F. Powell. "Thin film filter performance for extreme ultraviolet and x-ray applications". In: *Optical Engineering* 29(6).6 (1990), pp. 614–624. DOI: 10.1117/12.55641.

[3] K. Jimenez, P. Nicolosi, L. Juschkin, N. Ahmed, A. E. Gaballah, E. Cattaruzza, M. G. Sertsu, A. Gerardino, A. Giglia, G. Mussler, and P. Zuppella. "Extreme ultraviolet free-standing transmittance filters for high brilliance sources, based on Nb/Zr and Zr/Nb thin films on Si_3N_4 membranes: Design, fabrication, optical and structural characterization". In: *Thin Solid Films* 695.April 2019 (2020), p. 137739. ISSN: 00406090. DOI: 10.1016/j.tsf.2019.137739.

[4] K. Han, L. Wu, Y. Cao, H. Wang, C. Ye, K. Huang, M. Motapothula, H. Xing, X. Li, D. C. Qi, X. Li, and X. Renshaw Wang. "Enhanced Metal-Insulator Transition in Freestanding VO_2 Down to 5 nm Thickness". In: *ACS Applied Materials and Interfaces* 13.14 (2021), pp. 16688–16693. ISSN: 19448252. DOI: 10.1021/acsami.1c01581.

[5] B. S. Yin, Z. B. Wang, S. W. Zhang, C. Liu, Q. Q. Ren, and K. Ke. "In Situ Growth of Free-Standing All Metal Oxide Asymmetric Supercapacitor". In: *ACS Applied Materials and Interfaces* 8.39 (2016), pp. 26019–26029. ISSN: 19448252. DOI: 10.1021/acsami.6b08037.

[6] R. Govind and D. Atnoor. "Development of a Composite Palladium Membrane for Selective Hydrogen Separation at High Temperature". In: *Industrial and Engineering Chemistry Research* 30.3 (1991), pp. 591–594. ISSN: 15205045. DOI: 10.1021/ie00051a024.

[7] S. Adhikari and S. Fernando. "Hydrogen membrane separation techniques". In: *Industrial and Engineering Chemistry Research* 45.3 (2006), pp. 875–881. ISSN: 08885885. DOI: 10.1021/ie0506441.

[8] C. Zoldesi, K. Bal, B. Blum, G. Bock, D. Brouns, F. Dhalluin, N. Dziomkina, J. D. A. Espinoza, J. de Hoogh, S. Houweling, M. Jansen, M. Kamali, A. Kempa, R. Kox, R. de Kruif, J. Lima, Y. Liu, H. Meijer, H. Meiling, I. van Mil, M. Reijnen, L. Scaccabarozzi, D. Smith, B. Verbrugge, L. de Winters, X. Xiong, and J. Zimmerman. "Progress on EUV pellicle development". In: *Extreme*

Ultraviolet (EUV) Lithography V 9048.1 (2014), 90481N. ISSN: 1996756X. DOI: 10.1117/12.2049276.

[9] E. E. Gallagher, J. Vanpaemel, I. Pollentier, H. Zahedmanesh, C. Adelmann, C. Huyghebaert, R. Jonckheere, and J. U. Lee. "Properties and performance of EUVL pellicle membranes". In: *Photomask Technology 2015* 9635 (2015), p. 96350X. ISSN: 1996756X. DOI: 10.1117/12.2199076.

[10] D. L. Goldfarb. "Fabrication of a full-size EUV pellicle based on silicon nitride". In: *Photomask Technology 2015* 9635.914 (2015), 96350A. ISSN: 1996756X. DOI: 10.1117/12.2196901.

[11] H. J. Shin, I. S. Park, Y. J. Jang, S. J. Wi, G. S. Lee, and J. Ahn. "Fabrication of free-standing nanoscale SiN_x membranes with enhanced burst pressure via improved etching process". In: *Sensors and Actuators, A: Physical* 297 (2019), p. 111538. ISSN: 09244247. DOI: 10.1016/j.sna.2019.111538.

[12] X. Kong, K. Xu, C. Zhang, J. Dai, S. Norooz Oliaee, L. Li, X. Zeng, C. Wu, and Z. Peng. "Free-Standing Two-Dimensional Ru Nanosheets with High Activity toward Water Splitting". In: *ACS Catalysis* 6.3 (2016), pp. 1487–1492. ISSN: 21555435. DOI: 10.1021/acscatal.5b02730.

[13] H. Liu, C. Xi, J. Xin, G. Zhang, S. Zhang, Z. Zhang, Q. Huang, J. Li, H. Liu, and J. Kang. "Free-standing nanoporous NiMnFeMo alloy: An efficient non-precious metal electrocatalyst for water splitting". In: *Chemical Engineering Journal* 404.January 2020 (2021), p. 126530. ISSN: 13858947. DOI: 10.1016/j.cej.2020.126530.

[14] K. H. Seng, J. Liu, Z. P. Guo, Z. X. Chen, D. Jia, and H. K. Liu. "Free-standing V_2O_5 electrode for flexible lithium ion batteries". In: *Electrochemistry Communications* 13.5 (2011), pp. 383–386. ISSN: 13882481. DOI: 10.1016/j.elecom.2010.12.002.

[15] N. Luo, G. J. Ji, H. F. Wang, F. Li, Q. C. Liu, and J. J. Xu. "Process for a Free-Standing and Stable All-Metal Structure for Symmetrical Lithium-Oxygen Batteries". In: *ACS Nano* 14.3 (2020), pp. 3281–3289. ISSN: 1936086X. DOI: 10.1021/acsnano.9b08844.

[16] Y. L. Ding, Y. Wen, P. A. Van Aken, J. Maier, and Y. Yu. "Rapid and Up-Scalable Fabrication of Free-Standing Metal Oxide Nanosheets for High-Performance Lithium Storage". In: *Small* 11.17 (2015), pp. 2011–2018. ISSN: 16136829. DOI: 10.1002/smll.201402502.

[17] N. Setter. *Electroceramic-Based MEMS*. Ed. by N. Setter. Springer US, 2005, pp. XII, 414. ISBN: 0387233105.

[18] J. A. Thornton. "Stress-Related Effects in Thin Films". In: *Thin Solid Films* 171 (1989), pp. 5–31. DOI: 10.1016/0040-6090(89)90030-8.

[19] M. F. Doerner and W. D. Nix. "Stresses and deformation processes in thin films on substrates". In: *Critical Reviews in Solid State and Materials Sciences* 14.3 (1988), pp. 225–268. DOI: 10.1080/10408438808243734.

[20] K. Kinosita. “Recent developments in the study of mechanical properties of thin films”. In: *Thin Solid Films* 12.1 (1972), pp. 17–28. ISSN: 00406090. DOI: 10.1016/0040-6090(72)90387-2.

[21] B. Lu, Y. Song, Z. Guo, and J. Zhang. “Modeling of progressive delamination in a thin film driven by diffusion-induced stresses”. In: *International Journal of Solids and Structures* 50.14-15 (2013), pp. 2495–2507. ISSN: 00207683. DOI: 10.1016/j.ijsolstr.2013.04.003.

[22] R. Mainz, H. Rodriguez-Alvarez, M. Klaus, D. Thomas, J. Lauche, A. Weber, M. D. Heinemann, S. Brunken, D. Greiner, C. A. Kaufmann, T. Unold, H. W. Schock, and C. Genzel. “Sudden stress relaxation in compound semiconductor thin films triggered by secondary phase segregation”. In: *Physical Review B - Condensed Matter and Materials Physics* 92.15 (2015), pp. 1–8. ISSN: 1550235X. DOI: 10.1103/PhysRevB.92.155310.

[23] Y. Kuru, M. Wohlschlögel, U. Welzel, and E. J. Mittemeijer. “Interdiffusion and stress development in Cu-Pd thin film diffusion couples”. In: *Thin Solid Films* 516.21 (2008), pp. 7615–7626. ISSN: 00406090. DOI: 10.1016/j.tsf.2008.05.011.

[24] P. Gas and F. M. D’Heurle. “Formation of silicide thin films by solid state reaction”. In: *Applied Surface Science* 73.C (1993), pp. 153–161. ISSN: 01694332. DOI: 10.1016/0169-4332(93)90160-D.

[25] O. Thomas, P. Gergaud, C. Rivero, and F. D’Heurle. “Stress development during the reactive formation of silicide films”. In: *Defect and Diffusion Forum* 237-240.PART 2 (2005), pp. 801–812. ISSN: 16629507. DOI: 10.4028/www.scientific.net/ddf.237-240.801.

[26] V. E. Borisenko. *Semiconducting Silicides*. 1st ed. Springer Berlin Heidelberg, 2000, p. 50. ISBN: 978-3-540-66111-5.

[27] See http://link.aps.org/supplemental/10.1103/PhysRevMaterials.6.043402 for a video of the change in appearance of a Ru thin film during annealing. See the Appendix for XPS survey and Si 2p spectra of the delaminated interface, TEM images, as well as TEM-EDX results of an annealed Ru-Mo alloy layer.

[28] D. J. Morgan. “Resolving ruthenium: XPS studies of common ruthenium materials”. In: *Surface and Interface Analysis* 47.11 (2015), pp. 1072–1079. ISSN: 10969918. DOI: 10.1002/sia.5852.

[29] L. Pasquali, N. Mahne, M. Montecchi, V. Mattarello, and S. Nannarone. “Formation and distribution of compounds at the Ru-Si(001) ultrathin film interface”. In: *Journal of Applied Physics* 105.4 (2009). ISSN: 00218979. DOI: 10.1063/1.3079507.

[30] G. Yetik, A. Troglia, S. Farokhipoor, S. van Vliet, J. Momand, B. J. Kooi, R. Bliem, and J. W. Frenken. “Ultrathin, sputter-deposited, amorphous alloy films of ruthenium and molybdenum”. In: *Surface and Coatings Technology* 445 (2022), p. 128729. ISSN: 0257-8972. DOI: 10.1016/j.surfcoat.2022.128729.

[31] K.-C. Park and K.-B. Kim. “Effect of Annealing of Titanium Nitride on the Diffusion Barrier Property in Cu Metallization”. In: *Journal of The Electrochemical Society* 142.9 (1995), pp. 3109–3115. ISSN: 0013-4651. DOI: 10.1149/1.2048697.

[32] G. H. Shen, J. C. Chen, C. H. Lou, S. L. Cheng, and L. J. Chen. “The growth of pinhole-free epitaxial $DySi_{2-x}$ films on atomically clean Si(111)”. In: *Journal of Applied Physics* 84.7 (1998), pp. 3630–3635. ISSN: 00218979. DOI: 10.1063/1.368538.

[33] R. J. Jaccodine. “Surface Energy of Germanium and Silicon”. In: *Journal of The Electrochemical Society* 110.6 (1963), p. 524. ISSN: 00134651. DOI: 10.1149/1.2425806.

[34] A. A. Baski, S. C. Erwin, and L. J. Whitman. “The structure of silicon surfaces from (001) to (111)”. In: *Surface Science* 392.1-3 (1997), pp. 69–85. ISSN: 00396028. DOI: 10.1016/S0039-6028(97)00499-8.

[35] A. A. Stekolnikov, J. Furthmüller, and F. Bechstedt. “Absolute surface energies of group-IV semiconductors: Dependence on orientation and reconstruction”. In: *Physical Review B - Condensed Matter and Materials Physics* 65.11 (2002), pp. 1–10. ISSN: 1550235X. DOI: 10.1103/PhysRevB.65.115318.

[36] S. R. Narayan, J. M. Day, H. L. Thinakaran, N. Herbots, M. E. Bertram, C. E. Cornejo, T. C. Diaz, K. L. Kavanagh, R. J. Culbertson, F. J. Ark, S. Ram, M. W. Mangus, and R. Islam. “Comparative Study of Surface Energies of Native Oxides of Si(100) and Si(111) via Three Liquid Contact Angle Analysis”. In: *MRS Advances* 3.57-58 (2018), pp. 3379–3390. ISSN: 20598521. DOI: 10.1557/adv.2018.473.

[37] M. Toramaru, N. Kobayashi, N. Kawamura, S. Ohno, Y. Miyamoto, and K. Shudo. “Nanoscale relaxation in Ru-Si growth on a silicon (111) surface”. In: *Surface and Interface Analysis* 45.7 (2013), pp. 1109–1112. ISSN: 01422421. DOI: 10.1002/sia.5235.

[38] M. Liehr, H. Dallaporta, and J. E. Lewis. “Defect formation in SiO_2/Si(100) by metal diffusion and reaction”. In: *Applied Physics Letters* 53.June (1988), pp. 589–591. DOI: 10.1063/1.100630.

[39] M. L. F. Nascimento and E. D. Zanotto. “Diffusion processes in vitreous silica revisited”. In: *Physics and Chemistry of Glasses: European Journal of Glass Science and Technology Part B* 48.4 (2007), pp. 201–217. ISSN: 00319090.

[40] D. Poutcharovsky and E. Parthé. “The Orthorhombic Crystal Structure of Ru_2Si_3, Ru_2Ge_3, Os_2Si_3 and Os_2Ge_3”. In: *Acta Crystallographica Section B* 30 (1974), pp. 2692–2696. DOI: 10.1107/S0567740874007825.

[41] I. Nedelcu, R. W. van de Kruijs, A. E. Yakshin, and F. Bijkerk. “Thermally enhanced interdiffusion in Mo/Si multilayers”. In: *Journal of Applied Physics* 103 (2008), p. 083549. DOI: 10.1063/1.2907964.

APPENDIX

Video Live delamination of a 100 nm Ru thin film during annealing in UHV at approximately 400°C. The sample is mounted onto a standard Omicron plate with spot-welded Ta strips. As a result of annealing, an area on the left side of the sample changes in appearance (lower reflectivity and higher apparent roughness). The modified area expands, propagating across the entire film towards the right side of the sample in a few seconds. The video is available at http://link.aps.org/supplemental/10.1103/PhysRevMaterials.6.043402

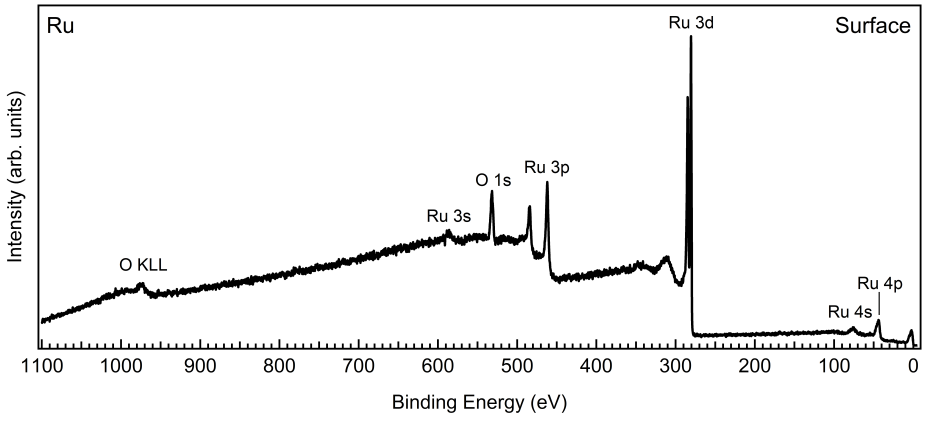

Figure 2.5 *Ex situ XPS investigation of a 100 nm thick Ru thin film after annealing but prior to exfoliation (film still on the substrate): the XPS survey shows the presence of only Ru and O without any traces of Si.*

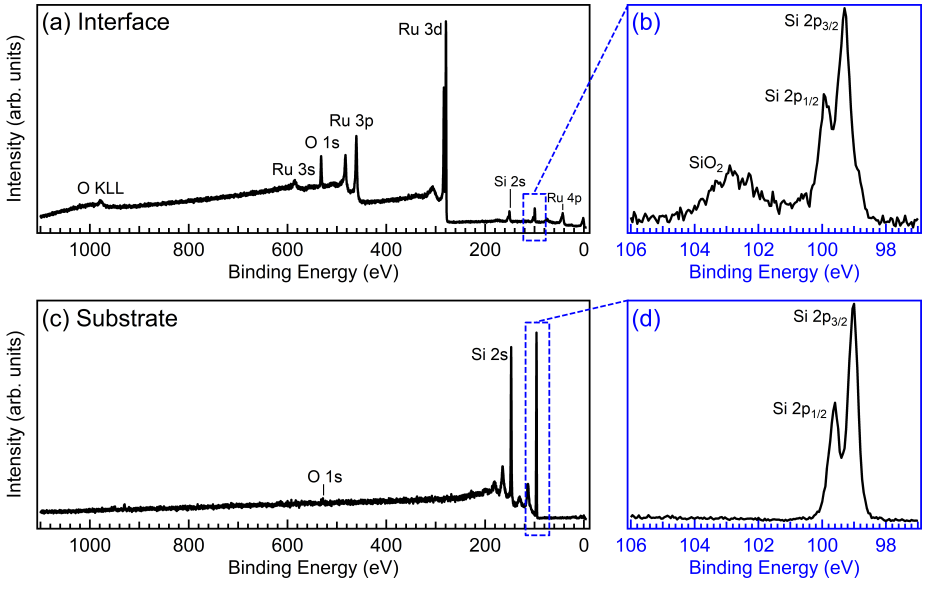

Figure 2.6 *In situ XPS investigation of the Ru/Si(100) interface and bare substrate after annealing and exfoliation in UHV. (a) XPS survey of the Ru/Si(100) interface showing the presence of O, Ru and Si. (b) Detailed measurement of the Ru/Si(100) interface Si 2p region: the main Si 2p doublet is shifted 0.3 eV towards a higher binding energy value with respect to elemental Si, compatible with Ru silicide. The small shoulder visible around 99 eV of binding energy is assigned to elemental Si. The broad peak detected around 103 eV of binding energy is assigned to SiO_2 (c) XPS survey of the bare substrate showing the presence of Si and small traces of O; a copper contamination (below 0.2%, as determined from the peak area) is also detected at 932 eV of binding energy. (d) Detailed measurement of the bare substrate Si 2p region: the main Si 2p doublet at approximately 99 eV is assigned to elemental Si. No traces of SiO_x species are detected.*

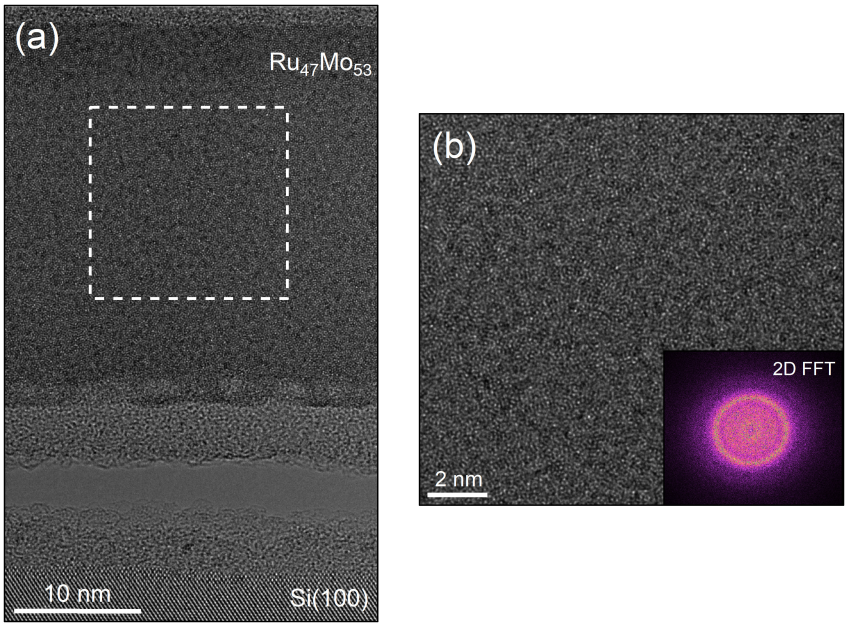

Figure 2.7 *High-resolution transmission electron microscopy (HR-TEM) measurements of a 20 nm thick $Ru_{47}Mo_{53}$ thin film after annealing at 400° C. (a) TEM image of the annealed sample showing the crystalline Si(100) substrate, the disordered native SiO_2, carbon layers accumulated during focused-ion-beam cutting, and the amorphous metallic thin film. (b) Zoomed-in region of the $Ru_{47}Mo_{53}$ thin film (white dashed square in (a)), and corresponding 2D-FFT filtered using a Hann function (inset).*

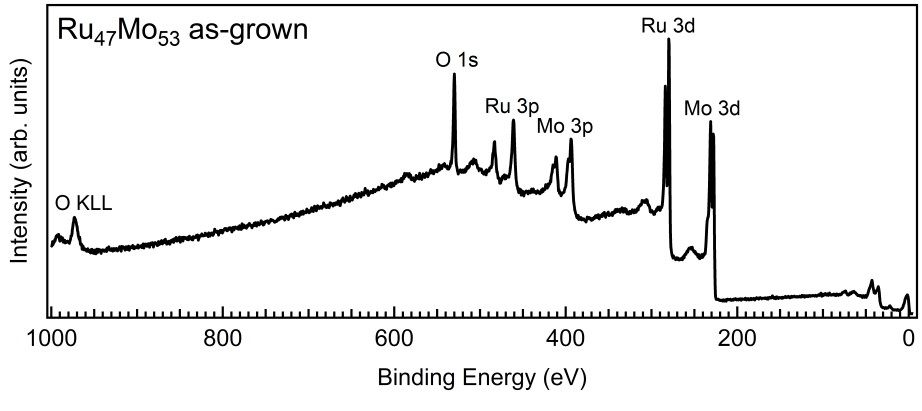

Figure 2.8 *Ex situ XPS investigation of an as-grown 20 nm $Ru_{47}Mo_{53}$ thin film prior to annealing and exfoliation: the XPS survey shows the presence of only Ru, Mo and O with no traces of Si.*

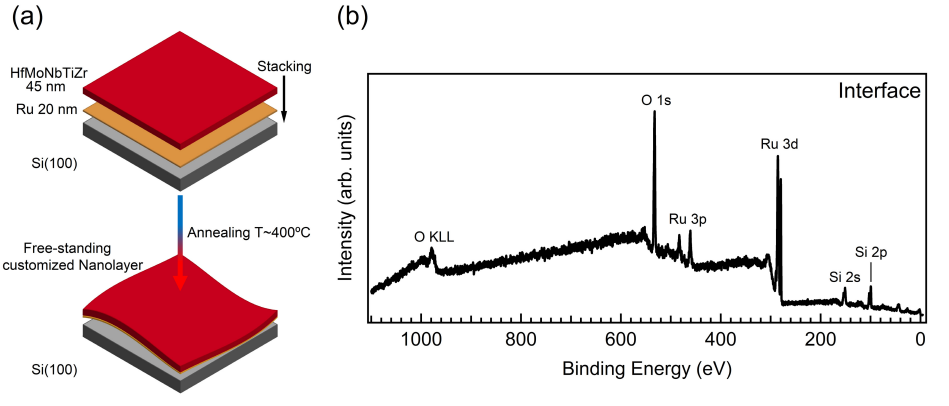

Figure 2.9 *(a) Sketch of the free-standing customized nanolayer fabricated using a 20 nm thick Ru thin film as a buffer layer between a 45 nm HfMoNbTiZr high-entropy alloy thin film and a Si(100) substrate with native oxide. (b) Ex situ XPS investigation of the HfMoNbTiZr/Ru/SiO_2 interface after annealing and exfoliation: only Ru, O and Si are detected with no traces of other metals.*

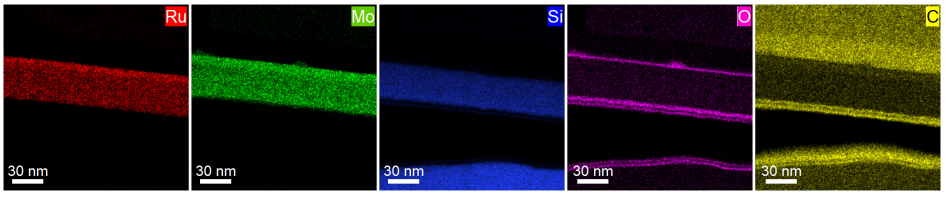

Figure 2.10 *HR-TEM EDX map of Ru, Mo, Si, O and C at a location where the $Ru_{47}Mo_{53}$ thin film is completely detached from the substrate. The black area underneath the film is empty space created by the detachment of the film from the substrate.*

3

TUNING MATERIAL PROPERTIES VIA DISORDER: FROM CRYSTALLINE ALLOY TO METALLIC GLASS

Pathways to tune the electronic, chemical, mechanical, and optical properties of solids without modifying their composition represent a new paradigm in the design of functional and sustainable materials. The level of structural disorder - from perfectly crystalline to fully amorphous – for example, induces remarkable changes in material properties. Typically, disorder is introduced by altering the composition of a material, adding to the misconception that these two properties cannot be decoupled. Here, we demonstrate that striking differences in the optical, electronic, and corrosion properties of CuZr are achieved by deliberately and reproducibly engineering the level of structural disorder in pulsed laser deposited thin films of a constant composition. This approach allows tuning the structure of CuZr from polycrystalline to fully amorphous, switching the nature of charge transport from metallic to semiconductor-like, the optical properties in the visible regime from opaque to transparent, and the corrosion behavior in air from mixed oxidation to the formation of a protective Zr oxide overlayer. Our results highlight the tunability of structural disorder in alloys and its remarkable effect on material properties, providing the opportunity to design sustainable functional materials based on customizing properties beyond their composition.

A. Troglia, V. Vollema, S. Cassanelli, E. van Heumen, J. van de Groep, A. de Visser, and R. Bliem. *Tuning material properties via disorder: From crystalline alloy to metallic glass.* Materials Today Physics **29**, 100893 (2022).

3.1 INTRODUCTION

Structural disorder in materials is intuitively often considered detrimental compared to the well-defined long-range order offered by crystalline solids. However, several examples of amorphous materials are known to exhibit superior properties to their crystalline counterparts. Metallic glasses [1–4], for example, have gained considerable attention due to their corrosion resistance [5, 6], mechanical strength [7, 8], wear resistance [9], and permeability for diffusion [10]. Excellent performance in catalysis has also been reported for other amorphous materials [11, 12]. The complete lack of long-range order at the atomic scale has been found to yield very different mechanical, optical and magnetic properties compared to crystalline materials [13–15]. In specific applications, the properties of amorphous solids already find appreciation in the thin-film regime, for example in microelectronic and biomedical devices and sensors [16, 17]. The penetration of amorphous materials into new technological fields of application is, however, partly limited by the perceived lack of flexibility in the structure of (established) materials.

In the context of thin films, structure plays a key role in several applications, such as perfectly conformal layers for electronics applications [18] or protective coatings against corrosion in reactive environments, where grain boundaries might act as diffusion channels and reactive points in crystalline films [19]. It has been shown that the amorphous structure is more resistant to oxidation compared to its polycrystalline counterpart due to the lack of structural order [20, 21]. Similarly, grain boundaries together with point defects and surface roughening strongly influence the charge transport properties in the thin-film regime [22]. Understanding and controlling the electrical conductivity at the nanometer scale is for example essential to increase the performance of integrated circuits. In this framework, structural disorder can thus be leveraged to tune the properties of thin films to specific applications.

Among the vast variety of thin-film metallic glasses that have been developed and investigated in literature, CuZr stands out as an ideal system for studying the fundamental role of structure. On the one hand, it is characterized by its excellent glass forming ability [23, 24]. On the other, many crystalline phases and intermetallic compounds are known to form at low temperature [25]. Thus, CuZr is a good model system to study how the thin-film structure affects the material's properties at the atomic scale, with several works reporting an amorphous structure for a wide range of Cu content (18–88 at.%) achieved with sputter-deposition [26, 27], co-evaporation [28] and pulsed laser deposition [29].

However, modifying the structure of a metallic thin film without affecting other properties is not straightforward. For instance, the amorphous phase in a binary metal alloy is usually dependent on the stoichiometry of its constituents [30, 31]. As mentioned, CuZr is a good example where the compositional range in which the amorphous phase is favored is particularly large. Other approaches to obtain a glassy structure involve very high cooling rates, which are typically in the order of 10^{14} Ks^{-1} for single-element metals [32] and approximately 10^{3} Ks^{-1} for selected binary alloys [33]. Thus, the deposition of metallic alloys with the same

composition but different structure requires dedicated fabrication methods.

In this work, we demonstrate that the level of structural disorder is tunable in thin films of identical composition by tuning the growth parameters of pulsed laser deposition (PLD), allowing for growth far from and close to equilibrium. Adjusting the level of disorder in the layer profoundly impacts the surface chemistry, the electronic transport properties, and the optical transparency of the thin films. Our results establish the essential role that structural disorder plays in the optoelectronic and chemical properties of CuZr thin films. We anticipate the engineering of material properties through structural disorder to be more universally applicable. Such structural tuning opens up a new paradigm in materials design, allowing for the optimization of functional solids for specific technological applications without the need to modify their composition.

3.2 RESULTS AND DISCUSSION

To systematically study the impact of disorder on optoelectronic and surface chemical properties of materials, we directly compare CuZr thin films of the same composition with different structure. The exclusive variation of structure is achieved by PLD, which is capable of growing well-defined crystalline as well as off-equilibrium disordered layers. We use the deposition temperature as parameter to vary the level of disorder in the layer, which we probe using grazing-incidence x-ray diffraction (GI-XRD).

Figure 3.1 (a) shows the results of the structural comparison of CuZr thin films deposited at room temperature (RT, blue curve) and at T≈500°C (red curve). The diffractograms are fundamentally different. GI-XRD of CuZr grown at RT results in a typical 'liquid-like' pattern expected from a fully amorphous thin film [31, 34]. It is characterized by a very broad peak centered at approximately 37.5° with a full-width at half maximum (FWHM) of 8.5° and a second broad feature at approximately 65.0° with a FWHM of 10.0°. No sharp peaks are present in the GI-XRD pattern. The residual sharp intensity variations above the noise threshold are correlated to the presence of a low density of large crystallites due to melt ejection during deposition. The effect of these droplets on the diffraction results is explained in the Appendix (Figure 3.7). On the contrary, the GI-XRD pattern of CuZr thin films deposited at T≈500°C (red curve in Figure 3.1) is characterized by the presence of several sharp peaks attributed to the formation of crystalline grains. The main peaks are located at approximately 33°, 38°, 40°, 44°, 46°, 67° and can be ascribed to different Cu-rich (Cu_8Zr_3 and $Cu_{10}Zr_7$) and Zr-rich ($CuZr_2$) crystal phases [24, 26, 27], highlighted by triangular, square and circular symbols, respectively. No peaks associated to undesired metal-oxide phases such as ZrO_2 [26, 35] were detected. Using the FWHM of the crystalline peaks and the Scherrer equation [36] the mean size of the ordered grains is estimated at approximately 10 nm, which is relatively large compared to the film thickness of this study (≈20 nm). The high-temperature deposition of the film within the crystallization temperature range (T_x≈444–527°C [37, 38]) thus allows for sufficient mobility to grow polycrystalline CuZr, consisting of relatively large Cu-rich and Zr-rich grains.

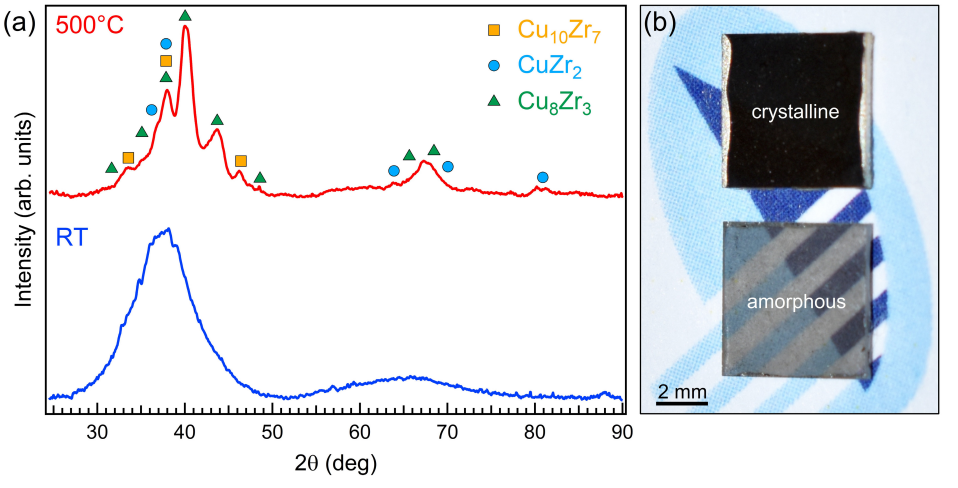

Figure 3.1 *(a) GI-XRD results of CuZr thin films deposited at room temperature (RT, blue curve) and at 500 °C (red curve). CuZr thin films grown at RT display two very broad, weak peaks, characteristic of an amorphous structure. In contrast, the growth at high temperature favors the formation of a polycrystalline structure of Cu-rich and Zr-rich grains. (b) Photograph of a polycrystalline (top) and amorphous (bottom) CuZr thin film showing stark differences in the visible optical properties: the amorphous film is partially transparent, while the polycrystalline film is opaque and dark.*

On the other hand, keeping the substrate at RT leads to a rapid quenching of the ablated material in an amorphous structure, which is favored in the compositional range chosen in this study [23, 24]. Annealing the amorphous layer is expected to induce crystallinity at comparable temperatures, but is expected to result in a broader distribution of crystallite sizes and stronger tendency towards break-up and dewetting.

Figure 3.1 (b) displays an optical photograph of the polycrystalline (top) and the amorphous (bottom) CuZr films, illustrating the dramatic influence of the level of structural disorder on the optical properties of CuZr in the visible spectral range. Despite having the same thickness, the amorphous CuZr thin film is partially transparent, while the polycrystalline layer is opaque, dark and reflective. While these images were acquired in air, the same difference in appearance is also observed immediately after growth in ultra-high vacuum (UHV).

Disorder is also considered a promising parameter to engineer the smoothness and homogeneity of coatings, which we probe using atomic force microscopy (AFM). Indeed, stark differences between the CuZr thin films deposited at RT and at T≈500°C are observed in the surface topography shown in Figure 3.2. The AFM micrograph of the amorphous film deposited at RT shows a smooth, near-featureless morphology down to the nanometer scale. In contrast, the polycrystalline film deposited at T≈500°C displays a richer morphology dominated by protruding

features with a typical diameter of 20–25 nm, comparable to the average thickness of the continuous film. The thin-film surface roughness is significantly lower for the amorphous film than for its polycrystalline counterpart, as quantified by respective root-mean-square height variations S_q of 0.5 nm and 2.4 nm. Such a difference is unsurprising, as the development of grain boundaries in a polycrystalline material is known to promote roughness [31]. Additionally, significant differences in roughness have been previously reported for sputter-deposited CuZr films of various compositions due to composition-induced changes in structure and crystallinity [27, 39]. Here, in contrast, the film composition is constant and the difference is thus only due to the absence/presence of crystallinity.

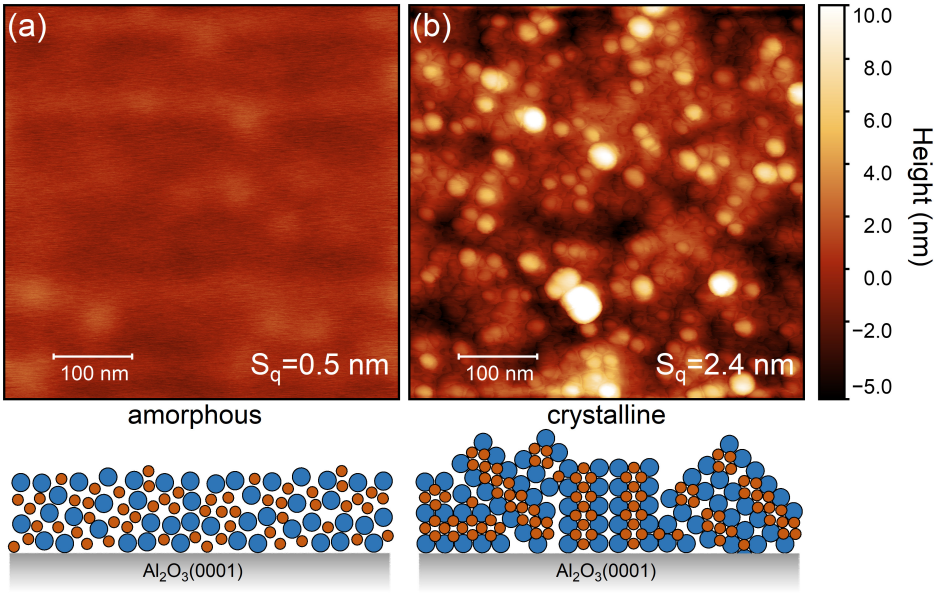

Figure 3.2 *Atomic force microscopy (AFM) micrographs of an amorphous (a) and a polycrystalline (b) CuZr thin film measured in air. Both images are displayed with the same height scale as indicated by the color bar. The amorphous film is characterized by a smooth surface with a very low surface roughness, whereas the polycrystalline film presents a grainy surface morphology with a much higher surface roughness, illustrated by the respective schematics below.*

To study the effect of structural disorder on the surface chemical properties of the CuZr thin films we use x-ray photoelectron spectroscopy (XPS) before and after air exposure. The thin films were first measured *in situ* after growth in UHV to infer the chemical composition and the purity level of the surface without air exposure. A survey spectrum of an as-grown CuZr thin film is reported in Figure 3.8 (a), showing only core-level peaks ascribed to Cu and Zr, with minor traces of oxygen contamination. The XPS results of amorphous and polycrystalline CuZr thin films after air exposure are reported in Figure 3.3. The detailed Cu 2p

regions of an amorphous (blue curve) and a polycrystalline (red curve) CuZr thin film exposed to air are compared to an as-grown film (black curve) measured *in situ* in Figure 3.3 (a). The Cu 2p spectrum of the air-exposed amorphous film almost exactly matches the spectrum of the as-grown film measured in UHV: the Cu $2p_{3/2}$ peak is fitted with a single component at a binding energy (E_B) of 932.9 eV (Figure 3.3 (b)), in good agreement with literature values for metallic Cu [40]. No satellite features characteristic of Cu oxide and hydroxide species [40] are detected in the blue and black spectra. To further confirm the assignment as metallic Cu and exclude Cu_2O, the Cu $L_3M_{4,5}M_5$ Auger parameter was calculated, since it has been shown that the Auger spectral line-shape and position directly depends on the Cu oxidation state and species [40, 41]. The Cu $L_3M_{4,5}M_5$ Auger spectrum is reported in Figure 3.9 (a): the main peak is located at E_B=567.4 eV, resulting in an Auger parameter α'=1851.1 eV [42], in excellent agreement with the expected value for Cu^0 [40]. These results indicate that Cu is fully metallic both in the as-grown and in the amorphous air-exposed CuZr thin film.

Polycrystalline CuZr, on the other hand, shows a very different Cu 2p XPS spectrum. The red curve in Figure 3.3 (a) shows the clear presence of a shoulder and a satellite feature at higher binding energy values. The detailed peak-fit reported in Figure 3.3 (c) reveals the presence of the main metallic Cu $2p_{3/2}$ peak at E_B=932.6 eV together with two sets of components ascribed to CuO and $Cu(OH)_2$ species [40]. The analysis of the corresponding Auger parameters further confirms these results (see Figure 3.9 (b)). These findings indicate that, in contrast to amorphous CuZr thin films, Cu is partially oxidized after air exposure in polycrystalline CuZr.

While air exposure led to very different results regarding the oxidation behavior of Cu in amorphous and polycrystalline CuZr thin films, the behavior of Zr is similar in both cases. Figure 3.10 reports the detailed XPS spectra of the Zr 3d region for amorphous CuZr (a) and polycrystalline CuZr (b) after air exposure. Both spectra display a main doublet ascribed to ZrO_2 [43], with a Zr $3d_{5/2}$ peak centered at $E_B \approx 182.8$ eV. A low-intensity peak at $E_B \approx 179.5$ eV ascribed to metallic Zr [43] is visible for the polycrystalline sample, while no other Zr species are detected in the amorphous film. Moreover, the relative surface composition of the films changes dramatically after air exposure, with a reduction of the total Cu XPS intensity and an enrichment of Zr at the surface in both amorphous and polycrystalline CuZr thin films (from XPS we estimate Cu:Zr=31:69 (±1 at.%) and Cu:Zr=39:61 (±1 at.%) for amorphous and polycrystalline, respectively).

To identify the difference in oxidation mechanism, the nature of the oxides formed on the amorphous and polycrystalline layers was investigated using Raman spectroscopy measurements in air. Figure 3.4 shows the recorded Raman shift for polycrystalline CuZr (red curve), amorphous CuZr (blue curve) and a bare Al_2O_3(0001) substrate (black curve). Again, a clear difference is visible as a function of the thin-film structure. The polycrystalline spectrum is characterized by two very broad but distinct peaks centered at around 277 cm^{-1} and 330 cm^{-1}, which can be ascribed to phonon modes in tetragonal ZrO_2 (t-ZrO_2) and CuO [44, 45], respectively, while no clear peaks are detected in the spectrum of the amorphous

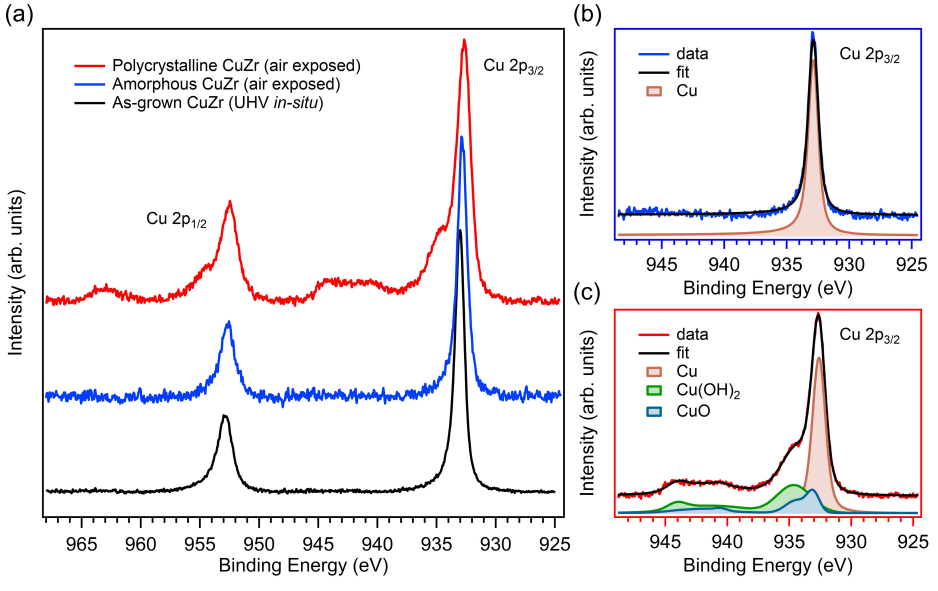

Figure 3.3 *X-ray photoelectron spectroscopy (XPS) measurements of amorphous vs. crystalline CuZr thin films exposed to air. (a) Cu 2p region of amorphous (blue) and crystalline (red) CuZr thin films after air exposure; the spectrum of an as-grown film (black) acquired in situ is also reported as a comparison. The curves are vertically offset for better visibility. (b) Cu $2p_{3/2}$ region of the amorphous CuZr thin film after air exposure: the spectrum shows a single peak associated with metallic Cu. (c) Cu $2p_{3/2}$ region of the polycrystalline CuZr thin film after air exposure: the spectrum shows three different components associated with metallic Cu, CuO and $Cu(OH)_2$.*

thin film. Moreover, the characteristic sharp peaks of the sapphire substrate are clearly visible above the background intensity of the amorphous CuZr spectrum, whereas only the most intense peak of the sapphire substrate at approximately 415 cm^{-1} is still detected in the case of polycrystalline CuZr. This strong difference in attenuation is consistent with the observed opaque nature of the polycrystalline layer reported in Figure 3.1 (b).

The substantial differences in the surface oxidation behavior of air-exposed amorphous and polycrystalline CuZr observed in XPS and Raman spectroscopy allow insights into the structure-dependent oxidation mechanism. As expected for a binary alloy with very different oxygen affinities such as CuZr [21, 46], both systems are characterized by a strong preferential oxidation and surface enrichment of Zr upon air exposure. However, the structure of the thin film plays a major role. In amorphous CuZr, a ZrO_2 layer fully passivates the surface and prevents Cu underneath from oxidizing. Based on previous reports for air-exposed [47] and thermally oxidized [21] amorphous CuZr films as well as CuZr-based alloys [19], the ZrO_2 layer is expected to be closed and amorphous. The lack of peaks

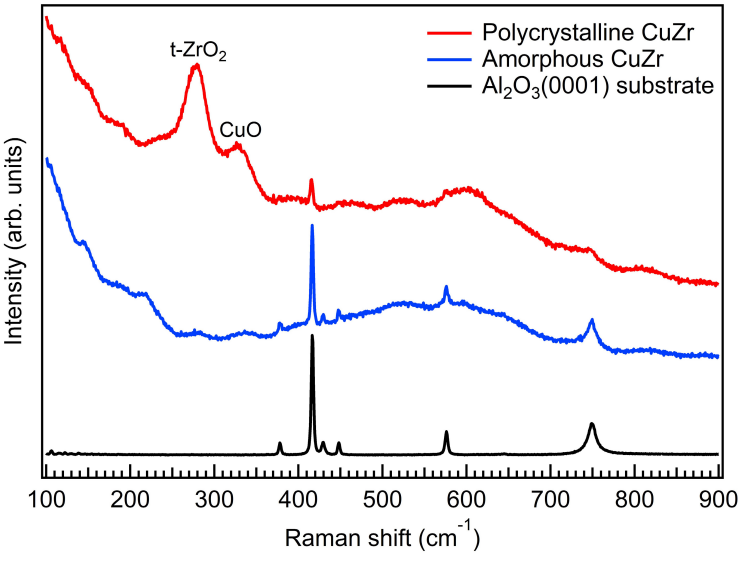

Figure 3.4 *Ex situ Raman spectroscopy measurements of polycrystalline (red curve) and amorphous (blue curve) CuZr thin films together with a bare Al_2O_3(0001) substrate (black curve), performed with an excitation wavelength of λ=532 nm. The curves are vertically offset for better visibility. The spectrum of polycrystalline CuZr is characterized by two broad peaks at 277 cm^{-1} and 330 cm^{-1}, not detected in amorphous CuZr, ascribed to t-ZrO_2 and CuO. The sharp peaks of the Al_2O_3(0001) substrate are still clearly visible above the background in amorphous CuZr, which indicates an overall weak optical absorption of the film around the pump wavelength.*

in the Raman spectrum of oxidized amorphous CuZr corroborates this conclusion [48]. The improved oxidation resistance is attributed to the absence of grain boundaries, defined structural defects and energetically favored interstitial sites that promote O_2 dissolution and diffusion within the film [19–21, 49]. Assuming a flat, homogeneous overlayer of amorphous ZrO_2 on crystalline Cu [50], we estimate the thickness of the oxide to be approximately 2.5–3.0 nm.

In polycrystalline CuZr, on the other hand, ZrO_2 is expected to be at least partially crystalline, based on previous findings for thermally oxidized crystalline CuZr [21]. This expectation is confirmed by the observation of peaks ascribed to t-ZrO_2 and CuO in the Raman spectrum. The very large FWHM of these peaks, as compared to the sapphire substrate, indicates the formation of defective oxide crystallites with relatively small grain size, which is also suggested by the lack of corresponding oxide peaks in GI-XRD. The formation of ZrO_2 with a tetragonal structure at RT, instead of the more stable monoclinic one, has already been observed in CuZr thin films for ZrO_2 nanocrystals below a critical size of 30 nm [47]. The rough, polycrystalline CuZr layer thus favors the formation of crystalline oxides and inhibits the formation of a closed amorphous ZrO_2 passivating layer. As

a result, grain boundaries and other structural defects are present, which serve as a pathway for O_2 diffusion and act as reactive points. Consequently, Cu is partially oxidized upon air exposure, resulting in an estimated composition of 50% Cu^0, 17% CuO and 33% $Cu(OH)_2$ measured in XPS spectra. The presence of a fraction of Cu_2O in the peak attributed to Cu metal cannot be excluded due to the close overlap of the respective XPS peaks. For Zr, only a small fraction of 5% remains metallic.

The marked difference in the visible optical absorption suggests that the structure might also play a key role in the conductivity of the CuZr thin films. Therefore, we investigate the charge transport properties from RT down to 4.2 K (liquid He) in a four-probe van der Pauw configuration [51]. Figure 3.5 shows the conductivity of polycrystalline (a) and amorphous (b) CuZr thin films as a function of temperature. The conductivity in polycrystalline CuZr is approximately 6.0 $m\Omega^{-1}cm^{-1}$ at RT and does not show a clear temperature dependence. Variations in the order of 0.5% are visible and can be ascribed to small modifications in the probe contacts with cooling. In stark contrast, the conductivity of amorphous CuZr is significantly lower, approximately 4.8×10^{-2} $m\Omega^{-1}cm^{-1}$ at RT, and decreases with decreasing temperature following an inverse exponential law.

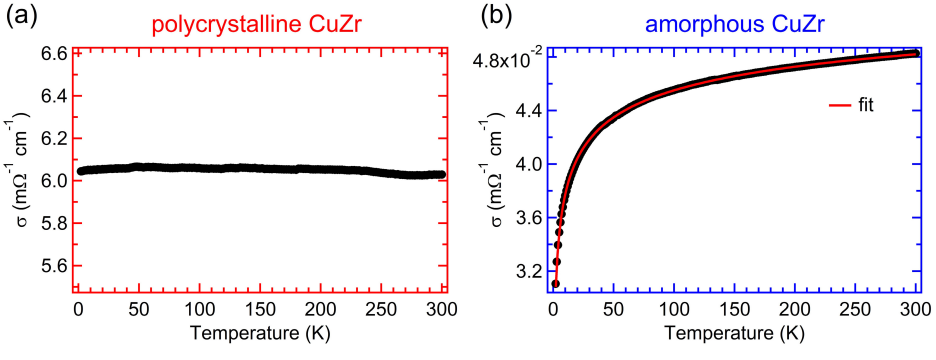

Figure 3.5 *Conductivity as a function of temperature for polycrystalline (a) and amorphous (b) CuZr thin films measured in a four-probe van der Pauw configuration. The conductivity in polycrystalline CuZr is independent of temperature while in amorphous CuZr it follows an inverse-exponential law as a function of temperature. The red solid curve in (b) is a fit to Mott's variable range hopping 3D model, which is in excellent agreement with the data.*

These results clearly indicate that the charge transport follows entirely different mechanisms in amorphous CuZr compared to its polycrystalline counterpart. In general, the conductivity in polycrystalline metallic thin films strongly deviates from the corresponding single-crystalline material and is reduced by point defects, external surfaces and in particular grain boundaries, which are found to be the dominant factor in the thin-film regime [52–54]. The conductivity in polycrystalline CuZr does not show a clear temperature dependence and is approximately two orders of magnitude lower than the value obtained for pure Cu thin films of

comparable thickness [55]. This indicates that the characteristic network of grain boundaries strongly reduces the electron mean free path and dominates the transport properties of the film, which behaves like a defective metal. The temperature-dependent resistivity change of the pure metal thus contributes too little to the overall resistivity to be clearly discernible in the measured temperature range. Similarly, disorder is expected to play a key role in amorphous CuZr, since it increases the electron scattering and reduces the electron mean free path. It is worth noting that the conductivity value at RT in amorphous CuZr is also considerably lower than values reported previously for CuZr [27], and Cu-based [56, 57] as well as other amorphous alloys films [58]. This discrepancy might be attributed to size effects based on the film thickness (≈20 nm), which are expected to increase the total resistivity [59].

To understand the temperature-dependence of the conductivity in amorphous CuZr we consider the charge transport mechanism in highly disordered systems, as described in detail by Mott [60]. The conductivity σ in amorphous materials is expected to follow the expression:

$$\sigma(T) = \sigma_0 exp\left(-\frac{T_0}{T}\right)^{\alpha} \tag{3.1}$$

where α is a characteristic exponent that assumes the value 1/3 or 1/4 in a two-dimensional and three-dimensional system, respectively. According to this model, known as Mott's variable range hopping conductivity, the theory of conductivity for doped semiconductors can also be applied to amorphous solids. In particular, the absence of long-range order induces a strong localization of the electronic states at individual atomic sites, with no electronic band structure formed in k-space. Similar to conduction in a semiconductor, the charge transport in an amorphous solid is dominated by a thermally activated hopping of electrons between localized states with energies concentrated in a narrow band near the Fermi level [60]. The conductivity is thus strongly dependent on temperature and shows a universal behavior with $\sigma_0 \propto exp(-T_0/T)^{\alpha}$. The red solid curve in Figure 3.5 (b) is a fit to Mott's variable range hopping model with α=1/4 (3D), which is found to be in excellent agreement with the experimental data over the entire temperature range (4.2–300 K). This result indicates that the electrons are indeed strongly localized in amorphous CuZr. The observation of three-dimensional hopping conduction indicates that the film thickness (≈20 nm) is significantly larger than the average hopping length, which defines the natural length scale of the process and corresponds to the average separation between available sites [61]. Since the model employed to interpret the transport properties does not provide information about the effective band gap, we derive this property from optical reflectivity measurements (see Appendix for details). Based on a simple model with a single Lorentzian oscillator, the band gap of amorphous CuZr is estimated at 1.0±0.1 eV, which is in the same range as the gaps of several materials that are heavily used in semiconductor technology.

In addition to the scientific interest in the observed changes in the optical, electronic, and surface chemical properties of CuZr with structural disorder, the

additional flexibility of the alloy film with respect to its transparency, corrosion resistance and reactivity, as well as its conductivity and transport mechanism provides an obvious link to a variety of applications. Tuning these properties while maintaining the (metal-based) composition of the layer is attractive in numerous contexts, including metal-based transparent coatings, catalysts with optimized electronic structure, customized corrosion-resistant coatings, and structures with tailored conductivity in the semiconductor industry.

3.3 CONCLUSIONS

In summary, our results demonstrate that the level of structural disorder in alloys is tunable and can induce drastic changes in the electronic, chemical, and optical properties of materials. In a direct comparison of amorphous and crystalline layers grown using PLD, we observe mechanistic differences in oxidation resistance, electronic transport, and optical transparency. The properties of the polycrystalline CuZr layers are dominated by their (defective) crystalline nature including grain boundaries, whereas the disordered nature of amorphous CuZr results in superior corrosion resistance and semiconductor-like electronic and optical properties. Our results establish tuning structural disorder in materials as a new route towards customizing functional materials to their application. This approach provides access to new applications for established materials and could loosen rigid constraints on composition in materials design, thus paving the way to the increased use of sustainable materials.

3.4 METHODS

3.4.1 SAMPLE PREPARATION

CuZr thin films were deposited onto 5×5 mm^2 $Al_2O_3(0001)$ substrates (Siegert Wafer GmbH) via pulsed laser deposition using a KrF excimer laser (λ=248 nm, 20 ns pulse duration) with a typical energy density of 4.5 J/cm^2 and laser repetition rate of 10 Hz. The substrates were cleaned prior to deposition with sequential ultrasonic bath of acetone and isopropanol. A 99.95% pure CuZr (50-50 at.%) target (Alineason Materials Technology GmbH) was used for the deposition process. The base pressure of the system was better than 5.0×10^{-10} mbar. The room temperature depositions were performed in 1.0×10^{-1} mbar Ar (purity 6.0) background pressure. The high-temperature depositions were performed in ultra-high vacuum: an infrared laser heater (λ=980 nm) was used to heat the substrates while the temperature was monitored with a pyrometer. The thickness of the thin films was approximately 20 nm, measured with an atomic force microscope. The composition of the deposited thin films was inferred by means of energy-dispersive x-ray spectroscopy (EDX) using a FEI Verios 460 SEM-EDX system equipped with a Schottky field electron gun and an Oxford Xmax 80 detector. The measured composition was found to be CuZr:44–56±1 at.% for room temperature depositions and CuZr:43–57±1 at.% for high-temperature depositions (T≈500°C).

The difference between film and target composition, i.e. the slight enrichment in total Zr content of the film, can be ascribed to resputtering effects typical of metals and alloys deposited with pulsed laser deposition [62, 63].

3.4.2 X-RAY DIFFRACTION

The structural properties of CuZr thin films were investigated *ex situ* by means of x-ray diffraction measurements in grazing-incidence configuration to minimize the contribution of the substrate. The GI-XRD investigation was performed using a Bruker D8 QUEST diffractometer system equipped with an Incoatec IμS 3.0 CuKα x-ray source (λ=1.5406 Å) and a PHOTON II Charge-integrating Pixel Array Detector (CPAD). Outliers corresponding to isolated saturated pixels of the detector have been removed in Figure 3.1 (a). The raw data are shown in Figure 3.6 of the Appendix.

3.4.3 ATOMIC FORCE MICROSCOPY

AFM measurements were performed using a Bruker Dimension Icon system operated in tapping mode. The measurements were carried out inside a soundproof chamber on a vibration isolation table. The images were processed and analysed using Gwyddion software.

3.4.4 X-RAY PHOTOELECTRON SPECTROSCOPY

XPS measurements were performed in a UHV setup (base pressure better than 1.0×10^{-9} mbar) equipped with a Scienta Omicron R4000 HiPP-3 analyser (swift acceleration mode, 1 mm entrance slit) and a monochromatic Al-Kα x-ray source (1486.6 eV). The CuZr thin films were first investigated *in situ* to infer the chemical composition of the surface: the samples were transferred from the PLD growth chamber to the XPS analysis chamber via an UHV transfer system to prevent contamination due to air exposure. The *ex situ* measurements (i.e. after air exposure) were performed on samples kept in the same ambient conditions for approximately two weeks. Survey spectra were recorded at a pass energy (PE) of 500 eV, while detailed spectra were recorded at PE=100 eV. The spectra were processed and analysed using KolXPD software (Kolibrik).

3.4.5 OPTICAL SPECTROSCOPY

A WITec alpha300 confocal Raman microscope was used to perform Raman spectroscopy measurements *ex situ* on CuZr thin films. The samples were mounted on a capacitive controlled piezo-stage with 3 nm lateral positioning accuracy. A continuous laser (λ=532 nm) was used as excitation wavelength and focused on the sample by a Zeiss EC Epiplan-Neofluar 100x objective (NA=0.9). The scattered light was collected by the same objective and detected with a fibre-coupled WITec UHTS 300 spectrometer (blaze wavelength 500 nm and 600 g/mm grating) and an Andor EMCCD. Fourier transform infrared spectroscopy was used to determine the

reflectivity of the samples over the energy range from 4 meV to 2.7 eV using a previously reported combination of sources, beam-splitters and detectors [64].

3.4.6 TRANSPORT MEASUREMENTS

Resistance measurements were carried out in the temperature range 4.2–300 K in a Physical Properties Measurement System/Dynacool (Quantum Design) using the resistivity option. Current and voltage contacts were attached to the corners of the samples by silver paint. Resistance data were taken in two van der Pauw configurations, after which the conductivity $\sigma(T)$ was evaluated by the van der Pauw relation [51]. The excitation current was 1 μA.

REFERENCES

[1] C. J. Byrne and M. Eldrup. “Bulk Metallic Glasses”. In: *Science* 321 (2008), pp. 502–503. DOI: 10.1126/science.1158864.

[2] W. H. Wang. “Bulk Metallic Glasses with Functional Physical Properties”. In: *Advanced Materials* 21 (2009), pp. 4524–4544. DOI: 10.1002/adma.200901053.

[3] A. Greer. “Metallic Glasses”. In: *Physical Metallurgy (Fifth Edition)*. Ed. by D. E. Laughlin and K. Hono. Fifth Edition. Oxford: Elsevier, 2014, pp. 305–385. ISBN: 978-0-444-53770-6. DOI: 10.1016/B978-0-444-53770-6.00004-6.

[4] Q. Halim, N. A. N. Mohamed, M. R. M. Rejab, W. N. W. A. Naim, and Q. Ma. “Metallic glass properties, processing method and development perspective: a review”. In: *International Journal of Advanced Manufacturing Technology* 112 (2021), pp. 1231–1258. ISSN: 14333015. DOI: 10.1007/s00170-020-06515-z.

[5] K. Asami, K. Hashimoto, T. Masumoto, and S. Shimodaira. “ESCA study of the passive film on an extremely corrosion-resistant amorphous iron alloy”. In: *Corrosion Science* 16 (1976), pp. 909–914. ISSN: 0010-938X. DOI: 10.1016/S0010-938X(76)80010-8.

[6] J. R. Scully, A. Gebert, and J. H. Payer. “Corrosion and related mechanical properties of bulk metallic glasses”. In: *Journal of Materials Research* 22 (2007), pp. 302–313. ISSN: 08842914. DOI: 10.1557/jmr.2007.0051.

[7] H. S. Chen. “Glassy metals”. In: *Reports on Progress in Physics* 43 (1980), pp. 353–432. DOI: 10.1088/0034-4885/43/4/001.

[8] J. J. Gilman. “Metallic Glasses”. In: *Science* 208 (1980), pp. 856–861. DOI: 10.1126/science.208.4446.856.

[9] M. Ishida, H. Takeda, N. Nishiyama, K. Kita, Y. Shimizu, Y. Saotome, and A. Inoue. “Wear resistivity of super-precision microgear made of Ni-based metallic glass”. In: *Materials Science and Engineering: A* 449-451 (2007), pp. 149–154. ISSN: 0921-5093. DOI: 10.1016/j.msea.2006.02.300.

[10] J. C. Barbour, F. W. Saris, M. Nastasi, and J. W. Mayer. “Amorphous Ni-Zr alloys as barriers for self-diffusion”. In: *Phys. Rev. B* 32 (2 1985), pp. 1363–1365. DOI: 10.1103/PhysRevB.32.1363.

[11] D. L. Cocke. “Heterogeneous Catalysis by Amorphous Materials”. In: *Journal of Metals* 10 (1986), pp. 70–74. ISSN: 00796786. DOI: 10.1007/BF03257931.

[12] B. R. Goldsmith, B. Peters, J. K. Johnson, B. C. Gates, and S. L. Scott. “Beyond Ordered Materials: Understanding Catalytic Sites on Amorphous Solids”. In: *ACS Catalysis* 7 (2017), pp. 7543–7557. DOI: 10.1021/acscatal.7b01767.

[13] M. M. Trexler and N. N. Thadhani. “Mechanical properties of bulk metallic glasses”. In: *Progress in Materials Science* 55 (2010), pp. 759–839. ISSN: 0079-6425. DOI: 10.1016/j.pmatsci.2010.04.002.

[14] O. Hunderi. “Optical properties of disordered and amorphous metal films”. In: *Thin Solid Films* 37 (1976), pp. 275–280. ISSN: 0040-6090. DOI: 10.1016/0040-6090(76)90194-2.

[15] Z. H. Stachurski. “On Structure and Properties of Amorphous Materials”. In: *Materials* 4 (2011), pp. 1564–1598. ISSN: 1996-1944. DOI: 10.3390/ma4091564.

[16] J. P. Chu, J. Jang, J. Huang, H. Chou, Y. Yang, J. Ye, Y. Wang, J. Lee, F. Liu, P. Liaw, Y. Chen, C. Lee, C. Li, and C. Rullyani. “Thin film metallic glasses: Unique properties and potential applications”. In: *Thin Solid Films* 520 (2012), pp. 5097–5122. ISSN: 0040-6090. DOI: 10.1016/j.tsf.2012.03.092.

[17] P. Yiu, W. Diyatmika, N. Bönninghoff, Y.-C. Lu, B.-Z. Lai, and J. P. Chu. “Thin film metallic glasses: Properties, applications and future”. In: *Journal of Applied Physics* 127 (2020), p. 030901. DOI: 10.1063/1.5122884.

[18] R. W. Johnson, A. Hultqvist, and S. F. Bent. “A brief review of atomic layer deposition: from fundamentals to applications”. In: *Materials Today* 17 (2014), pp. 236–246. ISSN: 1369-7021. DOI: 10.1016/j.mattod.2014.04.026.

[19] Y. Xu, L. Jeurgens, L. Lin, S. Ma, S. Zhu, Y. Huang, Y. Liu, J. Qiao, and Z. Wang. “Revealing the univariate effect of structural order on the oxidation of ternary alloys: Amorphous vs. crystalline Cu–Zr–Al alloys”. In: *Corrosion Science* 183 (2021), p. 109309. ISSN: 0010-938X. DOI: 10.1016/j.corsci.2021.109309.

[20] K. R. Lim, J. M. Park, S. J. Kim, E.-S. Lee, W. T. Kim, A. Gebert, J. Eckert, and D. H. Kim. “Enhancement of oxidation resistance of the supercooled liquid in Cu–Zr-based metallic glass by forming an amorphous oxide layer with high thermal stability”. In: *Corrosion Science* 66 (2013), pp. 1–4. ISSN: 0010-938X. DOI: 10.1016/j.corsci.2012.09.018.

[21] Y. Xu, L. P. Jeurgens, P. Schützendübe, S. Zhu, Y. Huang, Y. Liu, and Z. Wang. “Effect of atomic structure on preferential oxidation of alloys: amorphous versus crystalline Cu-Zr”. In: *Journal of Materials Science & Technology* 40 (2020), pp. 128–134. ISSN: 1005-0302. DOI: 10.1016/j.jmst.2019.10.001.

[22] R. C. Munoz and C. Arenas. “Size effects and charge transport in metals: Quantum theory of the resistivity of nanometric metallic structures arising from electron scattering by grain boundaries and by rough surfaces”. In: *Applied Physics Reviews* 4 (2017), p. 011102. DOI: 10.1063/1.4974032.

[23] Z.-Y. Wei, C. Shang, X.-J. Zhang, and Z.-P. Liu. “Glassy nature and glass-to-crystal transition in the binary metallic glass CuZr”. In: *Phys. Rev. B* 95 (21 2017), p. 214111. DOI: 10.1103/PhysRevB.95.214111.

[24] O. J. Kwon, Y. C. Kim, K. B. Kim, Y. K. Lee, and E. Fleury. “Formation of amorphous phase in the binary Cu-Zr alloy system”. In: *Metals and Materials International* 12 (2006), pp. 207–212. ISSN: 15989623. DOI: 10.1007/BF03027532.

[25] H. Okamoto. “Cu-Zr (Copper-Zirconium)”. In: *Journal of Phase Equilibria and Diffusion* 33 (2012), pp. 417–418. ISSN: 15477037. DOI: 10.1007/s11669-012-0077-1.

[26] M. Apreutesei, P. Steyer, L. Joly-Pottuz, A. Billard, J. Qiao, S. Cardinal, F. Sanchette, J. Pelletier, and C. Esnouf. “Microstructural, thermal and mechanical behavior of co-sputtered binary Zr–Cu thin film metallic glasses”. In: *Thin Solid Films* 561 (2014). Properties and Applications of Thin Film Metallic Glasses, pp. 53–59. ISSN: 0040-6090. DOI: 10.1016/j.tsf.2013.05.177.

[27] P. Zeman, M. Zítek, Š. Zuzjaková, and R. Čerstvý. “Amorphous Zr-Cu thin-film alloys with metallic glass behavior”. In: *Journal of Alloys and Compounds* 696 (2017), pp. 1298–1306. ISSN: 0925-8388. DOI: 10.1016/j.jallcom.2016.12.098.

[28] T. Minemura, J. J. van den Broek, and J. L. C. Daams. “Formation and thermal stability of amorphous Cu-Zr thin films deposited by coevaporation”. In: *Journal of Applied Physics* 63 (1988), pp. 4426–4430. DOI: 10.1063/1.340188.

[29] G. A. Almyras, G. M. Matenoglou, P. Komninou, C. Kosmidis, P. Patsalas, and G. A. Evangelakis. “On the deposition mechanisms and the formation of glassy CU–Zr thin films”. In: *Journal of Applied Physics* 107 (2010), p. 084313. DOI: 10.1063/1.3366715.

[30] W. L. Johnson. “Bulk glass-forming metallic alloys: Science and technology”. In: *MRS Bulletin* 24 (1999), pp. 42–56. ISSN: 02729172. DOI: 10.1557/proc-554-311.

[31] G. Yetik, A. Troglia, S. Farokhipoor, S. van Vliet, J. Momand, B. J. Kooi, R. Bliem, and J. W. Frenken. “Ultrathin, sputter-deposited, amorphous alloy films of ruthenium and molybdenum”. In: *Surface and Coatings Technology* 445 (2022), p. 128729. ISSN: 0257-8972. DOI: 10.1016/j.surfcoat.2022.128729.

[32] L. Zhong, J. Wang, H. Sheng, Z. Zhang, and S. X. Mao. “Formation of monatomic metallic glasses through ultrafast liquid quenching”. In: *Nature* 512 (2014), pp. 177–180. ISSN: 14764687. DOI: 10.1038/nature13617.

[33] W. H. Wang. “Roles of minor additions in formation and properties of bulk metallic glasses”. In: *Progress in Materials Science* 52 (2007), pp. 540–596. ISSN: 0079-6425. DOI: 10.1016/j.pmatsci.2006.07.003.

[34] B. Braeckman and D. Depla. “On the amorphous nature of sputtered thin film alloys”. In: *Acta Materialia* 109 (2016), pp. 323–329. ISSN: 1359-6454. DOI: 10.1016/j.actamat.2016.02.035.

[35] M. Ghidelli, A. Orekhov, A. L. Bassi, G. Terraneo, P. Djemia, G. Abadias, M. Nord, A. Béché, N. Gauquelin, J. Verbeeck, J.-P. Raskin, D. Schryvers, T. Pardoen, and H. Idrissi. "Novel class of nanostructured metallic glass films with superior and tunable mechanical properties". In: *Acta Materialia* 213 (2021), p. 116955. ISSN: 1359-6454. DOI: 10.1016/j.actamat.2021.116955.

[36] B. Cullity and S. Stock. *Elements of X-ray Diffraction, Third Edition*. Prentice-Hall, 2001.

[37] P. Yu, H. Bai, M. Tang, and W. Wang. "Excellent glass-forming ability in simple $Cu_{50}Zr_{50}$-based alloys". In: *Journal of Non-Crystalline Solids* 351 (2005), pp. 1328–1332. ISSN: 0022-3093. DOI: 10.1016/j.jnoncrysol.2005.03.012.

[38] D. Lee, B. Zhao, E. Perim, H. Zhang, P. Gong, Y. Gao, Y. Liu, C. Toher, S. Curtarolo, J. Schroers, and J. J. Vlassak. "Crystallization behavior upon heating and cooling in $Cu_{50}Zr_{50}$ metallic glass thin films". In: *Acta Materialia* 121 (2016), pp. 68–77. ISSN: 1359-6454. DOI: 10.1016/j.actamat.2016.08.076.

[39] A. Rauf, C. Guo, Y. Fang, Z. Yu, B. Sun, and T. Feng. "Binary Cu-Zr thin film metallic glasses with tunable nanoscale structures and properties". In: *Journal of Non-Crystalline Solids* 498 (2018), pp. 95–102. ISSN: 0022-3093. DOI: 10.1016/j.jnoncrysol.2018.06.015.

[40] M. C. Biesinger. "Advanced analysis of copper X-ray photoelectron spectra". In: *Surface and Interface Analysis* 49 (2017), pp. 1325–1334. DOI: 10.1002/sia.6239.

[41] S. Saikova, S. Vorobyev, M. Likhatski, A. Romanchenko, S. Erenburg, S. Trubina, and Y. Mikhlin. "X-ray photoelectron, Cu L_3MM Auger and X-ray absorption spectroscopic studies of Cu nanoparticles produced in aqueous solutions: The effect of sample preparation techniques". In: *Applied Surface Science* 258 (2012), pp. 8214–8221. ISSN: 0169-4332. DOI: 10.1016/j.apsusc.2012.05.024.

[42] S. W. Gaarenstroom and N. Winograd. "Initial and final state effects in the ESCA spectra of cadmium and silver oxides". In: *The Journal of Chemical Physics* 67 (1977), pp. 3500–3506. DOI: 10.1063/1.435347.

[43] I. Bespalov, M. Datler, S. Buhr, W. Drachsel, G. Rupprechter, and Y. Suchorski. "Initial stages of oxide formation on the Zr surface at low oxygen pressure: An in situ FIM and XPS study". In: *Ultramicroscopy* 159 (2015), pp. 147–151. ISSN: 0304-3991. DOI: 10.1016/j.ultramic.2015.02.016.

[44] S. N. Basahel, M. Mokhtar, E. H. Alsharaeh, T. T. Ali, H. A. Mahmoud, and K. Narasimharao. "Physico-Chemical and Catalytic Properties of Mesoporous CuO-ZrO_2 Catalysts". In: *Catalysts* 6 (2016), p. 57. ISSN: 2073-4344. DOI: 10.3390/catal6040057.

[45] J. F. Xu, W. Ji, Z. X. Shen, W. S. Li, S. H. Tang, X. R. Ye, D. Z. Jia, and X. Q. Xin. "Raman spectra of CuO nanocrystals". In: *Journal of Raman Spectroscopy* 30 (1999), pp. 413–415. DOI: 10.1002/(SICI)1097-4555(199905)30:5<413::AID-JRS387>3.0.CO;2-N.

[46] X. Li, J. Wu, and Y. Pan. "Preparation of nanostructured Cu/Zr metal mixed oxides via self-sustained oxidation of a CuZr binary amorphous alloy". In: *Journal of Materials Science & Technology* 35 (2019), pp. 1601–1606. ISSN: 1005-0302. DOI: 10.1016/j.jmst.2019.03.020.

[47] Y. Xu, X. Liu, L. Gu, J. Wang, P. Schützendübe, Y. Huang, Y. Liu, and Z. Wang. "Natural oxidation of amorphous Cu_xZr_{1-x} alloys". In: *Applied Surface Science* 457 (2018), pp. 396–402. ISSN: 0169-4332. DOI: 10.1016/j.apsusc.2018.06.130.

[48] D. S. S. Padovini, D. S. L. Pontes, C. J. Dalmaschio, F. M. Pontes, and E. Longo. "Facile synthesis and characterization of ZrO_2 nanoparticles prepared by the AOP/hydrothermal route". In: *RSC Adv.* 4 (73 2014), pp. 38484–38490. DOI: 10.1039/C4RA04861J.

[49] M. Kotrlová, P. Zeman, Š. Zuzjaková, and M. Zítek. "On crystallization and oxidation behavior of $Zr_{54}Cu_{46}$ and $Zr_{27}Hf_{27}Cu_{46}$ thin-film metallic glasses compared to a crystalline $Zr_{54}Cu_{46}$ thin-film alloy". In: *Journal of Non-Crystalline Solids* 500 (2018), pp. 475–481. ISSN: 0022-3093. DOI: 10.1016/j.jnoncrysol.2018.09.004.

[50] A. Jablonski and J. Zemek. "Overlayer thickness determination by XPS using the multiline approach". In: *Surface and Interface Analysis* 41.3 (2009), pp. 193–204. DOI: 10.1002/sia.3005.

[51] L. J. van der Pauw. "A method of measuring specific resisitivity and Hall effect of discs of arbitrary shape". In: *Philips Research Reports* 13 (1958), pp. 1–9. ISSN: 00023027.

[52] A. F. Mayadas and M. Shatzkes. "Electrical-Resistivity Model for Polycrystalline Films: the Case of Arbitrary Reflection at External Surfaces". In: *Phys. Rev. B* 1 (4 1970), pp. 1382–1389. DOI: 10.1103/PhysRevB.1.1382.

[53] G. Reiss, J. Vancea, and H. Hoffmann. "Grain-Boundary Resistance in Polycrystalline Metals". In: *Phys. Rev. Lett.* 56 (19 1986), pp. 2100–2103. DOI: 10.1103/PhysRevLett.56.2100.

[54] L. Moraga, C. Arenas, R. Henriquez, S. Bravo, and B. Solis. "The electrical conductivity of polycrystalline metallic films". In: *Physica B: Condensed Matter* 499 (2016), pp. 17–23. ISSN: 0921-4526. DOI: 10.1016/j.physb.2016.07.001.

[55] F. Cemin, D. Lundin, D. Cammilleri, T. Maroutian, P. Lecoeur, and T. Minea. "Low electrical resistivity in thin and ultrathin copper layers grown by high power impulse magnetron sputtering". In: *Journal of Vacuum Science & Technology A* 34 (2016), p. 051506. DOI: 10.1116/1.4959555.

[56] Y. K. Kuo, K. M. Sivakumar, C. A. Su, C. N. Ku, S. T. Lin, A. B. Kaiser, J. B. Qiang, Q. Wang, and C. Dong. "Measurement of low-temperature transport properties of Cu-based Cu-Zr-Ti bulk metallic glass". In: *Phys. Rev. B* 74 (1 2006), p. 014208. DOI: 10.1103/PhysRevB.74.014208.

[57] H. Turnow, H. Wendrock, S. Menzel, T. Gemming, and J. Eckert. "Structure and properties of sputter deposited crystalline and amorphous Cu–Ti films". In: *Thin Solid Films* 598 (2016), pp. 184–188. ISSN: 0040-6090. DOI: 10.1016/j.tsf.2015.10.081.

[58] D. You, H. Zhang, S. Ganorkar, T. Kim, J. Schroers, J. J. Vlassak, and D. Lee. "Electrical resistivity as a descriptor for classification of amorphous versus crystalline phases of alloys". In: *Acta Materialia* 231 (2022), p. 117861. ISSN: 1359-6454. DOI: 10.1016/j.actamat.2022.117861.

[59] G. Palasantzas, Y.-P. Zhao, G.-C. Wang, T.-M. Lu, J. Barnas, and J. T. M. De Hosson. "Electrical conductivity and thin-film growth dynamics". In: *Phys. Rev. B* 61 (16 2000), pp. 11109–11117. DOI: 10.1103/PhysRevB.61.11109.

[60] N. F. Mott. "Conduction in Non-crystalline Materials". In: *Philosophical Magazine* 19 (1969), pp. 835–852.

[61] B. I. Shklovskii and A. L. Efros. *Electronic Properties of Doped Semiconductors*. 1st ed. Springer Berlin, Heidelberg, 1984. ISBN: 9783662024058. DOI: 10.1007/978-3-662-02403-4.

[62] S. Fähler, K. Sturm, and H.-U. Krebs. "Resputtering during the growth of pulsed-laser-deposited metallic films in vacuum and in an ambient gas". In: *Applied Physics Letters* 75.24 (1999), pp. 3766–3768. ISSN: 0003-6951. DOI: 10.1063/1.125449.

[63] K. Sturm, S. Fähler, and H.-U. Krebs. "Pulsed laser deposition of metals in low pressure inert gas". In: *Applied Surface Science* 154-155 (2000), pp. 462–466. ISSN: 0169-4332. DOI: 10.1016/S0169-4332(99)00407-9.

[64] A. Tytarenko. "Exploring instabilities of bad metals with optical spectroscopy". PhD thesis. University of Amsterdam, 2017. URL: https://hdl.handle.net/11245.1/dda680a2-a2a8-4987-9957-eae125605545.

APPENDIX

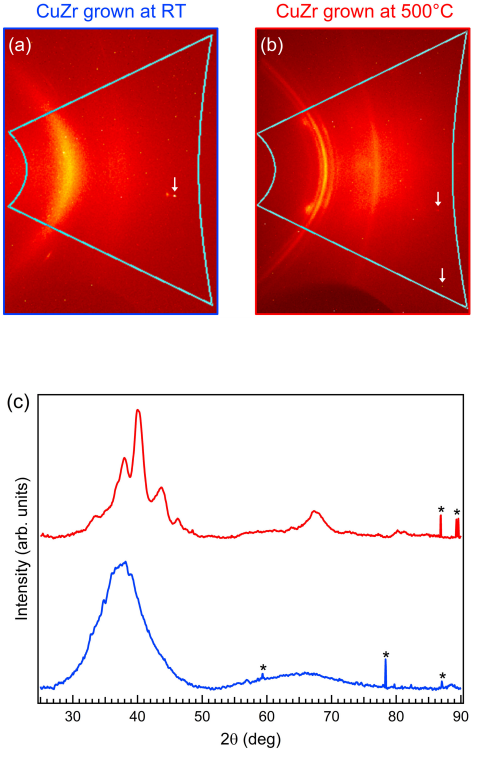

Figure 3.6 *2D diffraction patterns corresponding to CuZr thin films grown at RT (a) and at 500 °C (b). The integration of the area marked with a light blue line allowed to extract the diffractograms reported in (c). The sharp spikes marked with an asterisk in (c) are artefacts of the measurement ascribed to saturated pixels on the 2D detector (indicated in (a) and (b) with white arrows). These artefacts have been removed in Figure 3.1.*

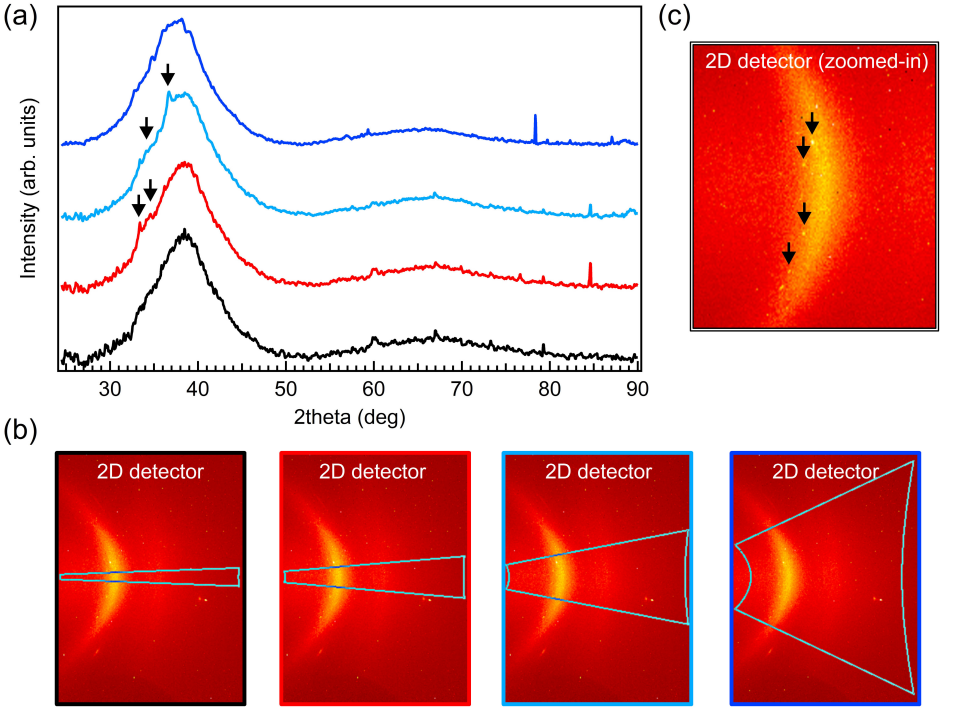

Figure 3.7 *(a) GI-XRD diffractograms of a CuZr thin film deposited at room temperature derived from a 2D diffraction pattern by integrating over different ranges of in-plane angles, indicated in (b). The sharp features marked with black arrows in (a) are ascribed to diffraction from individual crystalline droplets from melt ejection. The corresponding diffraction spots are marked with black arrows in the zoomed-in image of the 2D detector (c).*

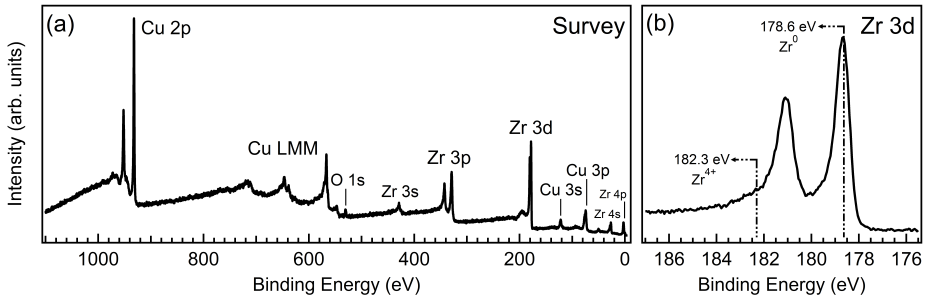

Figure 3.8 *In situ XPS investigation of an as-grown CuZr thin film. (a) XPS survey showing the presence of Cu, Zr and small traces of O. (b) Detailed measurement of the Zr 3d region: the main doublet is located at E_B=178.6 eV, indicating that Zr is mostly metallic. Small traces of Zr^{4+} around E_B=182.3 eV are visible in the tail of the Zr 3d doublet. From the measured XPS peak areas we can estimate a 5% surface contamination with oxygen. We ascribe the presence of a small amount of oxygen to the interaction of the highly reactive element Zr with water still present in the deposition and measurement vacuum chamber, despite the excellent background pressure (better than 5.0×10^{-10} mbar and 1.0×10^{-9} mbar, respectively). This is clearer by considering the as-grown XPS spectrum of the Zr 3d region shown in (b): the main Zr $3d_{5/2}$ peak is located at 178.6 eV of binding energy, in good agreement with the expected value for metallic Zr [1]. On the other hand, the presence of a small contribution from ZrO_2 species around 182.3 eV [1] is visible as a weak shoulder in the tail of the metallic Zr $3d_{3/2}$ peak. Also, the presence of small traces of sub-oxide species in the range between 179.0 eV and 182.0 eV [1] cannot be excluded. Nevertheless, the total oxygen content is very low, confirming the high purity of the as-grown CuZr thin films.*

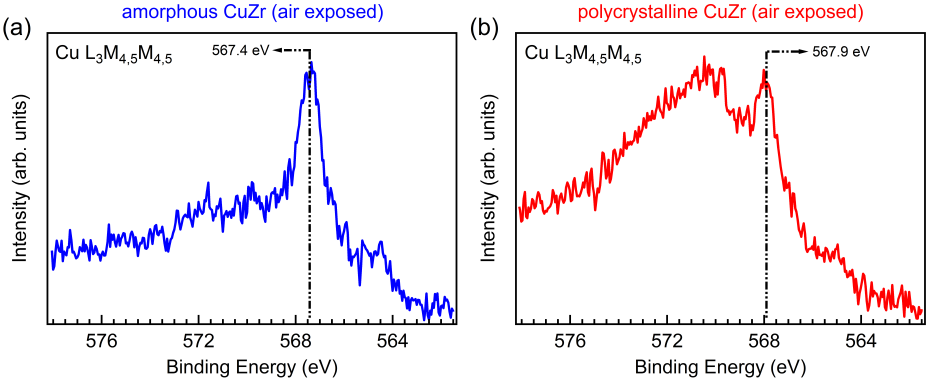

Figure 3.9 *XPS measurements of the Cu $L_3M_{4,5}M_5$ Auger region for amorphous (a) and polycrystalline (b) CuZr thin films after air exposure. The main peak position is marked with a dashed line. The calculated Auger parameter (α'=1851.3 eV) for polycrystalline CuZr is in very good agreement with the calculated value for metallic Cu [2] in amorphous CuZr. However, the higher spectral intensity around E_B=570 eV suggests the presence of peaks ascribed to CuO (expected at $E_B\approx$569.0 eV [2]) and $Cu(OH)_2$ (expected at $E_B\approx$570.4 eV [2]) in the polycrystalline CuZr film.*

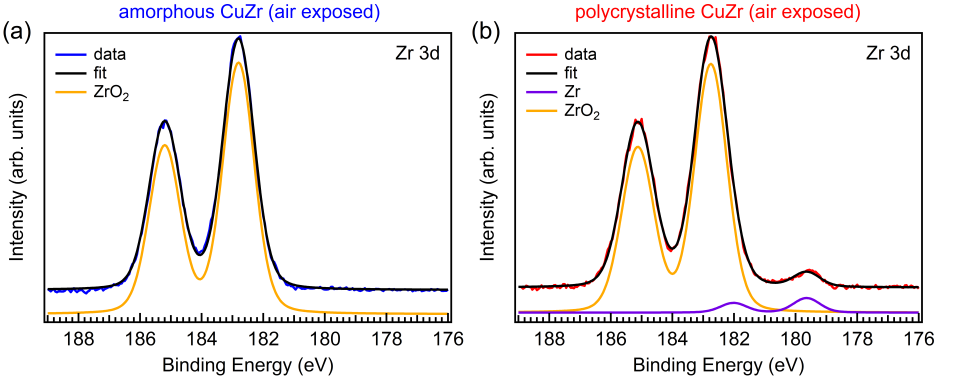

Figure 3.10 *XPS measurements of the Zr 3d region for amorphous (a) and polycrystalline (b) CuZr thin films after air exposure. Both spectra display a main peak centered at E_B=182.8 eV ascribed to ZrO_2. The polycrystalline film shows the presence of an additional, low-intensity peak centered at E_B=179.5 eV and ascribed to metallic Zr.*

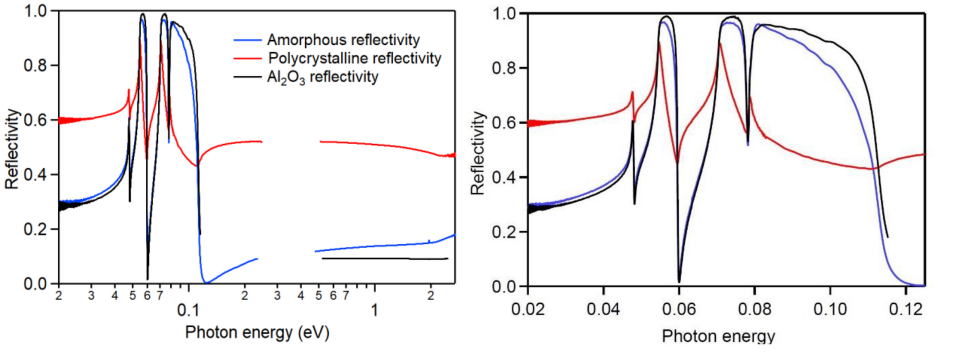

Figure 3.11 *Full (left) and detailed (right) reflectivity data of amorphous (blue) and polycrystalline (red) layers of CuZr as well as an Al_2O_3(0001) reference sample (black) measured using FTIR.*

Optical measurement of the band gap of amorphous CuZr

We determined the reflectivity of our thin films with Fourier transform infrared spectroscopy. Three experiments were performed that enabled us to determine the optical response of the polycrystalline and amorphous film. In the first experiment we determine the reflectivity of the bare, sapphire substrate, see Figure 3.11. Since the backside of the Al_2O_3 (0001) substrate is unpolished, Fabry-Perot interference does not play a role in this experiment. We determine the reflectivity over the energy range from 4 meV to 2.7 eV, using a combination of sources, beam-splitters and detectors [3]. We first determine the reflected intensity from the substrate and subsequently use evaporated gold (below 0.6 eV) or silver (above 0.6 eV) as reference to determine the absolute reflectivity. The excellent agreement between the reflectivity determined in different energy ranges and with different reference materials indicate an error on the reflectivity between 0.1% and 0.3%.

The reflectivity of the substrate-film samples is determined in exactly the same way as the substrate. Comparing the three measurements in Figure 3.11, we see distinct difference between the bare substrate and the two substrate-film samples. Starting with the bare substrate, the reflectivity shows a series of infrared active phonon modes below 100 meV. The mode frequencies extracted from a Drude Lorentz model (see below) agree well with previously reported values [4]. Above 100 meV, the reflectivity is nearly frequency independent up to the limit of our energy range.

The reflectivity of the substrate with amorphous film is very similar to the bare substrate in the phonon energy range. The reflectivity in the NIR-VIS range of the spectrum is however significantly higher and acquires a frequency dependence. This points to an interband transition in this energy range. The reflectivity of the substrate with polycrystalline film is significantly different also in the far-infrared range. We still observe the same set of phonon modes, but they are significantly less pronounced. The NIR-VIS reflectivity is higher than both the amorphous film and substrate as could be expected from the distinctly different color one can observe with the naked eye.

To extract the optical conductivity, we model the reflectivity date using RefFit [5]. In a first step we determine a Drude–Lorentz model that reproduces the reflectivity of the bare substrate. This is used as input in a model that solves the Fresnel equations for the combined substrate plus film data. In this model, the measured reflectivity is reproduced with the previously determined substrate model and a second model for the dielectric function of the film. From this analysis we can estimate the DC conductivities for both films. We find $\sigma_{DC} \approx 5.8\ \mathrm{m\Omega^{-1}cm^{-1}}$ for the polycrystalline film and $\sigma_{DC} \approx 1.5\mathrm{x}10^{-1}\ \mathrm{m\Omega^{-1}cm^{-1}}$ for the amorphous film.

Reproducing the measured reflectivity data for the amorphous film requires a single Lorentzian-like oscillator at high energy. This allows us to make an estimate of the bandgap of the amorphous film at approximately 1.0±0.1 eV (see Table below).

Sample		Al_2O_3	PC	Amorphous
Drude	ω_p	-	4849	-
	γ_D	-	511.4	-
Lorentz 1	ω_0	84.1	1463	806.4
	f_p	30.2	12072	2857
	γ	32.2	4252	3567
Phonon 1	ω_0	47.8	-	-
	f_p	23.7	-	-
	γ	0.1	-	-
Phonon 2	ω_0	54.5	-	-
	f_p	95.0	-	-
	γ	0.2	-	-
Phonon 3	ω_0	70.6	-	-
	f_p	127.6	-	-
	γ	0.3	-	-
Phonon 4	ω_0	78.6	-	-
	f_p	35.1	-	-
	γ	0.9	-	-
ε_∞		3.44	19.3	6.24

Table 3.1 *Drude-Lorentz model mode frequencies in meV. In this table, ω_p is the plasma frequency, γ_D indicates the line broadening, ω_p is the central frequency of the Lorentz oscillator or phonon mode and f_p is the corresponding oscillator strength. The phonon modes of the Al_2O_3 (0001) substrate correspond well with previously reported literature. The final row of the table indicates the estimated ϵ_∞, which is a measure of high-energy interband transitions above our energy range.*

REFERENCES

[1] I. Bespalov, M. Datler, S. Buhr, W. Drachsel, G. Rupprechter, and Y. Suchorski. "Initial stages of oxide formation on the Zr surface at low oxygen pressure: An in situ FIM and XPS study". In: *Ultramicroscopy* 159 (2015), pp. 147–151. ISSN: 0304-3991. DOI: 10.1016/j.ultramic.2015.02.016.

[2] M. C. Biesinger. "Advanced analysis of copper X-ray photoelectron spectra". In: *Surface and Interface Analysis* 49 (2017), pp. 1325–1334. DOI: 10.1002/sia.6239.

[3] A. Tytarenko. "Exploring instabilities of bad metals with optical spectroscopy". PhD thesis. University of Amsterdam, 2017. URL: https://hdl.handle.net/11245.1/dda680a2-a2a8-4987-9957-eae125605545.

[4] Y. Liu, B. Cheng, K.-K. Wang, G.-P. Ling, J. Cai, C.-L. Song, and G.-R. Han. "Study of Raman spectra for γ-Al_2O_3 models by using first-principles method". In: *Solid State Communications* 178 (2014), pp. 16–22. ISSN: 0038-1098. DOI: 10.1016/j.ssc.2013.09.030.

[5] A. B. Kuzmenko. "Kramers–Kronig constrained variational analysis of optical spectra". In: *Review of Scientific Instruments* 76.8 (2005). ISSN: 0034-6748. DOI: 10.1063/1.1979470.

4

BRIDGING THE GAP BETWEEN HIGH-ENTROPY ALLOYS AND METALLIC GLASSES: CONTROL OVER DISORDER AND MECHANICAL PROPERTIES OF COATINGS

High-entropy alloys (HEAs) and high-entropy metallic glasses (HEMGs) represent two intensively researched classes of materials with high technological interest for applications as functional coatings with high strength, hardness, toughness, and corrosion resistance. The distinctive structural difference between single-phase crystalline solid solutions for HEAs and liquid-like disorder for HEMGs generates a seemingly insuperable contrast. In this work, we demonstrate that we can deliberately choose between crystalline or glassy properties by introducing structural disorder in HfMoNbTiZr thin films of identical composition. Using pulsed laser deposition (PLD) at different growth conditions, we reproducibly tune the structure of HfMoNbTiZr coatings from crystalline to fully amorphous. We show that the level of disorder has a profound impact on the mechanical properties of the coatings using the hardness derived from nanoindentation measurements as an example. While the hardness of polycrystalline HfMoNbTiZr layers already substantially exceeds the single-phase bulk value, the amorphous HfMoNbTiZr is even close to 30% harder, demonstrating a distinctive improvement with introducing disorder. Our findings bridge the two seemingly different concepts of HEAs and HEMGs and demonstrate that structural disorder is not a given material property. Instead, disorder can serve as a useful design parameter for customizing the properties of functional coatings.

This chapter has been submitted for publication in a modified form as: A. Troglia, C. Leriche, M. van de Poll, G. ten Brink, B. J. Kooi, B. Weber, and R. Bliem. *Bridging the gap between high-entropy alloys and metallic glasses: Control over disorder and mechanical properties of coatings* (2024).

4.1 INTRODUCTION

4.1.1 HIGH-ENTROPY ALLOYS: A BRIEF OVERVIEW

For thousands of years, alloying has been a key driving force in humankind's technological advancement [1]. Some major accomplishments in the field of metallurgy and alloy development directly affected the history of civilization. For example, one of the first alloys to be discovered was bronze, obtained by diluting copper with small quantities of tin. This finding led to the end of the Stone Age and the start of the Bronze Age, characterized by the widespread use of bronze due to its superior mechanical properties compared to stone. Similarly, the development of ferrous metallurgy and, in particular, the discovery of steel (an alloy of iron and carbon), led to the end of the Bronze Age and the birth of the Iron Age. Further improvements in the ability to precisely control the level of minor additions and impurities in iron alloys initiated the industrial revolution of the 19^{th} century.

Alloying continued to be a driving force for technology also during the 20^{th} century, with new lightweight and highly durable alloys boosting the development of several branches of industry such as aerospace engineering and telecommunication. These achievements have been possible with traditional alloying, that is, to select a small number of base elements with interesting properties and enhance them by adding small quantities of other elements. However, over the past few decades, many properties and possibilities of traditional alloying have been intensively explored: for example, almost all of the available elements have been studied as a base for simple alloys [2]. A new approach towards alloying is therefore required for a breakthrough in the field of materials development, going beyond incremental improvements. In this context, the so-called high-entropy alloys (HEAs) represent a radically novel concept, breaking with the traditional notion of alloying by working with multiple principal elements beyond the concentration of dopants [2, 3].

The commonly accepted definition of a HEA is 'an alloy consisting of five or more principal elements with an atomic concentration between 35 and 5 at.%, forming a single-phase solid solution [4]', i.e. a homogeneous mixture of atoms in one common, well-defined crystal structure. The latter represents the main discriminating factor between a true HEA and an 'ordinary' multi-component alloy, where the formation of various intermetallic phases with different crystal structures is generally favored [5]. This novel approach in materials design led to the synthesis of numerous HEAs with remarkable properties such as higher mechanical strength than the binary combinations of the constituent elements [5–8], increased ductility and toughness at cryogenic temperatures [9], and even superconductivity [10].

As can be intuitively imagined, not all mixtures of a large number of principal elements will form single-phase high-entropy alloys. In the past few years, several sets of rules with different levels of complexity have been developed in order to predict the formation and equilibrium structure of HEAs [11, 12]. Simple solid-solution formation rules for high-entropy alloys take into account three main parameters of the elements and their binary mixtures [13], that is the mixing enthalpy (ΔH_{mix}), the entropy of mixing (ΔS_{mix}), and the atomic size difference δ,

which is defined as [13]:

$$\delta = \sqrt{\sum_{i=1}^{N} c_i \left(1 - \frac{r_i}{\overline{r}}\right)^2} \tag{4.1}$$

Where N is the total number of elements, c_i is the relative atomic percentage of an element, r_i is the corresponding atomic radius and $\overline{r}$ is the average radius weighted with the concentration. The mixing enthalpy ΔH_{mix} describes the chemical affinity between the principal elements of the mixture and is defined as [13]:

$$\Delta H_{mix} = 4 \sum_{i=1, i\neq j}^{N} \Delta H_{ij} c_i c_j \tag{4.2}$$

Where ΔH_{ij} is the mixing enthalpy of the i-th and j-th element of the alloy. Finally, the last and perhaps most interesting parameter is the entropy of mixing ΔS_{mix}, or configurational entropy, which gives HEAs their peculiar name. For the ideal random mixture, it is defined following Boltzmann's equation as [13]:

$$\Delta S_{mix} = -R \sum_{i=1}^{N} c_i ln(c_i) \tag{4.3}$$

Where R is the ideal gas constant. The case of an equiatomic alloy of N elements maximizes this entropy term, which increases with every element added to the mixture:

$$\Delta S_{mix} = R ln(N) \tag{4.4}$$

A large value of ΔS_{mix} can significantly lower the corresponding Gibbs free-energy of mixing $\Delta G_{mix} = \Delta H_{mix} - T\Delta S_{mix}$ and favor the formation of solid solutions instead of intermetallic phases of a subset of the constituent elements [13]. Empirical rules developed in the literature set the conditions for the entropic effect to play a role, that is, small atomic size mismatch ($\delta <\sim 0.066$) and slightly positive or negative mixing enthalpy ($\sim -11.6 < \Delta H_{mix} < 3.2$ kJ/mol) [14]. It is clear then that high configurational entropy alone is not sufficient to stabilize solid solutions, which are the result of a more complicated interplay between order and disorder. This is confirmed by the fact that, despite tens of thousands of research publications over the past years, only ≈80 single phase (i.e.'true') HEAs have been identified and produced. The majority of complex multi-component alloys investigated is multi-phase [8].

On the other hand, large atomic size mismatch ($\delta > 0.064$) and noticeably negative enthalpy of mixing ($\Delta H_{mix} < -12.2$ kJ/mol) favor the formation of amorphous mixtures, which are called high-entropy metallic glasses (HEMGs) [14]. These materials are also considered a promising, novel class of alloys expected to merge features of both metallic glasses and high-entropy alloys, such as high strength, ductility, hardness, wear resistance, and thermal stability [15, 16]. However, the formation of an amorphous structure is in direct competition with ordered intermetallic phases. In general, the tendency of alloys to form amorphous phases is determined by their glass-forming ability (GFA), a parameter based on

empirical rules, such as significant atomic size difference, and negative enthalpy of mixing among the constituents [17]. Recent studies show that, similarly to conventional metallic glasses (MG), the GFA of HEMGs is strongly related to the chemical composition of the alloy [16]. Accordingly, common design strategies of HEMGs are careful selection of the constituent elements, and GFA enhancement with minor elements additions [15, 16]. In this context, the ability to directly compare HEAs and HEMGs without varying the composition could highlight the effects of configurational disorder on a regular lattice (HEA) versus structural disorder (HEMG), and their benefits/disadvantages for specific applications.

4.1.2 HIGH-ENTROPY ALLOY THIN FILMS

Since the first studies on high-entropy alloys [6, 7], an increasing amount of research was devoted to the synthesis of novel HEAs and investigation of their properties, particularly on bulk samples. The continuous demand for functional coatings with improved properties such as high strength, hardness, and wear resistance led to growing interest in high-entropy alloy thin films (HEATFs) [18–20]. In particular, this trend is based on the widely used assumption that they would retain the same remarkable features of their bulk counterparts. Indeed, reports on HEATFs confirm outstanding properties, such as high thermal and chemical stability at elevated temperatures, excellent strength and hardness, superior resistance to irradiation, wear, fatigue, corrosion and oxidation [18–21].

In particular, HEATFs based on refractory metals like Nb, Mo, Ta, and W have attracted considerable interest thanks to their excellent mechanical properties such as high strength and toughness, and thermal stability owing to their high melting point [22–24]. Among the vast class of refractory HEAs, HfMoNbTiZr has been selected for the present study of high-entropy alloy thin films, based on reports for HfNbTiZr-based bulk alloys, promising solid-solution strengthening, strain hardening, homogeneous deformation, and structural stability, as well as properties of general interest such as high hydrogen storage capacity and superconductivity [25–28].

Finding the ideal functional coating is well known to require more optimization than just the selection of elements, exemplified by the effects of various heat treatments on material properties [29]. The role of disorder and imperfections is also essential for the application of materials. Vacancies, grain boundaries, or surface roughness, for example, are known to strongly affect the physical, chemical, and electrical properties of polycrystalline alloys [30, 31]. Even stronger effects can be achieved by selecting materials that prefer to form metallic glasses, which have been shown to exhibit different mechanical properties, such as hardness, ductility, and deformation behavior, also as thin films [32]. In the case of high-entropy materials, the beneficial effects of disorder have led to the emergence of the class of high-entropy metallic glasses (HEMGs), which have shown excellent mechanical and electrical properties, structural stability, and resistance to annealing and irradiation [33–35]. Reports of remarkably high hardness in HEMGs [33, 36–39] are attributed to their fully disordered structure, characterized by the absence of

grain boundaries, point defects and long-range order. While HEMGs and HEAs are typically characterized by different compositions, favoring either amorphicity or crystallinity, recent work on binary alloys demonstrated that tuning thin-film growth parameters allows for the growth of crystalline or amorphous layers of the same material [40]. Deliberately introducing structural disorder via off-equilibrium layer growth eradicates the co-dependence of structure and stoichiometry, opening up new pathways to customize existing materials for new applications. Building a bridge between HEAs and their glassy counterparts will add versatility to this highly promising class of materials, for example allowing for the application of a single HEA as hard coating and as mechanically compliant film.

Here, we demonstrate that the hardness of the high-entropy alloy HfMoNbTiZr can be improved by deliberately introducing structural disorder to this material, which typically forms a single-phase crystalline structure [26, 28]. By appropriately tuning the substrate temperature during pulsed laser deposition (PLD), different levels of structural disorder are obtained, ranging from fully amorphous to polycrystalline, without variation of the average chemical composition. The resulting amorphous HfMoNbTiZr thin films exhibit a very high hardness, exceeding that of their crystalline counterpart by approximately 30%. Our results thus establish structural disorder as an effective parameter to tune the properties of high-entropy alloy thin films, merging the concepts of HEAs and HEMGs for versatile functional coatings.

4.2 METHODS

4.2.1 SAMPLE PREPARATION

HfMoNbTiZr (HEA) thin films were deposited onto 5×5 mm^2 Al_2O_3(0001) substrates (Siegert Wafer GmbH) via pulsed laser deposition (PLD) using a KrF excimer laser (λ=248 nm, 20 ns pulse duration) with a typical energy density of 10.5-11.0 J/cm^2 and laser repetition rate of 10 Hz. The substrates were cleaned prior to deposition with sequential ultrasonic baths of acetone and isopropanol. A custom-made equiatomic HfMoNbTiZr target was used for the deposition process. The target was synthetized by arc-melting using powders or pieces of high-purity Hf (99.90%), Mo (99.95%), Nb (99.99%), Ti (99.99%), and Zr (99.95%). During the fabrication process, the target was re-melted more than 10 times after turning and rotating to ensure homogeneity. The base pressure of the PLD system was better than 5.0×10^{-10} mbar. All the depositions were performed in 4.0×10^{-2} mbar Ar (purity 6.0) background pressure. An infrared laser heater (λ=980 nm) was used to heat the substrate while the temperature was monitored with a pyrometer. The thickness of the films ranged between 20 nm and 100 nm, measured with atomic force microscopy. The elemental composition of the custom-made HEA target and deposited HEA thin films was measured by means of energy-dispersive x-ray spectroscopy (EDX) using a FEI Verios 460 SEM-EDX system equipped with a Schottky field electron gun and an Oxford Xmax 80 detector. SEM images of the surface morphology were acquired using the same setup, with an electron energy

of 10 keV and beam current of 100 pA.

4.2.2 X-RAY DIFFRACTION

The structural properties of HEA thin films were investigated *ex situ* by means of x-ray diffraction measurements in grazing-incidence configuration to minimize the signal from the substrate. The GI-XRD investigation was performed using a Bruker D8 QUEST diffractometer system equipped with an Incoatec IμS 3.0 CuKα x-ray source (λ=1.5406 Å) and a PHOTON II Charge-integrating Pixel Array Detector (CPAD). The diffractograms were obtained by integrating over lines of constant 2θ angle on the 2D detector using the Bruker APEX4 software. The integration areas are highlighted in the 2D diffraction patterns by light blue lines. Additional bright, sharp diffraction peaks attributed to crystalline melt-ejected droplets during deposition [40] have been removed in Figure 4.1 for clarity (see Figure 4.5 of the Appendix for the raw data and additional information).

4.2.3 TRANSMISSION ELECTRON MICROSCOPY

A JEOL 2010 operating at 200 kV (and equipped with a LaB_6 electron source) was used to record selected area electron diffraction (SAED) patterns and bright-field TEM images with relatively small objective aperture to generate strong scattering contrast to differentiate between amorphous and (nano)crystalline structures. TEM samples were produced by depositing the HEA films directly onto 20 nm thick silicon-nitride membranes and then directly capping these films with a 10 nm amorphous Si layer. For comparison, TEM samples without capping layer were also produced and analyzed.

4.2.4 X-RAY PHOTOELECTRON SPECTROSCOPY

XPS measurements were performed in a UHV setup (base pressure below 1.0×10^{-9} mbar) equipped with a Scienta Omicron R4000 HiPP-3 analyzer (swift acceleration mode, 1 mm entrance slit) and a monochromatic Al-Kα x-ray source (1486.6 eV). The HEA thin films were investigated immediately after deposition to infer the chemical composition and overall purity of the surface: the samples were transferred from the PLD growth chamber to the XPS analysis chamber via an UHV transfer system to prevent contamination due to air exposure.

4.2.5 HARDNESS MEASUREMENTS

The hardness of the HfMoNbTiZr thin films and the bulk PLD target was determined via nanoindentation measurements performed using a Femtotools FT-I04 system equipped with a Berkovich diamond tip (width approx. 200 nm) and FT S-20000 bi-axial MEMS force sensors. The indentations were performed in 'continuous stiffness measurement' (CSM) mode [41], providing continuous results as a function of penetration depth. To minimize the contribution of the Al_2O_3(0001) substrate, films of a thickness of at least 100 nm were used and the

indenter maximum penetration depth was set to 180 nm. The hardness values were then extracted by averaging more than 30 measurements performed on different locations distanced several microns from each other. For the bulk HEA target, the maximum penetration depth was set to 1.2 μm to minimize the contribution of the much higher surface roughness.

4.3 RESULTS

To paint a comprehensive picture of HfMoNbTiZr (HEA) thin films, we connect the growth parameters to measurements of the structure, composition, topography, and hardness of the layers. The structural investigation was performed by means of grazing-incidence x-ray diffraction (GI-XRD) with a 2D detector. Figure 4.1 (a) provides an overview of the temperature-dependent diffractograms obtained from samples grown at substrate temperatures ranging from room temperature (RT) up to 900°C. The diffraction pattern of the HEA film grown at RT corresponds to the one expected from amorphous structures [40, 42, 43], exhibiting two broad and weak peaks (commonly referred to as amorphous halos) centered at approximately 37° and 63°, with a full width at half maximum (FWHM) of 5.5° and 10.5°, respectively. These peaks are also characteristic of the diffractogram of the sample grown at 700°C, although a clear narrowing is discernible (FWHM reduces to approximately 3.6° and 7.5°). The broad, low-intensity peak at 54° is ascribed to an attenuated signal stemming from the Al_2O_3 substrate, visible as weak spots at the edges of the integration area (light blue lines) in the 2D diffraction pattern. Upon increasing the temperature to 800°C, sharp additional peaks around 38°, 52° and 57° are observed, indicating the formation of crystalline ordered phases [40, 43], while the amorphous halos further narrow and shift towards higher diffraction angles. On the other hand, the diffraction pattern of the HEA film deposited at 900°C displays very different features, dominated by well-defined sharp reflections at positions of 28°, 29°, 38°, 41°, 51°, 58°, and 68°. The bright spots at well-defined angles on the 2D-detector image demonstrate a high orientational preference (Figure 4.1 (e)). Additionally, the amorphous halos are no longer observed. As a comparison, GI-XRD measurements were also performed on the HEA bulk target used for the PLD depositions (blue curve in Figure 4.1 (a)), which displays sharp reflections produced by the Debye-Scherrer rings at positions 38°, 54°, 68° and 80°, in good agreement with the expected single-phase body-centered cubic (BCC) crystal structure with a = 3.36 Å reported for HfMoNbTiZr in literature [26].

To gain further insight into the microstructural evolution at high deposition temperature without substrate-induced effects, a HEA thin film was deposited at 900°C onto a Si(100) substrate coated with a 100 nm thick amorphous Si_3N_4 film. The deposition onto an amorphous layer is expected to remove any substrate-induced orientational preference. Indeed, no clear orientational preference is observed for the HEA film deposited onto amorphous Si_3N_4 (Figure 4.6 of the Appendix). The 2D diffraction pattern is dominated by continuous diffraction rings characteristic for randomly oriented polycrystalline layers. The integrated diffractogram of the HEA film deposited onto Si_3N_4 is similar to the one on

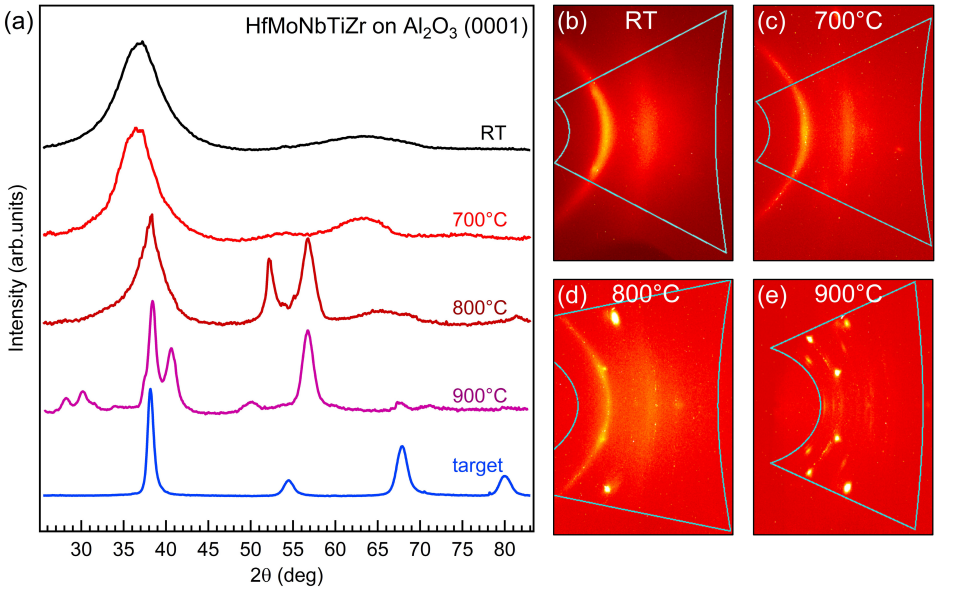

Figure 4.1 *(a) GI-XRD results of HfMoNbTiZr thin films deposited onto Al_2O_3(0001) at different substrate temperatures. The diffractograms have been normalized by height. HEA thin films deposited at RT (black curve) and at 700°C (red curve) display an amorphous structure. After increasing the temperature to 800°C (dark red curve), sharp crystalline diffraction peaks appear, and dominate the diffractogram at 900°C (purple curve). As a comparison, the GI-XRD pattern of the HEA target used for the deposition is also reported (blue curve), displaying a single-phase BCC crystal structure [26]. Sharp diffraction peaks attributed to melt-ejected droplets during deposition have been removed (see Figure 4.5 of the Appendix). (b-e) Corresponding 2D detector images: the integration of the area marked with a light-blue solid line allowed to extract the diffractograms reported in (a). The 2D diffraction patterns of (b-c) are dominated by broad continuous rings, indicating an amorphous structure. In contrast, sharp diffraction spots at well-defined angles are visible in (d-e), indicating preferential orientation of crystallites.*

Al_2O_3(0001): sharp peaks associated with crystalline phases are detected, while the amorphous halos are not observed. However, several additional peaks at lower diffraction angles and a splitting of the main peak at 38° are observed.

High-resolution structural characterization in real and reciprocal space has been performed by means of transmission electron microscopy (TEM) and diffraction of selected HEA thin films. Figure 4.2 shows representative TEM images of HEA thin films deposited at RT (a) and at 700°C (d), together with the corresponding selected area electron diffraction pattern (SAED) (b, e). No crystallites or ordered regions are discernible in the real-space images for both growth temperatures (RT and 700°C). The residual contrast in the images of Figure 4.2 (a) and Figure 4.2 (d) is attributed to local variations in density or thickness of the layers in combination

with the fact that the images were taken at relatively large defocus. The diffraction pattern of the HEA film grown at RT reported in Figure 4.2 (b) exhibits only two broad and featureless rings of homogeneous intensity (Figure 4.2 (c)), which is characteristic for an amorphous layer. Also for the HEA film grown at 700°C, broad and liquid-like diffraction features dominate the pattern, as shown in Figure 4.2 (e). However, an additional weak but narrower and discontinuous ring is visible close to the second broad one (Figure 4.2 (f)), indicating the presence of a minority phase of extremely small crystallites, estimated to be approximately 1-2 nm in diameter, embedded in the amorphous matrix.

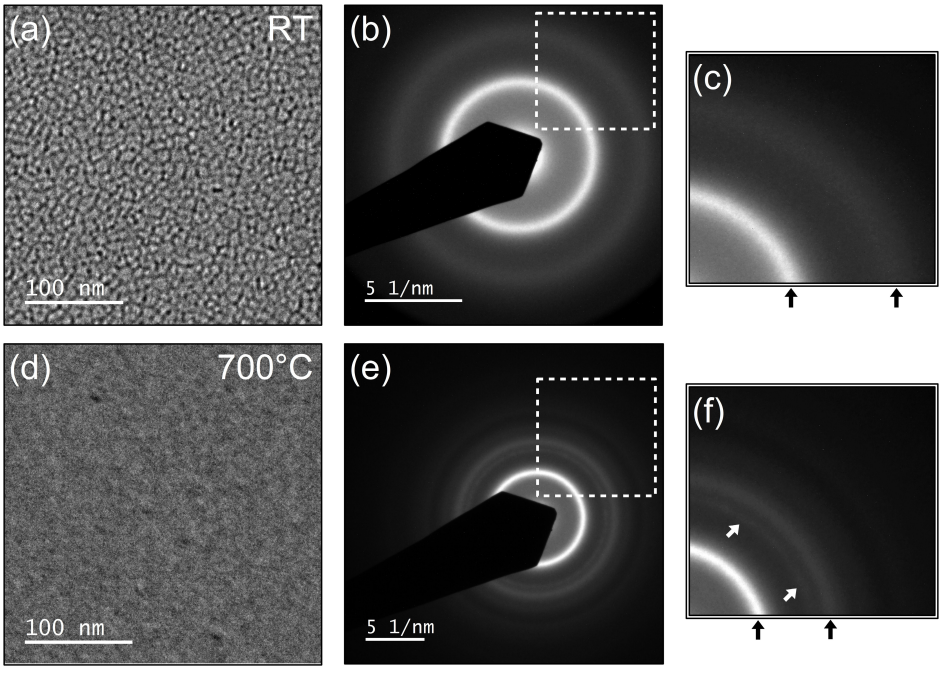

Figure 4.2 *TEM analysis of HfMoNbTiZr thin films (approximately 20 nm thick) deposited onto Si_3N_4 TEM windows and capped with an amorphous Si layer (approximately 10 nm thick). Top: TEM image of an as-grown HEA thin film deposited at room temperature (a), and corresponding SAED (b). (c) Zoomed-in panel in correspondence of the white dashed square in (b): only two broad continuous rings are visible (black arrows). Bottom: TEM image of a HEA thin film deposited at 700°C (d), and corresponding SAED pattern (e). (f) Zoomed-in panel in correspondence of the white dashed square in (e): an additional weak and discontinuous ring is visible (white arrows).*

Figure 4.3 gives further insights into the temperature-dependent structural evolution of HEA thin films. It shows TEM results focused on a region close to an extraordinarily large melt droplet (dark circular feature in Figure 4.3 (a) with a diameter of approximately 10 μm), which was ejected during PLD growth and landed at the surface with high temperature. Two distinct regions characterized by

different morphologies are clearly discernible in the TEM image of Figure 4.3 (a), with the area in the proximity of the droplet exhibiting larger contrast variations and clear signs of granularity. A zoomed-in TEM image reported in Figure 4.3 (b) corresponding to the black dashed square in panel (a) reveals a gradual transition towards increasing crystalline order as one approaches the immediate vicinity of the droplet. With decreasing distance to the droplet, the size and density of crystallites (dark and bright spots) increase up to patches of comparable brightness of approximately 100 nm in size. Smaller but clear crystallites are observed even several micrometers away from the droplet, therefore suggesting a high level of crystallinity over extended areas close to the droplet. The SAED pattern of Figure 4.3 (c) (corresponding to the area in Figure 4.3 (b)) shows several continuous and well-defined diffraction rings in the vicinity of the reciprocal distance expected for the original BCC-type crystal structure of the HEA (marked with dashed red circles), as expected for a polycrystalline film. An additional distribution of bright diffraction spots is visible around the rings, corresponding to XRD diffraction angles varying from approximately 32° to 42°. A direct comparison between GI-XRD of the HEA grown at 900°C onto Si_3N_4 and a TEM SAED line profile of Figure 4.3 (c) is reported in Figure 4.7 of the Appendix. The SAED line profile shows similarities with the GI-XRD diffractogram, with the appearance of additional diffraction peaks with respect to the original BCC-type crystal structure.

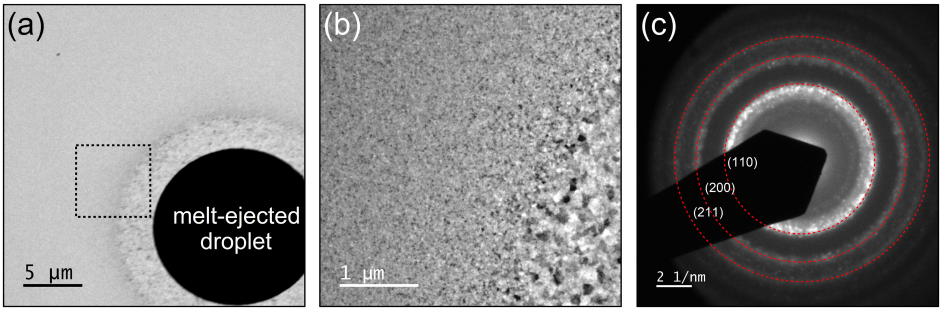

Figure 4.3 *(a) TEM analysis of a HfMoNbTiZr thin film deposited at 700°C onto Si_3N_4 TEM windows, focused on a region close to an extraordinarily large melt droplet. (b) Zoomed-in TEM image of an area close to the droplet corresponding to the dashed black square in (a): the dark and bright spots are ascribed to crystallites with a diameter of up to 100 nm. (c) SAED pattern of the region in (b) showing several continuous rings and bright diffraction spots. The expected diffraction rings for the pure BCC phase of the HEA are marked with red dashed circles.*

For the comparison of amorphous and polycrystalline layers of the same alloy, it is important to ensure that differences between the layers are not dominated by variations in stoichiometry transfer during thin-film growth. The elemental compositions of the HEA films and the bulk PLD target, as measured by energy-dispersive x-ray spectroscopy (EDX, acquired with a scanning electron microscope), are reported in Table 4.1. The target used for PLD exhibits a

close-to-equimolar chemical composition, showing a minor depletion (≈2.5 at.%) in Nb content and slight enrichment in Ti content, while the values of Hf, Mo and Zr content are compatible with the nominal ones within the EDX experimental error of ±1 at.%. On the other hand, the HEA thin films exhibit an elemental composition with clear differences as compared to the bulk target, with approximately 4 at.% enrichment in Mo and Zr, and 5 at.% depletion in Hf and Ti. The difference in elemental composition between target and thin films is ascribed to resputtering effects and scattering of the ablated material with the Ar background, which are common phenomena occurring in PLD of metallic thin films [40, 44, 45]. The HEA thin films deposited onto sapphire substrates at RT and high temperature (800°C) exhibit the same elemental composition within the experimental error of EDX. Typical scanning electron microscopy (SEM) images of the HfMoNbTiZr HEA thin films are reported in Figure 4.8 of the Appendix and show a smooth and homogeneous surface morphology. As a result of melt-ejection of droplets during laser ablation, a low density of particles with diameters ranging from tens of nanometers up to a few micrometers are deposited onto the surface.

Table 4.1 *Elemental composition (in at.% as measured by EDX) of HfMoNbTiZr thin films deposited at RT and 800°C, compared with the HEA PLD target. The thickness of both films was approximately 100 nm. The EDX experimental error is estimated at ±1 at.%.*

	Hf	Mo	Nb	Ti	Zr
nominal	20.0	20.0	20.0	20.0	20.0
HEA-target	20.5	19.3	17.5	22.4	20.3
HEA-RT	15.4	23.7	19.2	17.6	24.1
HEA-800°C	14.1	24.8	19.1	18.0	24.0

The surface composition and impurity content were investigated using XPS. Figure 4.9 of the Appendix shows an XPS survey spectrum of an as-grown HEA thin film (thickness approximately 100 nm) measured after deposition at RT, and transferred to the analysis tool in ultra-high vacuum (UHV) without air exposure. The XPS survey exhibits only the core level peaks assigned to Hf, Mo, Nb, Ti and Zr, with minor traces of oxygen. The detection of small traces of oxygen is ascribed to the interaction of highly reactive elements such as Zr and Hf with residual water in the deposition and measurement UHV chambers.

To quantify the interplay between thin film structure and mechanical performance, we investigated the hardness of the HEA thin films using nanoindentation in continuous stiffness measurement mode. Figure 4.4 shows the measured depth-dependent hardness data of fully amorphous (blue curve) and crystalline (red curve) HfMoNbTiZr HEA films on $Al_2O_3(0001)$, averaged over 30 independent indentation measurements. An initial rise in the measured hardness is observed in the first 30 nm of indentation depth, which is typically caused by an inaccuracy of the nanoscale geometry description of the diamond indenter (Berkovich tip, 3-sided pyramid) and sample (smooth flat). This leads to a varying definition of the

contact area function with penetration depth, function which forms the basis of the Oliver-Pharr model used in this measurement [41]. At indentation depths beyond 30 nm a significant difference in hardness between the amorphous and crystalline film can be identified, and this difference decreases as the indentation depth increases and the mechanical properties of the underlying $Al_2O_3(0001)$ start dominating the measurement. We therefore interpret the plateau region between approximately 30 nm and 50 nm (inset of Figure 4.4) as indicative of a *minimal* contrast in hardness. In this 30-50 nm region, the hardness of amorphous HfMoNbTiZr is H=14±1 GPa, clearly exceeding the value for polycrystalline HfMoNbTiZr of H=11±1 GPa. At this indentation depth of 30-50% of the film thickness, the absolute values of the hardness may already be influenced by the substrate. As a comparison, nanoindentation was also performed on the bulk HEA PLD target, as reported in Figure 4.10 of the Appendix. The HEA target displays a substantially lower hardness compared to the thin films, exhibiting a value of H=4.7±0.6 GPa. The variation in the reduced modulus of the thin films (Figure 4.11) and the PLD target (Figure 4.10) also reflects their different mechanical properties.

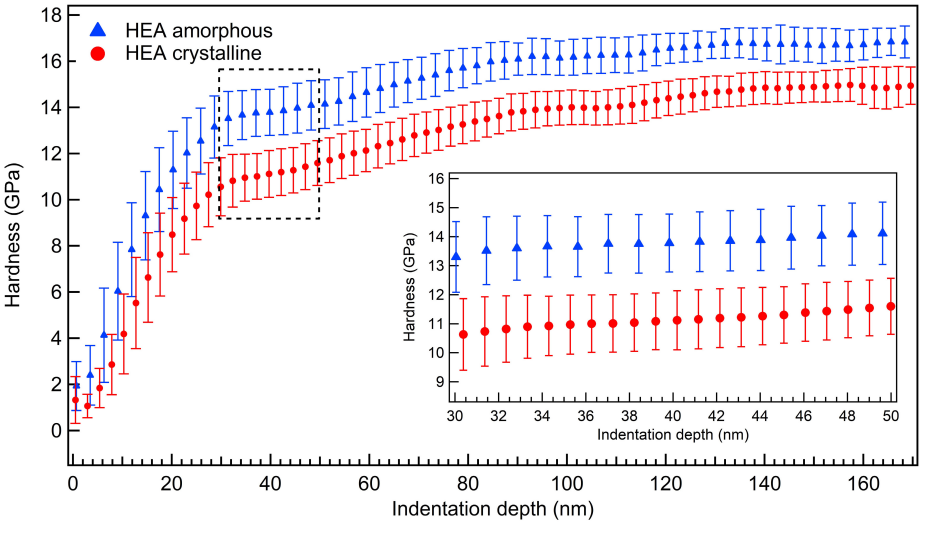

Figure 4.4 *Hardness as a function of contact depth obtained from nanoindentation measurements of amorphous (blue curve) and crystalline (red curve) HfMoNbTiZr thin films deposited onto $Al_2O_3(0001)$. The thickness of both films was approximately 100 nm. The hardness values of the HEA films were extracted from the plateau region detected between approximately 30 nm and 50 nm of indentation depth (black dashed square), reported in the inset.*

4.4 DISCUSSION

The combined results of GI-XRD, TEM and EDX measurements clearly demonstrate that structural disorder in HfMoNbTiZr thin films of constant composition (within 1 at.%) is a tunable parameter that can be controlled independently of the composition via the growth conditions in pulsed laser deposition. In agreement with previous studies on metallic glasses grown with PLD [40], the temperature of the substrate is a key parameter. At low substrate temperatures, the HEA films are amorphous. The fully disordered phase is predominant up to substrate temperatures of at least 700°C. Nanometer-sized crystallites embedded in the amorphous matrix give a subtle signal in the TEM SAED pattern at 700°C, but they do not present a signature in GI-XRD measurements, thus indicating low density, or extremely small particle sizes (in the range of 1-2 nm). The decrease in width of the amorphous halos and their shift towards higher diffraction angles with increasing temperature suggest the formation of a lower-energy amorphous structure and tunable packing density of the HEA films [46]. By increasing the substrate temperature to 800°C, the crystallites grow in size and number, and are detected also with GI-XRD. However, the presence of high background signal in the region of the amorphous halos in the 800°C diffractogram still indicates a significant level of disorder. After a further increase in growth temperature to 900°C, the system overcomes the strongly disordered state and forms crystalline grains with high orientational preference. The high thermal energy required to induce crystallization is in agreement with temperature scales characteristic of refractory metals such as niobium, tantalum, and tungsten [47]. Here, this is borne out by a remarkably high temperature (between 800°C and 900°C) required to obtain sharp diffraction features, which are a clear indication of structural order over tens of nanometers. In comparison, the crystallization temperature of the majority of metalloid-free metallic glasses is in the range of approximately 400-700°C [47–49]. High crystallization temperatures are particularly desirable in industries such as energy production and space exploration, where coatings need to sustain highly corrosive and high temperature environments [47].

The crystalline HEA thin film exhibits a more complicated diffraction pattern than the bulk polycrystalline PLD target. The diffractograms of the films deposited onto sapphire at T=800°C and 900°C show a combination of Debye-Scherrer rings, likely originating from the starting BCC-type polycrystalline phase, and several sharp diffraction spots stemming from a newly formed crystalline phase with well-defined orientation aligning with the $Al_2O_3(0001)$ substrate. The additional reflections at approximately 2θ = 29°, 41°, 51°, and 58° in Figure 4.1 (a) are attributed to a primitive cubic structure (CsCl-type) with a lattice constant of approximately a = 3.12 Å. The decrease in the magnitude of the lattice constant in comparison to the original BCC structure of the PLD target is reflected in the shift of the reflections to larger 2θ values. The symmetry reduction to a primitive cubic cell manifests itself for example in the emergence of the (100) and (111) reflections at approximately 29° and 51°, respectively. This interpretation is supported by the recent report of a primitive cubic structure of the CsCl-type in HEAs containing

refractory metals [50]. The stabilization of the CsCl-type crystal structure is ascribed to the difference in magnitude of the atomic radius between the larger Hf and Zr, on one side, and smaller Mo, Nb and Ti, on the other, which leads to a partial ordering of these two subgroups of atoms in two different crystallographic positions [50]. Therefore, in contrast to the arc-melted bulk target, which is close to the thermodynamically preferred structure, the off-equilibrium nature of PLD, with large variations in the local composition of crystalline nuclei, results in a polycrystalline structure of HfMoNbTiZr with two phases at the conditions tested here. This means that, technically, the crystalline layers of HfMoNbTiZr in this study are not single-phase solid solutions and therefore cannot be considered a 'true' HEA, in contrast to the PLD target.

The deposition of HfMoNbTiZr at 900°C onto an amorphous Si_3N_4 layer further clarifies the mechanism of crystalline growth at high temperature. The amorphous structure of Si_3N_4 prevents the formation of a strong orientational preference in the film owing to its own lack of long-range order. The 2D-detector image corresponding to HfMoNbTiZr on Si_3N_4 (Figure 4.6 (c)) shows the presence of continuous rings, whereas the one corresponding to HfMoNbTiZr on sapphire is characterized by bright spots at well-defined diffraction angles in three dimensions (Figure 4.6 (b)). In contrast to the single-phase bulk target, the diffraction pattern of the film deposited on Si_3N_4 (Figure 4.6 (a)) features multiple peak splittings. The majority of the new diffraction rings are close to the original reflection positions of the native BCC-type structure of the target, indicating the formation of various BCC intermetallic phases with similar lattice constants, estimated in the range between 3.2 Å and 3.8 Å. This is ascribed to a temperature-induced phase segregation of alloys with different compositions in the film. The peak at 29° is still present, providing further evidence for the existence of the cubic CsCl-type lattice discussed above. Interestingly, the orientational and structural preference provided by the Al_2O_3(0001) substrate also strongly reduces the observed variation in lattice constants and is thus expected to improve the homogeneity of the layer.

Moreover, the continuous temperature variation observed in TEM measurements of a region close to a micrometer-sized droplet provides insight into the temperature-dependent variations in structure. The droplet is expected to substantially increase the local temperature of the film upon landing on the surface as a hot melt and slowly cooling down. As a consequence, a gradient in thermal energy is formed in the surroundings of the droplet, with decreasing temperature as one moves away from its boundary. In this region, the temperature is expected to be locally high enough (namely ≥ 900°C) to induce the formation of large crystalline grains. The grain size decreases at larger distance from the droplet. The corresponding SAED line profile of Figure 4.7 shows the presence of several additional diffraction peaks, confirming temperature-induced formation of additional phases, most likely via phase separation. These results further clarify the growth mechanism of crystalline HfMoNbTiZr and confirm the formation of a layer with different coexisting phases at high temperature.

Nanoindentation measurements establish the important role that the thin-film structure plays in the mechanical properties of the coatings. As compared to

conventional alloys and pure metals, many HEAs have been reported to be harder thanks to solid-solution strengthening and lattice distortion effects [18, 51, 52]. This is in line with our observation that the single-phase BCC crystal structure of the HfMoNbTiZr PLD target is harder than the corresponding individual pure metals Mo, Nb, Ti, Hf, Zr [53, 54], in good agreement with previous reports on similar bulk high-entropy alloys [53, 55–58]. Polycrystalline HfMoNbTiZr thin films display a remarkably high hardness of 11 GPa, in agreement with previous reports of hard refractory HEA coatings [22, 33, 59, 60]. The hardness of the crystalline HEA coating is even surpassed by the amorphous HfMoNbTiZr thin film, with a measured hardness value of 14 GPa. While the difference between polycrystalline and amorphous layers is based on measurements with exactly the same sample geometry, substrate effects on the absolute hardness values cannot be excluded. For substrates with significantly higher hardness than the respective coating, however, the influence of the substrate on the measurement is reduced [61], supporting that HfMoNbTiZr thin films are indeed substantially harder than the bulk material. We attribute this increase in hardness to grain-size thin-film effects, as described by the Hall-Petch relationship, which states that the hardness of nanomaterials increases with decreasing grain size. Down to a critical grain size of 10-30 nm, grain boundaries act as diffusion barriers hindering the propagation of dislocations [62]. In line with this interpretation, multi-phase HEA thin films commonly display increased hardness with respect to their single-phase counterparts [19, 63, 64]. Therefore, the coexistence of different crystalline phases is expected to play an important role in effectively impeding the motion of dislocations. The increased hardness of amorphous HfMoNbTiZr (approximately 30% higher) is in agreement with the concept that metallic glasses are harder than crystalline alloys thanks to the lack of structural long-range order, which hinders the atoms' mobility and further enhances resistance to plastic deformations [33, 65–67].

Our results demonstrate that the targeted introduction of structural disorder to a (otherwise single-phase) HEA is a viable option for optimizing selected material properties. Increasing the level of disorder to first form to a polycrystalline layer with different phases and then a fully amorphous film, raises the hardness of HfMoNbTiZr to a different regime. The level of structural disorder represents an additional degree of freedom in the development of coatings, which has been effective to tune the optical, chemical and electronic properties of simple alloys without modifying their composition [40]. Here, this novel approach is extended to mechanical properties and high-entropy materials. Intentionally disordering a high-entropy alloy allows us to bridge the gap between the two seemingly different concepts of HEAs and HEMGs and customize the hardness of the material. This is for instance relevant to tune HEAs to fulfill either the requirements of mechanically stable, strong, and durable protective coatings against wear, stress, and fatigue or those of mechanical compliance of flexible electronics and wearable devices.

4.5 CONCLUSIONS

In summary, we demonstrate the growth of HfMoNbTiZr high-entropy alloy thin films with tunable level of structural disorder, ranging from fully amorphous to crystalline while maintaining an identical composition. This is achieved by appropriately varying the substrate temperature during pulsed laser deposition of the alloy. The amorphous phase exhibits remarkable thermal stability, being predominant up to a growth temperature of 700°C. For complete crystallization, a higher temperature (900°C) is required. Nanoindentation measurements highlight the intriguing mechanical properties of HfMoNbTiZr thin films, which display exceptional increase in hardness compared to the single-phase bulk PLD target. The fully disordered, amorphous HfMoNbTiZr films further exceed the hardness of the polycrystalline layers by approximately 30%. These results establish the importance of disorder as an effective parameter to tune the properties of materials without varying their composition, serving as a bridge between the different concepts of HEA and HEMG. Control over a gradual transition between order and disorder provides new versatility to materials design and has the potential to widen the scope of alloy coatings and enhance their individual performance.

REFERENCES

[1] B. Murty, J. Yeh, and S. Ranganathan. “Chapter 1 - A Brief History of Alloys and the Birth of High-Entropy Alloys”. In: *High Entropy Alloys*. Ed. by B. Murty, J. Yeh, and S. Ranganathan. Butterworth-Heinemann, 2014, pp. 1–12. ISBN: 978-0-12-800251-3. DOI: 10.1016/B978-0-12-800251-3.00001-8.

[2] D. Miracle. “High entropy alloys as a bold step forward in alloy development”. In: *Nature Communications* 10.1805 (2019). ISSN: 2041-1723. DOI: 10.1038/s41467-019-09700-1.

[3] M.-H. Tsai and J.-W. Yeh. “High-Entropy Alloys: A Critical Review”. In: *Materials Research Letters* 2.3 (2014), pp. 107–123. DOI: 10.1080/21663831.2014.912690.

[4] D. Miracle and O. Senkov. “A critical review of high entropy alloys and related concepts”. In: *Acta Materialia* 122 (2017), pp. 448–511. ISSN: 1359-6454. DOI: 10.1016/j.actamat.2016.08.081.

[5] R. Kozak, A. Sologubenko, and W. Steurer. “Single-phase high-entropy alloys – an overview”. In: *Zeitschrift für Kristallographie - Crystalline Materials* 230.1 (2015), pp. 55–68. DOI: doi:10.1515/zkri-2014-1739.

[6] J.-W. Yeh, S.-K. Chen, S.-J. Lin, J.-Y. Gan, T.-S. Chin, T.-T. Shun, C.-H. Tsau, and S.-Y. Chang. “Nanostructured High-Entropy Alloys with Multiple Principal Elements: Novel Alloy Design Concepts and Outcomes”. In: *Advanced Engineering Materials* 6.5 (2004), pp. 299–303. DOI: 10.1002/adem.200300567.

[7] B. Cantor, I. Chang, P. Knight, and A. Vincent. “Microstructural development in equiatomic multicomponent alloys”. In: *Materials Science and Engineering: A* 375-377 (2004), pp. 213–218. ISSN: 0921-5093. DOI: 10.1016/j.msea.2003.10.257.

[8] W. Steurer. “Single-phase high-entropy alloys – A critical update”. In: *Materials Characterization* 162 (2020), p. 110179. ISSN: 1044-5803. DOI: 10.1016/j.matchar.2020.110179.

[9] B. Gludovatz, A. Hohenwarter, D. Catoor, E. H. Chang, E. P. George, and R. O. Ritchie. “A fracture-resistant high-entropy alloy for cryogenic applications”. In: *Science* 345.6201 (2014), pp. 1153–1158. DOI: 10.1126/science.1254581.

[10] L. Sun and R. J. Cava. “High-entropy alloy superconductors: Status, opportunities, and challenges”. In: *Phys. Rev. Mater.* 3 (9 2019), p. 090301. DOI: 10.1103/PhysRevMaterials.3.090301.

[11] M. C. Troparevsky, J. R. Morris, P. R. C. Kent, A. R. Lupini, and G. M. Stocks. “Criteria for Predicting the Formation of Single-Phase High-Entropy Alloys”. In: *Phys. Rev. X* 5 (1 2015), p. 011041. DOI: 10.1103/PhysRevX.5.011041.

[12] O. Senkov and D. Miracle. “A new thermodynamic parameter to predict formation of solid solution or intermetallic phases in high entropy alloys”. In: *Journal of Alloys and Compounds* 658 (2016), pp. 603–607. ISSN: 0925-8388. DOI: 10.1016/j.jallcom.2015.10.279.

[13] Y. Zhang, Y. Zhou, J. Lin, G. Chen, and P. Liaw. “Solid-Solution Phase Formation Rules for Multi-component Alloys”. In: *Advanced Engineering Materials* 10.6 (2008), pp. 534–538. DOI: 10.1002/adem.200700240.

[14] S. Guo, Q. Hu, C. Ng, and C. Liu. “More than entropy in high-entropy alloys: Forming solid solutions or amorphous phase”. In: *Intermetallics* 41 (2013), pp. 96–103. ISSN: 0966-9795. DOI: 10.1016/j.intermet.2013.05.002.

[15] W. H. Wang. “High-Entropy Metallic Glasses”. In: *JOM* 66 (10 2014), pp. 2067–2077. ISSN: 1543-1851. DOI: 10.1007/s11837-014-1002-3.

[16] Y. Chen, Z.-W. Dai, and J.-Z. Jiang. “High entropy metallic glasses: Glass formation, crystallization and properties”. In: *Journal of Alloys and Compounds* 866 (2021), p. 158852. ISSN: 0925-8388. DOI: 10.1016/j.jallcom.2021.158852.

[17] S. Guo and C. Liu. “Phase stability in high entropy alloys: Formation of solid-solution phase or amorphous phase”. In: *Progress in Natural Science: Materials International* 21.6 (2011), pp. 433–446. ISSN: 1002-0071. DOI: 10.1016/S1002-0071(12)60080-X.

[18] N. I. Muhammad Nadzri, D. S. C. Halin, M. M. Al Bakri Abdullah, S. Joseph, M. A. A. Mohd Salleh, P. Vizureanu, D.-P. Burduhos-Nergis, and A. V. Sandu. “High-Entropy Alloy for Thin Film Application: A Review”. In: *Coatings* 12.12 (2022), p. 1842. ISSN: 2079-6412. DOI: 10.3390/coatings12121842.

[19] K. Cui and Y. Zhang. “High-Entropy Alloy Films”. In: *Coatings* 13.3 (2023), p. 635. ISSN: 2079-6412. DOI: 10.3390/coatings13030635.

[20] X. H. Yan, J. S. Li, W. R. Zhang, and Y. Zhang. “A brief review of high-entropy films”. In: *Materials Chemistry and Physics* 210 (2018). High-Entropy Materials, pp. 12–19. ISSN: 0254-0584. DOI: 10.1016/j.matchemphys.2017.07.078.

[21] R. K. Duchaniya, U. Pandel, and P. Rao. “Coatings based on high entropy alloys: An overview”. In: *Materials Today: Proceedings* 44 (2021), pp. 4467–4473. ISSN: 2214-7853. DOI: 10.1016/j.matpr.2020.10.720.

[22] M. A. Tunes and V. M. Vishnyakov. “Microstructural origins of the high mechanical damage tolerance of NbTaMoW refractory high-entropy alloy thin films”. In: *Materials & Design* 170 (2019), p. 107692. ISSN: 0264-1275. DOI: 10.1016/j.matdes.2019.107692.

[23] X. Feng, J. Zhang, Z. Xia, W. Fu, K. Wu, G. Liu, and J. Sun. “Stable nanocrystalline NbMoTaW high entropy alloy thin films with excellent mechanical and electrical properties”. In: *Materials Letters* 210 (2018), pp. 84–87. ISSN: 0167-577X. DOI: 10.1016/j.matlet.2017.08.129.

[24] W. Xiong, A. X. Guo, S. Zhan, C.-T. Liu, and S. C. Cao. “Refractory high-entropy alloys: A focused review of preparation methods and properties”. In: *Journal of Materials Science & Technology* 142 (2023), pp. 196–215. ISSN: 1005-0302. DOI: 10.1016/j.jmst.2022.08.046.

[25] O. Senkov, J. Scott, S. Senkova, D. Miracle, and C. Woodward. “Microstructure and room temperature properties of a high-entropy TaNbHfZrTi alloy”. In: *Journal of Alloys and Compounds* 509.20 (2011), pp. 6043–6048. ISSN: 0925-8388. DOI: 10.1016/j.jallcom.2011.02.171.

[26] N. Guo, L. Wang, L. Luo, X. Li, Y. Su, J. Guo, and H. Fu. “Microstructure and mechanical properties of refractory MoNbHfZrTi high-entropy alloy”. In: *Materials & Design* 81 (2015), pp. 87–94. ISSN: 0261-3069. DOI: 10.1016/j.matdes.2015.05.019.

[27] V. Pacheco, G. Lindwall, D. Karlsson, J. Cedervall, S. Fritze, G. Ek, P. Berastegui, M. Sahlberg, and U. Jansson. “Thermal Stability of the HfNbTiVZr High-Entropy Alloy”. In: *Inorganic Chemistry* 58.1 (2019), pp. 811–820. DOI: 10.1021/acs.inorgchem.8b02957.

[28] J. Kitagawa, K. Hoshi, Y. Kawasaki, R. Koga, Y. Mizuguchi, and T. Nishizaki. “Superconductivity and hardness of the equiatomic high-entropy alloy HfMoNbTiZr”. In: *Journal of Alloys and Compounds* 924 (2022), p. 166473. ISSN: 0925-8388. DOI: 10.1016/j.jallcom.2022.166473.

[29] R. N. Elshaer, S. El-Hadad, and A. Nofal. “Influence of heat treatment processes on microstructure evolution, tensile and tribological properties of Ti6Al4V alloy”. In: *Scientific Reports* 13 (1 2023), p. 11292. ISSN: 2045-2322. DOI: 10.1038/s41598-023-38250-2.

[30] Y. Xu, L. Jeurgens, L. Lin, S. Ma, S. Zhu, Y. Huang, Y. Liu, J. Qiao, and Z. Wang. “Revealing the univariate effect of structural order on the oxidation of ternary alloys: Amorphous vs. crystalline Cu–Zr–Al alloys”. In: *Corrosion Science* 183 (2021), p. 109309. ISSN: 0010-938X. DOI: 10.1016/j.corsci.2021.109309.

[31] R. C. Munoz and C. Arenas. “Size effects and charge transport in metals: Quantum theory of the resistivity of nanometric metallic structures arising from electron scattering by grain boundaries and by rough surfaces”. In: *Applied Physics Reviews* 4 (2017), p. 011102. DOI: 10.1063/1.4974032.

[32] J. P. Chu, J. Jang, J. Huang, H. Chou, Y. Yang, J. Ye, Y. Wang, J. Lee, F. Liu, P. Liaw, Y. Chen, C. Lee, C. Li, and C. Rullyani. “Thin film metallic glasses: Unique properties and potential applications”. In: *Thin Solid Films* 520 (2012), pp. 5097–5122. ISSN: 0040-6090. DOI: 10.1016/j.tsf.2012.03.092.

[33] S. Alvi, M. Milczarek, D. M. Jarzabek, D. Hedman, M. G. Kohan, N. Levintant-Zayonts, A. Vomiero, and F. Akhtar. “Enhanced Mechanical, Thermal and Electrical Properties of High-Entropy HfMoNbTaTiVWZr Thin Film Metallic Glass and its Nitrides”. In: *Advanced Engineering Materials* 24.9 (2022), p. 2101626. DOI: 10.1002/adem.202101626.

[34] S. Zhao, H. Wang, L. Xiao, N. Guo, D. Zhao, K. Yao, and N. Chen. “High strain rate sensitivity of hardness in quinary Ti-Zr-Hf-Cu-Ni high entropy metallic glass thin films”. In: *Physica E: Low-dimensional Systems and Nanostructures* 94 (2017), pp. 100–105. ISSN: 1386-9477. DOI: 10.1016/j.physe.2017.07.021.

[35] M. Tunes, H. Vo, J. Baldwin, T. Saleh, S. Fensin, and O. El-Atwani. “Perspectives on novel refractory amorphous high-entropy alloys in extreme environments”. In: *Applied Materials Today* 32 (2023), p. 101796. ISSN: 2352-9407. DOI: 10.1016/j.apmt.2023.101796.

[36] P. L. Wei Li and P. K. Liaw. “Microstructures and properties of high-entropy alloy films and coatings: a review”. In: *Materials Research Letters* 6.4 (2018), pp. 199–229. DOI: 10.1080/21663831.2018.1434248.

[37] N. Tüten, D. Canadinc, A. Motallebzadeh, and B. Bal. “Microstructure and tribological properties of TiTaHfNbZr high entropy alloy coatings deposited on Ti6Al4V substrates”. In: *Intermetallics* 105 (2019), pp. 99–106. ISSN: 0966-9795. DOI: 10.1016/j.intermet.2018.11.015.

[38] X. Liu, W. Cai, Y. Zhang, L. Wang, and J. Wang. “Tuning microstructure and mechanical and wear resistance of ZrNbTiMo refractory high-entropy alloy films via sputtering power”. In: *Frontiers in Materials* 10 (2023). ISSN: 2296-8016. DOI: 10.3389/fmats.2023.1145631.

[39] X. Chang, M. Zeng, K. Liu, and L. Fu. “Phase Engineering of High-Entropy Alloys”. In: *Advanced Materials* 32.14 (2020), p. 1907226. DOI: 10.1002/adma.201907226.

[40] A. Troglia, V. Vollema, S. Cassanelli, E. van Heumen, J. van de Groep, A. de Visser, and R. Bliem. “Tuning material properties via disorder: From crystalline alloy to metallic glass”. In: *Materials Today Physics* 29 (2022), p. 100893. ISSN: 2542-5293. DOI: 10.1016/j.mtphys.2022.100893.

[41] W. C. Oliver and G. M. Pharr. “Measurement of hardness and elastic modulus by instrumented indentation: Advances in understanding and refinements to methodology”. In: *Journal of Materials Research* 19 (2004), pp. 3–20. ISSN: 2044-5326. DOI: 10.1557/jmr.2004.19.1.3.

[42] N. S. Gingrich. “The Diffraction of X-Rays by Liquid Elements”. In: *Rev. Mod. Phys.* 15 (1 1943), pp. 90–110. DOI: 10.1103/RevModPhys.15.90.

[43] G. Yetik, A. Troglia, S. Farokhipoor, S. van Vliet, J. Momand, B. J. Kooi, R. Bliem, and J. W. Frenken. “Ultrathin, sputter-deposited, amorphous alloy films of ruthenium and molybdenum”. In: *Surface and Coatings Technology* 445 (2022), p. 128729. ISSN: 0257-8972. DOI: 10.1016/j.surfcoat.2022.128729.

[44] S. Fähler, K. Sturm, and H.-U. Krebs. “Resputtering during the growth of pulsed-laser-deposited metallic films in vacuum and in an ambient gas”. In: *Applied Physics Letters* 75.24 (1999), pp. 3766–3768. ISSN: 0003-6951. DOI: 10.1063/1.125449.

[45] K. Sturm, S. Fähler, and H.-U. Krebs. “Pulsed laser deposition of metals in low pressure inert gas”. In: *Applied Surface Science* 154-155 (2000), pp. 462–466. ISSN: 0169-4332. DOI: 10.1016/S0169-4332(99)00407-9.

[46] H. Luan, X. Zhang, H. Ding, F. Zhang, J. H. Luan, Z. B. Jiao, Y.-C. Yang, H. Bu, R. Wang, J. Gu, C. Shao, Q. Yu, Y. Shao, Q. Zeng, N. Chen, C. T. Liu, and K.-F. Yao. “High-entropy induced a glass-to-glass transition in a metallic glass”. In: *Nature Communications* 13 (1 2004), p. 2183. ISSN: 2041-1723. DOI: 10.1038/s41467-022-29789-1.

[47] J. Howard, K. Carlson, and D. Chidambaram. “High-temperature metallic glasses: Status, needs, and opportunities”. In: *Phys. Rev. Mater.* 5 (4 2021), p. 040301. DOI: 10.1103/PhysRevMaterials.5.040301.

[48] D. V. Louzguine-Luzgin, D. B. Miracle, L. Louzguina-Luzgina, and A. Inoue. “Comparative analysis of glass-formation in binary, ternary, and multicomponent alloys”. In: *Journal of Applied Physics* 108.10 (2010), p. 103511. ISSN: 0021-8979. DOI: 10.1063/1.3506687.

[49] C. Suryanarayana and A. Inoue. “Iron-based bulk metallic glasses”. In: *International Materials Reviews* 58.3 (2013), pp. 131–166. DOI: 10.1179/1743280412Y.0000000007.

[50] K. Stolze, J. Tao, F. O. von Rohr, T. Kong, and R. J. Cava. “Sc–Zr–Nb–Rh–Pd and Sc–Zr–Nb–Ta–Rh–Pd High-Entropy Alloy Superconductors on a CsCl-Type Lattice”. In: *Chemistry of Materials* 30.3 (2018), pp. 906–914. DOI: 10.1021/acs.chemmater.7b04578.

[51] P. Edalati, A. Mohammadi, M. Ketabchi, and K. Edalati. “Ultrahigh hardness in nanostructured dual-phase high-entropy alloy AlCrFeCoNiNb developed by high-pressure torsion”. In: *Journal of Alloys and Compounds* 884 (2021), p. 161101. ISSN: 0925-8388. DOI: 10.1016/j.jallcom.2021.161101.

[52] E. George, W. Curtin, and C. Tasan. “High entropy alloys: A focused review of mechanical properties and deformation mechanisms”. In: *Acta Materialia* 188 (2020), pp. 435–474. ISSN: 1359-6454. DOI: 10.1016/j.actamat.2019.12.015.

[53] H. Yao, J. Qiao, J. Hawk, H. Zhou, M. Chen, and M. Gao. “Mechanical properties of refractory high-entropy alloys: Experiments and modeling”. In: *Journal of Alloys and Compounds* 696 (2017), pp. 1139–1150. ISSN: 0925-8388. DOI: 10.1016/j.jallcom.2016.11.188.

[54] G. V. Samsonov. “Handbook of the Physicochemical Properties of the Elements”. In: Springer US, 1968. Chap. Mechanical Properties of the Elements, pp. 387–446. DOI: 10.1007/978-1-4684-6066-7_7.

[55] M. Srikanth, A. R. Annamalai, A. Muthuchamy, and C.-P. Jen. “A Review of the Latest Developments in the Field of Refractory High-Entropy Alloys”. In: *Crystals* 11.6 (2021), p. 612. ISSN: 2073-4352. DOI: 10.3390/cryst11060612.

[56] F. Liu, P. K. Liaw, and Y. Zhang. “Recent Progress with BCC-Structured High-Entropy Alloys”. In: *Metals* 12.3 (2022), p. 501. ISSN: 2075-4701. DOI: 10.3390/met12030501.

[57] F. Tian, L. K. Varga, N. Chen, J. Shen, and L. Vitos. “Empirical design of single phase high-entropy alloys with high hardness”. In: *Intermetallics* 58 (2015), pp. 1–6. ISSN: 0966-9795. DOI: 10.1016/j.intermet.2014.10.010.

[58] S. Maiti and W. Steurer. “Structural-disorder and its effect on mechanical properties in single-phase TaNbHfZr high-entropy alloy”. In: *Acta Materialia* 106 (2016), pp. 87–97. ISSN: 1359-6454. DOI: 10.1016/j.actamat.2016.01.018.

[59] M. Zhang, X. Zhou, X. Yu, and J. Li. “Synthesis and characterization of refractory TiZrNbWMo high-entropy alloy coating by laser cladding”. In: *Surface and Coatings Technology* 311 (2017), pp. 321–329. ISSN: 0257-8972. DOI: 10.1016/j.surfcoat.2017.01.012.

[60] C. Cheng, X. Zhang, M. J. R. Haché, and Y. Zou. “Phase transition and nanomechanical properties of refractory high-entropy alloy thin films: effects of co-sputtering Mo and W on a TiZrHfNbTa system”. In: *Nanoscale* 14 (20 2022), pp. 7561–7568. DOI: 10.1039/D2NR01635D.

[61] H. Pelletier, J. Krier, and P. Mille. “Characterization of mechanical properties of thin films using nanoindentation test”. In: *Mechanics of Materials* 38.12 (2006), pp. 1182–1198. ISSN: 0167-6636. DOI: 10.1016/j.mechmat.2006.02.011.

[62] I. Ovid’ko, R. Valiev, and Y. Zhu. “Review on superior strength and enhanced ductility of metallic nanomaterials”. In: *Progress in Materials Science* 94 (2018), pp. 462–540. ISSN: 0079-6425. DOI: 10.1016/j.pmatsci.2018.02.002.

[63] L. Lin, X. Xian, Z. Zhong, C. Chen, Z. Zhu, Y. Wu, and P. K. Liaw. “A multi-phase CrMnFeCoNiAl0.75 high-entropy alloy with high strength at intermediate temperature”. In: *Intermetallics* 120 (2020), p. 106744. ISSN: 0966-9795. DOI: 10.1016/j.intermet.2020.106744.

[64] S. Fritze, C. M. Koller, L. von Fieandt, P. Malinovskis, K. Johansson, E. Lewin, P. H. Mayrhofer, and U. Jansson. “Influence of Deposition Temperature on the Phase Evolution of HfNbTiVZr High-Entropy Thin Films”. In: *Materials* 12.4 (2019). ISSN: 1996-1944. DOI: 10.3390/ma12040587.

[65] A. Inoue and A. Takeuchi. “Recent development and application products of bulk glassy alloys”. In: *Acta Materialia* 59.6 (2011), pp. 2243–2267. ISSN: 1359-6454. DOI: 10.1016/j.actamat.2010.11.027.

[66] D. V. Louzguine-Luzgin and A. Inoue. “Bulk Metallic Glasses: Formation, Structure, Properties, and Applications”. In: *Handbook of Magnetic Materials*. Ed. by K. Buschow. Vol. 21. Elsevier, 2013. Chap. 3, pp. 131–171. DOI: 10.1016/B978-0-444-59593-5.00003-9.

[67] S. Sarker, R. Tang-Kong, R. Schoeppner, L. Ward, N. A. Hasan, D. G. Van Campen, I. Takeuchi, J. Hattrick-Simpers, A. Zakutayev, C. E. Packard, and A. Mehta. “Discovering exceptionally hard and wear-resistant metallic glasses by combining machine-learning with high throughput experimentation”. In: *Applied Physics Reviews* 9.1 (2022), p. 011403. ISSN: 1931-9401. DOI: 10.1063/5.0068207.

APPENDIX

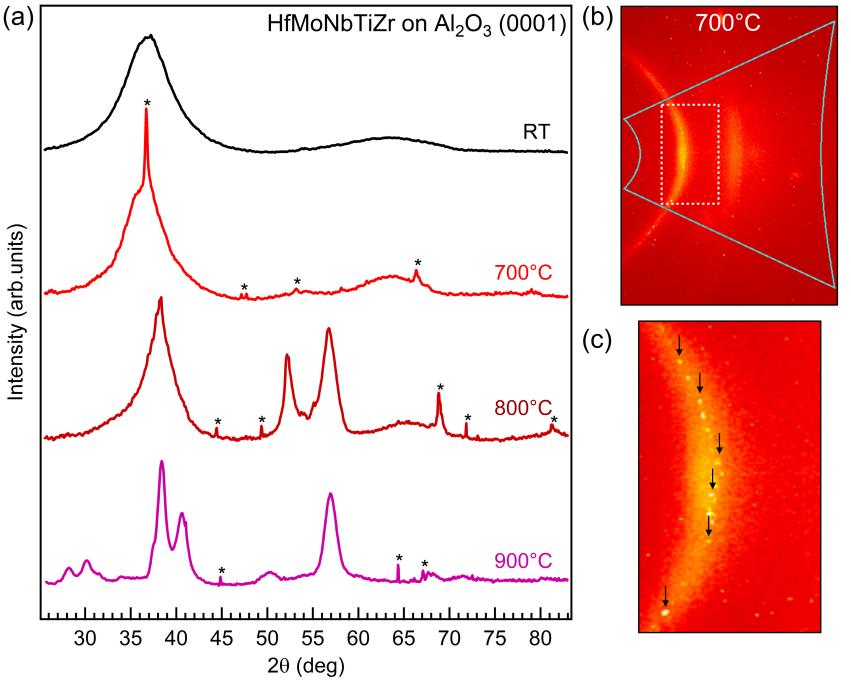

Figure 4.5 *(a) Raw GI-XRD diffractograms of HEA thin films deposited at different substrate temperatures, ranging from RT up to 900°C. (b) 2D detector image of the HEA film deposited at 700°C showing the presence of a few diffraction spots attributed to crystalline droplets. These spots have been marked with black arrows in the zoomed-in image in (c), corresponding to the dashed white square in (b).*

Figure 4.5 displays the raw GI-XRD diffractograms of HEA thin film as a function of growth temperature. The sharp peaks marked with black asterisks are ascribed to diffraction from individual large crystalline particles deposited on the surface in low density. The ejection of liquid metal droplets during deposition is common for laser-ablation of metals and can be reduced by polishing the PLD target (see for example the 2D-detector image of the sample grown at room temperature in Figure 4.1 (b)). The sharp diffraction peaks associated with the metal droplets have been removed in Figure 4.1 for clarity.

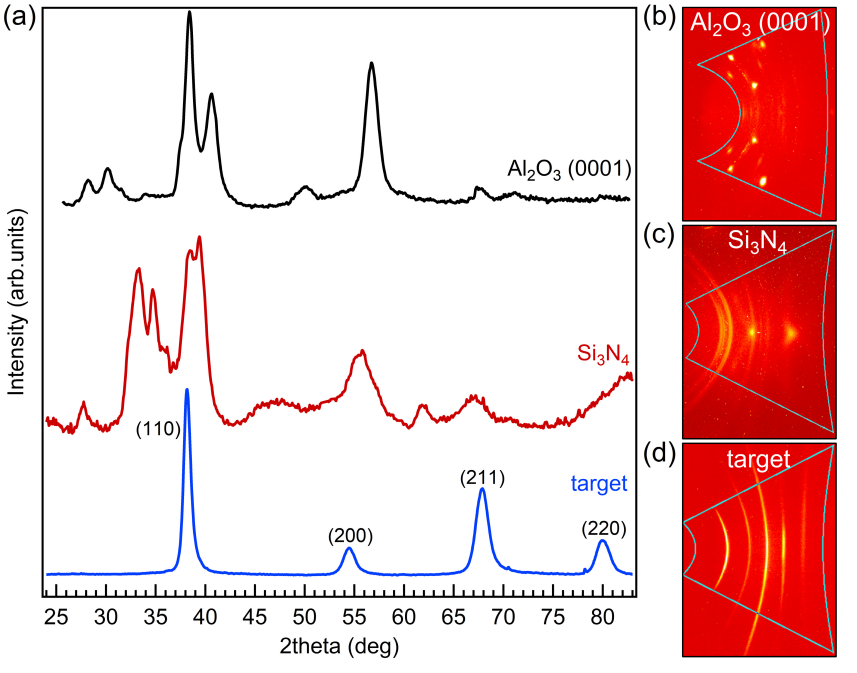

Figure 4.6 *(a) GI-XRD diffractograms of HfMoNbTiZr thin films deposited at T=900°C onto Al_2O_3(0001) substrate (black curve) and onto 100 nm thick (CVD deposited) amorphous Si_3N_4 on a Si(100) substrate (red curve). The diffractogram of the HEA target is also reported as a comparison (blue curve). (b-d) Corresponding 2D-detector images: the integration of the area marked with a light blue line allowed extracting the diffractograms reported in (a).*

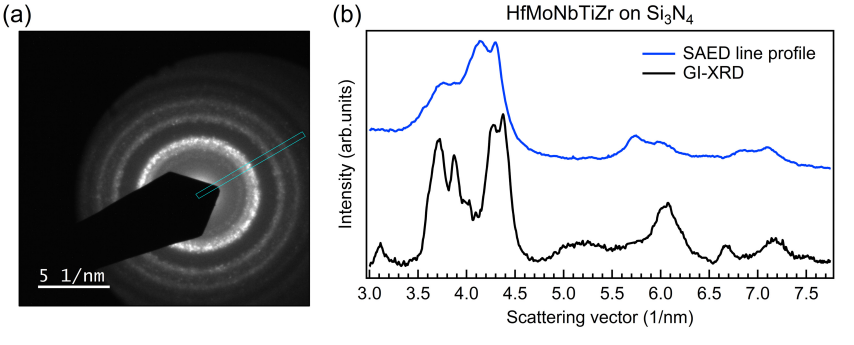

Figure 4.7 *(a) TEM SAED pattern corresponding to a crystalline region of a HfMoNbTiZr thin film deposited at 700°C onto a Si_3N_4 TEM window. The area marked with a light-blue curve has been used to extract the SAED line profile. (b) Comparison between the integrated SAED line profile in panel (a) (blue curve) and a GI-XRD diffractogram of a HEA thin film deposited at 900°C onto a Si_3N_4 substrate (black curve).*

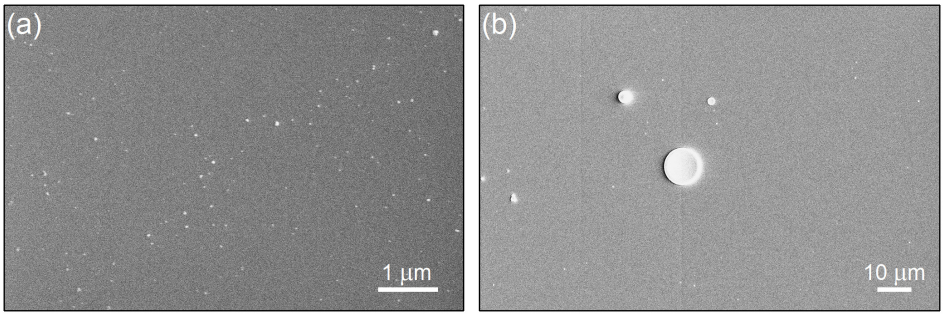

Figure 4.8 *Typical plan view scanning electron microscopy images of HfMoNbTiZr thin films (approximately 20 nm thick) deposited onto Al_2O_3 (0001) substrate. The surface exhibits a smooth and homogeneous morphology, characterized by the presence of metal droplets with a diameter ranging from a few tens of nanometers (a) up to 10 µm (b). These droplets give rise to sharp diffraction spots at well-defined angles on the GI-XRD 2D detector (see Figure 4.5).*

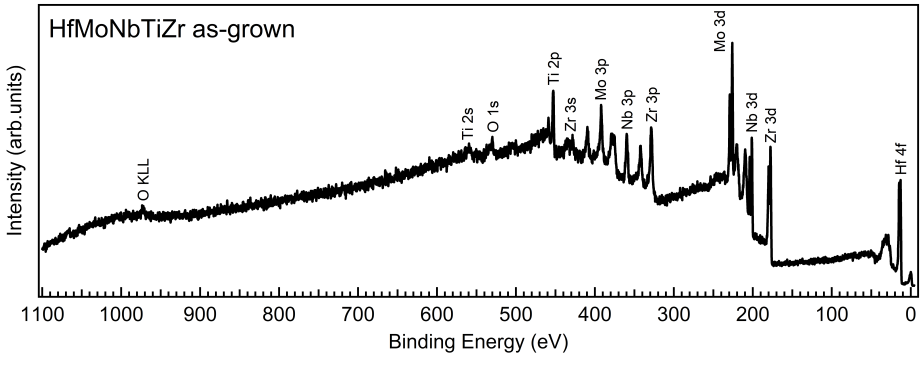

Figure 4.9 *In situ X-ray photoelectron spectroscopy investigation of an as-grown HfMoNbTiZr thin film (with a thickness of approximately 100 nm) deposited onto Al_2O_3 (0001) substrate at room temperature. The survey spectrum has been acquired at pass energy PE=500 eV. Only core level peaks ascribed to Hf, Mo, Nb, Ti, and Zr are visible in the XPS survey, with minor traces of O. The presence of a small amount of oxygen is ascribed to the interaction of highly reactive elements such as Zr and Hf with residual water present in the ultra-high vacuum chambers for deposition and spectroscopy.*

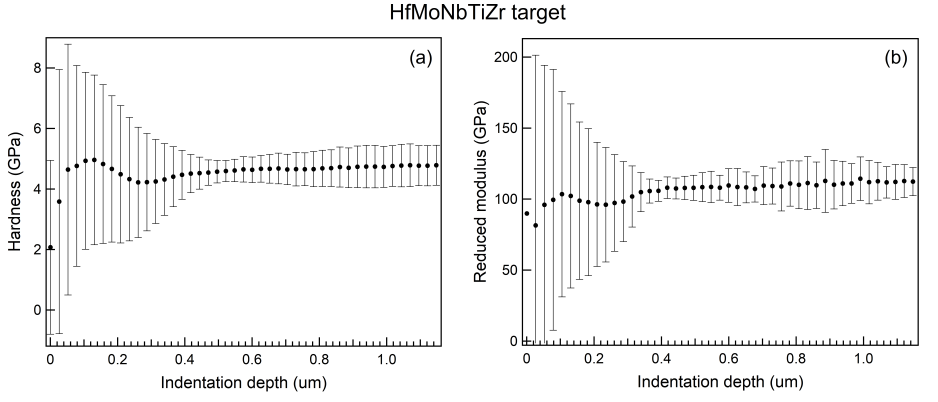

Figure 4.10 *Hardness (a) and corresponding reduced modulus (b) as a function of contact depth obtained from nanoindentation measurements of the HfMoNbTiZr PLD target. The high uncertainty obtained in the first ≈0.4 µm is ascribed to the high roughness of the target surface. The bulk hardness value has been extracted from the plateau region detected between approximately 0.5 µm and 1.1 µm.*

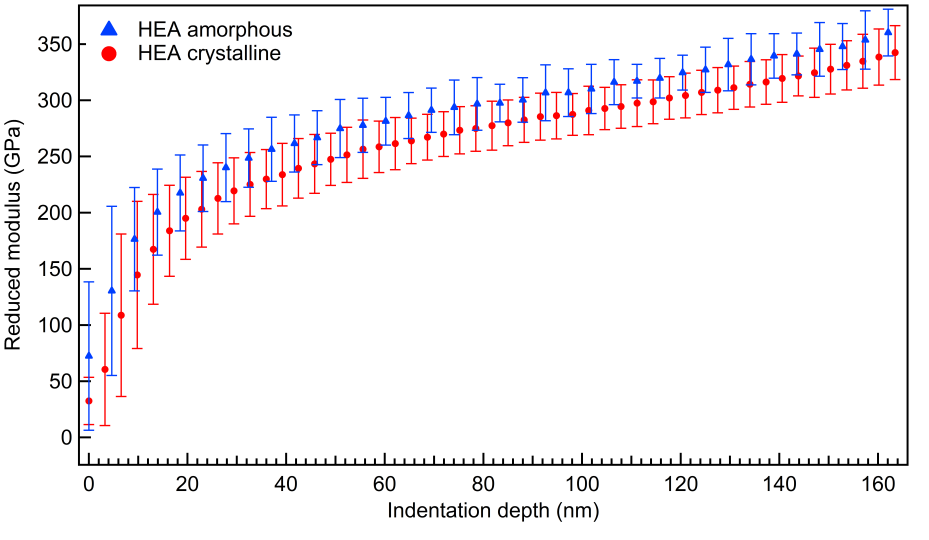

Figure 4.11 *Reduced modulus as a function of contact depth obtained from nanoindentation measurements of amorphous (blue curve) and crystalline (red curve) HfMoNbTiZr thin films deposited onto Al_2O_3 (0001). The thickness of both films was approximately 100 nm.*

SUMMARY

OPTIMIZING THIN-FILM PROPERTIES VIA ATOMIC-SCALE MODIFICATION

In materials science, the atomic scale is often overlooked if the primary interest is in macroscopic properties and a detailed atomic-level understanding is not essential. However, for a large variety of applications, ranging from free-standing nanolayers to hard, corrosion-resistant, and optically transparent thin films, the optimization of macroscopic properties can be achieved through controlled atomic-scale modification. In this thesis, this approach is focused on coatings of metals and alloys, which form an active area of research both in fundamental and applied contexts. Novel pathways to customize metallic films to specific requirements are explored. The effects on macroscopic performance are characterized and connected to an atomic-scale picture by employing a wide array of experimental techniques, including x-ray photoelectron spectroscopy, x-ray diffraction, atomic-force microscopy, Raman spectroscopy, and transmission electron microscopy. Here, the main conclusions and the most important experimental findings from the individual chapters are summarized, and their impact on the core themes of this thesis is highlighted.

In **chapter 1**, the background of the thesis is set by addressing the main advantages and drawbacks of the employed deposition techniques. Furthermore, growth kinetics and stress buildup/relaxation are briefly reviewed, since they play a fundamental role in the effects observed in the following chapters. The discussion is focused first on sputtering and pulsed laser deposition, and the influence of growth parameters on thin-film properties. This is particularly important in the context of atomic-scale optimization of thin films: the competition between thermodynamics and kinetics during deposition is addressed, and the possibility of using kinetics to influence the growth mode is discussed. The latter is critical for controlling film properties such as microstructure and morphology, which strongly influence the coating performance. Finally, the development of stress and the effects of stress-relaxation processes in thin films are reviewed. The background provided in these sections helps to understand the underlying atomic-scale processes and interpret the experimental results on macroscopic properties such as strength, chemical stability, and optical transparency of thin films.

A versatile, simple, and chemical-free method to produce free-standing layers of nanoscale thickness is explored in **chapter 2**. The observation that Ru layers deposited onto Si(100) delaminate upon annealing is explained using a stress-based mechanism, combining results from photoelectron spectroscopy, transmission, and scanning electron microscopy. The essential requirements for the observed mechanism of delamination are identified in the element Ru and the Si(100) substrate with native oxide. Upon annealing at temperatures above 400°C, diffusion of Si from the substrate into

the Ru layer is enabled, leading to the buildup of in-plane compressive stress, which is relaxed by local buckling that eventually results in a sharp separation of the coating at the interface between silicon oxide and Si. The delamination process can be generalized and extended to different metals and alloys by using a thin Ru buffer layer, allowing to harvest free-standing nanolayers of custom composition.

In **chapter 3**, the degree of structural disorder is investigated as an atomic-scale parameter for customizing functional coatings at the macroscale. This novel strategy is applied to a simple binary alloy system, and its impact on different material properties is studied on the example of CuZr. The approach based on PLD allows tuning the level of structural disorder without affecting other film parameters (such as stoichiometry) and enables to isolate the effects of the different atomic structures. Amorphous and crystalline CuZr layers with the same composition are directly compared, and the results demonstrate the critical role of disorder on the macroscopic film behavior, such as resistance to corrosion, electronic conductivity, and optical transparency. Crystalline CuZr layers are dark and reflective, show the conductivity of a bad metal, and grain boundary effects in their oxidation behavior. Conversely, the fully disordered nature of amorphous CuZr layers results in increased corrosion resistance and semiconductor-like behavior in the electronic and optical properties.

Similarly to the approach of chapter 3, the concept of deliberately introducing structural disorder is explored in **chapter 4** for multi-component alloy thin films. A promising class of materials, namely high-entropy alloys (HEAs), and their fully-disordered counterpart, high-entropy metallic glasses (HEMGs), have been chosen for the study. Amorphous and crystalline layers of HfMoNbTiZr of the same composition are fabricated with PLD and compared. This work sheds light on the modification of HfMoNbTiZr from HEA to HEMG, and the concomitant change in hardness. In this context, amorphous HfMoNbTiZr layers display higher hardness with respect to their crystalline counterparts, increased by approximately 30%. This result is ascribed to the lack of long-range order, which hinders atom mobility and enhances resistance to plastic deformations. Additionally, drastic variations in hardness between the bulk material and the thin films are observed.

In conclusion, since the first fundamental description by Feynman in 1959, the field of nanotechnology has experienced drastic breakthroughs and rapid development, allowing to shape today's technological landscape. Thin films in particular are essential in enhancing and functionalizing the performance of bulk materials. The ability to develop coatings with novel, tailored properties is a strong requirement to further push the boundaries of modern-day technology. In this context, optimizing the macroscopic film properties through tailored atomic-scale modification represents one of the most effective and fascinating aspects of thin-film technology. The experimental results reported in this thesis further strengthen the importance of atomic-scale properties in determining the macroscopic behavior, highlighting new ways of innovative materials design.

SAMENVATTING

OPTIMALISATIE VAN DUNNE LAAGEIGENSCHAPPEN DOOR MODIFICATIE OP ATOMAIRE SCHAAL

In de materiaalwetenschap wordt de atomaire schaal vaak over het hoofd gezien wanneer het primaire doel de macroscopische eigenschappen is, en gedetailleerd begrip van het materiaal op atomair niveau niet essentieel is. Echter kan de optimalisatie van macroscopische eigenschappen bereikt worden door modificatie op de atomaire schaal voor een grote verscheidenheid aan toepassingen, van vrijstaande nanolagen, tot aan harde, corrosiebestendige en optisch transparante dunne lagen. In dit proefschrift is deze aanpak toegespitst op coatings van metalen en legeringen, waar zowel in fundamentele als in toegepaste context actief onderzoek naar wordt gedaan. Nieuwe manieren worden verkend om metaalachtige lagen aan te passen aan specifieke eisen. De effecten op macroscopische prestaties worden gekarakteriseerd en verbonden aan een atomair plaatje door middel van een breed scala aan technieken, waaronder röntgenfoto-elektron spectroscopie, röntgendiffractie, atoomkrachtmicroscopie, Raman spectroscopie en transmissie-elektronenmicroscopie. Hieronder worden de voornaamste conclusies en belangrijkste experimentele bevindingen van de afzonderlijke hoofdstukken samengevat, en hun impact op de hoofdthema's van dit proefschrift wordt gemarkeerd.

In **hoofdstuk 1** wordt de achtergrond van dit proefschrift geschetst door de voornaamste voor- en nadelen van de gebruikte depositietechnieken te adresseren. Verder worden de groeikinetiek van dunne lagen en opbouw/relaxatie van mechanische spanning kort doorgenomen, aangezien deze een fundamentele rol spelen in de waargenomen fenomenen van de volgende hoofdstukken. Allereerst wordt de focus gelegd op sputteren en 'pulsed laser deposition' (PLD), evenals op de invloed van groeiparameters op de eigenschappen van dunne lagen. Dit is bijzonder belangrijk in de context van optimalisatie van dunne lagen op de atomaire schaal: de competitie tussen thermodynamica en kinetiek gedurende depositie wordt geadresseerd, en de mogelijkheid om kinetiek te gebruiken om de groeimodus te beïnvloeden wordt bediscussieerd. Dit laatste is van kritiek belang om dunne laageigenschappen zoals de microstructuur en de morfologie te beheersen, welke de prestaties van de coating sterk beïnvloeden. Tenslotte worden de ontwikkeling van mechanische spanning en de effecten van relaxatie daarvan in dunne lagen herzien. De achtergrondinformatie die in deze secties wordt gegeven helpt in het begrijpen van de onderliggende processen op atomaire schaal, en in het interpreten van de experimentele resultaten van macroscopische eigenschappen zoals de sterkte, chemische stabiliteit en optische transparantie van dunne lagen.

Een veelzijdige, simpele, en chemicaliën-vrije methode om vrijstaande lagen van nanometer dikte te produceren wordt verkend in **hoofdstuk 2**. De waarneming dat ruthe-

nium lagen gedeponeerd op Si(100) delamineren na verhitting, wordt verklaard door middel van een mechanisme gebaseerd op mechanische spanning, waarbij resultaten van foto-elektronenspectroscopie, transmissie- en rasterelektronenmicroscopie worden gecombineerd. De essentiële vereisten voor dit geobserveerde mechanisme van delaminatie worden geïdentificeerd voor het element Ru en het Si(100) substraat met natuurlijke oxidelaag. Bij verhitting tot temperaturen boven 400°C wordt diffusie van Si vanuit het substraat naar de Ru laag mogelijk gemaakt, wat leidt tot opbouw van drukspanning binnenin de laag. De spanning relaxeert door middel van een lokale "knik" in de laagstructuur, wat uiteindelijk resulteert in een scherpe scheiding van de coating bij het grensvlak tussen het Si kristal en de natuurlijke siliciumoxide. Dit proces van delaminatie kan gegeneraliseerd worden en worden uitgebreid naar verschillende metalen en legeringen door gebruik van een dunne Ru bufferlaag, wat het mogelijk maakt om vrijstaande nanolagen van zelfgekozen samenstelling te fabriceren.

In **hoofdstuk 3** wordt de mate van structurele wanorde onderzocht als een atomaire parameter voor het aanpassen van functionele coatings op de macroschaal. Deze vernieuwende strategie is toegepast op een simpele binaire legering, en de invloed op verschillende materiaaleigenschappen is onderzocht voor het voorbeeld van CuZr. Deze aanpak gebaseerd op PLD maakt het mogelijk om de mate van structurele wanorde af te stellen zonder invloed te hebben op de andere parameters van het film (zoals de stoichiometrie) en stelt ons in staat om de effecten van de verschillende atomaire structuren te isoleren. Amorfe en kristallijne CuZr lagen met dezelfde stoichiometrie worden rechtstreeks vergeleken en de resultaten laten de cruciale rol zien van wanorde in het macroscopische gedrag van de laag, zoals de resistentie tegen corrosie, soortelijke geleidbaarheid, en de optische transparantie. Kristallijne CuZr lagen zijn donker en reflectief, hebben de geleidbaarheid van een slecht metaal, en tonen de effecten van korrelgrenzen in hun oxidatiegedrag. Daarentegen resulteert de volledig ongeordende aard van een amorfe CuZr laag in een toename van de resistentie tegen corrosie en halfgeleider-achtig gedrag in termen van de elektronische en optische eigenschappen.

Vergelijkbaar met de aanpak in hoofdstuk 3 wordt in **hoofdstuk 4** het concept van opzettelijk structurele wanorde introduceren verder verkend, ditmaal voor dunne lagen van legeringen met meerdere componenten. Een veelbelovende klasse materialen, te weten zogeheten 'high-entropy alloys' (HEAs), en hun volledig ongeordende tegenhangers, 'high-entropy metallic glasses' (HEMGs), zijn gekozen voor deze studie. Amorfe en kristalline lagen van HfMoNbTiZr met dezelfde compositie worden gefabriceerd met PLD en daarna onderling vergeleken. Dit werk belicht de modificatie van HfMoNbTiZr van HEA tot HEMG en de daarbij horende verandering in hardheid. In deze context tonen amorfe HfMoNbTiZr lagen een hogere hardheid vergeleken met hun kristallijne tegenhanger, met een toename van ongeveer 30%. Dit resultaat wordt toegeschreven aan het gebrek van lange-afstandsorde, wat atomaire mobiliteit hindert en de weerstand tegen plastische vervorming verhoogt. Bovendien worden drastische variaties in hardheid waargenomen tussen bulk materiaal en dunne lagen.

Ten slotte, sinds de allereerste fundamentele omschrijving door Feynman in 1959, heeft het veld van nanotechnologie drastische doorbraken en rappe ontwikkelingen doorgemaakt, waardoor het vorm heeft kunnen geven aan het hedendaagse technologische landschap. Dunne lagen in het bijzonder zijn essentieel in het verbeteren en

functionaliseren van de prestaties van bulkmaterialen. Het vermogen om coatings te ontwikkelen met vernieuwende, op maat gemaakte eigenschappen is een sterk vereiste voor het verder verleggen van de grenzen van de moderne technologie. In deze context vertegenwoordigt het optimaliseren van macroscopische eigenschappen door middel van modificatie op atomaire schaal één van de meest effectieve en fascinerende aspecten van de technologie van dunne lagen. De experimentele resultaten getoond in dit proefschrift versterken het belang van de eigenschappen op atomair niveau in het bepalen van het macroscopisch gedrag, wat nieuwe manieren van innovatief ontwerp van materialen benadrukt.

LIST OF PUBLICATIONS

This thesis is based on the following publications:

CHAPTER 2

A. Troglia, S. van Vliet, G. Yetik, I. El Wakil, J. Momand, B. J. Kooi, and R. Bliem. *Free-standing nanolayers based on Ru silicide formation on Si(100).* Physical Review Materials **6**, 043402 (2022).

CHAPTER 3

A. Troglia, V. Vollema, S. Cassanelli, E. van Heumen, J. van de Groep, A. de Visser, and R. Bliem. *Tuning material properties via disorder: From crystalline alloy to metallic glass.* Materials Today Physics **29**, 100893 (2022).

CHAPTER 4

A. Troglia, C. Leriche, M. van de Poll, G. ten Brink, B. J. Kooi, B. Weber, and R. Bliem. *Bridging the gap between high-entropy alloys and metallic glasses: Control over disorder and mechanical properties of coatings.* Submitted (2024).

The author has also contributed to the following publications:

[11] L. Cruciani, S. van Vliet, **A. Troglia**, R. Bliem, K. van Druten, and P. Planken. *Femtosecond Laser-Induced Emission of Coherent Terahertz Pulses from Ruthenium Thin Films.* The Journal of Physical Chemistry C, 127, 22662 - 22672 (2023).

[10] P. C. M. Laan, E. O. Bobylev, F. J. de Zwart, J. A. Vleer, **A. Troglia**, R. Bliem, G. Rothenberg, J. N. H. Reek, and N. Yan. *Tailoring Secondary Coordination Sphere Effects in Single-metal-site Catalysts by Surface Immobilization of Supramolecular Cages.* Chemistry – A European Journal, e202301901 (2023).

[9] P. C. M. Laan, F. J. de Zwart, E. M. Wilson, **A. Troglia**, O. C. M. Lugier, N. J. Geels, R. Bliem, J. N. H. Reek, B. de Bruin, G. Rothenberg, and N. Yan. *Understanding the Oxidative Properties of Nickel Oxyhydroxide in Alcohol Oxidation Reactions.* ACS Catalysis **13**, 13, 8467-8476 (2023).

[8] M. J. Mekkering, J. Biemolt, J. de Graaf, Y. Lin, N. P. van Leest, **A. Troglia**, R. Bliem, B. de Bruin, G. Rothenberg, and N. Yan. *Dry reforming of methane over single-atom Rh/Al_2O_3 catalysts prepared by exsolution.* Catalysis Science & Technology **13**, 2255-2260 (2023).

[7] S. van Vliet, **A. Troglia**, E. Olsson, and R. Bliem. *Identifying silicides via plasmon loss satellites in photoemission of the Ru-Si system.* Applied Surface Science **608**, 155139 (2023).

[6] G. Yetik, **A. Troglia**, S. Farokhipoor, S. van Vliet, J. Momand, B. J. Kooi, R. Bliem, and J. W. M. Frenken. *Ultrathin, sputter-deposited, amorphous alloy films of ruthenium and molybdenum.* Surface and Coatings Technology **445**, 128729 (2022).

[5] A. Goyal, M. van der Laan, **A. Troglia**, M. Lin, H. Agarwal, J. van de Groep, R. Bliem, J. M. J Paulusse, P. Schall, and K. Dohnalova. *Microscopic Proof of Photoluminescence from Mechanochemically Synthesized 1-Octene-Capped Quantum-Confined Silicon Nanoparticles: Implications for Light-Emission Applications.* ACS Omega **7**, 28, 24881–24887 (2022).

[4] **A. Troglia**, C. Bigi, I. Vobornik, J. Fujii, D. Knez, R. Ciancio, G. Dražić, M. Fuchs, D. Di Sante, G. Sangiovanni, G. Rossi, P. Orgiani, and G. Panaccione. *Evidence of a 2D Electron Gas in a Single-Unit-Cell of Anatase TiO_2(001).* Advanced Science **9**, 2105114 (2022).

[3] O. Lugier, **A. Troglia**, N. Sadegh, L. van Kessel, R. Bliem, N. Mahne, S. Nannarone, and S. Castellanos. *Extreme Ultraviolet Photoelectron Spectroscopy on Fluorinated Monolayers: towards Nanolithography on Monolayers.* Journal of Photopolymer Science and Technology **33**, 229-234 (2020).

[2] C. Bigi, Z. Tang, G. M. Pierantozzi, P. Orgiani, P. K. Das, J. Fujii, I. Vobornik, T. Pincelli, **A. Troglia**, T. L. Lee, R. Ciancio, G. Drazic, A. Verdini, A. Regoutz, P. D. C. King, D. Biswas, G. Rossi, G. Panaccione, and A. Selloni. *Distinct behavior of localized and delocalized carriers in anatase TiO_2(001) during reaction with O_2.* Physical Review Materials **4**, 025801 (2020).

[1] C. Bigi, P. Orgiani, A. Nardi, **A. Troglia**, J. Fujii, G. Panaccione, I. Vobornik, and G. Rossi. *Robustness of topological states in Bi_2Se_3 thin film grown by Pulsed Laser Deposition on (001)-oriented $SrTiO_3$ perovskite.* Applied Surface Science **473**, 190-193 (2019).

ACKNOWLEDGEMENTS

The journey to obtain a PhD degree can feel like a personal, sometimes even solitary endeavor. However, *'No Man is An Island'*, and the work described in this manuscript has been possible thanks to the help and support of many individuals. Here, I would like to express my gratitude to those people who have contributed over the past years to the completion of this work.

First of all, I would like to give special thanks to my supervisor, Roland Bliem. Roland: thank you for trusting me and for giving me the opportunity to join your newly formed group as your first PhD student. All the inspiring, extensive, and constructive discussions we had, taught me how to critically approach the complex problems I faced during the PhD work, and allowed me to grow both professionally and personally. Thank you for always being available to answer my (many) questions, for being open to different points of view, and for guiding and supporting me throughout this journey with a positive and encouraging attitude.

I am also very grateful to my promotor, Mark Golden, and all the other members of the committee: Paul Planken, Anna Isaeva, Erik van Heumen, Gertjan Koster, and Richard van Lent, for taking the time out of their busy schedule to carefully read and evaluate this thesis.

A large part of the research described in this manuscript would not have been possible without the help of many collaborators, to whom I am deeply grateful. I would like to thank Bart Kooi, Jamo Momand, and Gert ten Brink from the University of Groningen for performing the TEM measurements on our samples. Next, I would like to thank Jorik van de Groep, Anne de Visser, Erik van Heumen, and Silvia Cassanelli from the University of Amsterdam for the Raman spectroscopy, resistivity, and optical spectroscopy measurements of the CuZr thin films. Also, I would like to acknowledge Sven Hennig from the Vrije Universiteit Amsterdam for allowing me to use the x-ray diffractometer system for the thin-film structural investigations. Lastly, I would like to thank Bart Weber and Cyrian Leriche from the Contact Dynamics group at ARCNL for the hardness measurements on the high-entropy alloy thin films.

I would like to extend my gratitude to the present and past members of the Materials and Surface Science for EUVL group at ARCNL: Stefan van Vliet, Tadé Hogenelst, Ester Pérez Penco, Cristiane Stilhano Vilas Boas, Christoph Morscher, Jan Verhoeven, Ibrahim El Wakil, Mike van de Poll, Ruben Visser, Arend-Jan van Calcar, and Bartjan Spaanderman. Together we shared countless days in the lab, performing experiments, maintenance, and bake-outs. Thank you for creating a stimulating, collaborative, fun, and friendly atmosphere both in the lab and outside ARCNL walls. When I started the PhD journey, the group consisted of just two people, Roland and myself, however it grew rapidly, and I am proud to see it well established and successful.

I would like to thank the former ARCNL director Joost Frenken, the institute manager

Marjan Fretz, and the present ARCNL director Wim van der Zande for their full support during these years. An important mention goes to the AMOLF/ARCNL support staff, to the electronic, software and ICT departments, and to the staff of the AMOLF workshop and NanoLab. Also, a big thank you to all the people at ARCNL, past and present, for welcoming me into the ARCNL family and making me feel at home.

I would like to dedicate a few words to my paranymphs, Görsel and Victor. Görsel: when I first joined ARCNL, I felt a bit lost and overwhelmed, however, you helped me during the first few months, showing me around and making me feel welcome. We started working together, and quickly became good friends. Thank you for always being patient and available to help, and for counterbalancing my (slight) pessimism with a pragmatic attitude. Victor: together we shared not only the office, but all the good and difficult moments of our PhD journeys. Thank you for always being supportive, ready to help, available to share your vast knowledge, and for being a dear friend throughout these years. Working with you has been really stimulating and inspiring, and I would like to thank you also for contributing to this manuscript with AFM measurements and analysis.

To Fiona, thank you for always being by my side and for giving me strength during these years. Completing this work would not have been possible without your constant and loving support.

Infine, vorrei dedicare le ultime parole di questo manoscritto alla mia famiglia. A mia mamma Diana, a mio papà Marco, a mia sorella Marina, a mio 'fratello' Pier e al mio nipotino Nicolò: grazie per aver sempre creduto in me, per il vostro affetto e sostegno incondizionato, e per ricordarmi che '*andrà tutto benissimo*'. Questa tesi è dedicata a voi.

Amsterdam,
July 2024